The Astrophysical Journal Supplement Series, 255:29 (35pp), 2021 August https://doi.org/10.3847/1538-4365/abff5e

The Palomar Transient Factory Core-collapse Supernova Host-galaxy Sample. I. Host-galaxy Distribution Functions and Environment Dependence of Core-collapse Supernovae

Steve Schulze[1], Ofer Yaron[1], Jesper Sollerman[2], Giorgos Leloudas[3], Amit Gal[4], Angus H. Wright[5], Ragnhild Lunnan[2], Avishay Gal-Yam[1], Eran O. Ofek[1], Daniel A. Perley[6], Alexei V. Filippenko[7,8], Mansi M. Kasliwal[9], Shrinivas R. Kulkarni[10], James D. Neill[9], Peter E. Nugent[7,11], Robert M. Quimby[12,13], Mark Sullivan[14], Nora Linn Strotjohann[1], Iair Arcavi[15,16], Sagi Ben-Ami[1], Federica Bianco[17,18,19,20], Joshua S. Bloom[7,11], Kishalay De[9], Morgan Fraser[21], Christoffer U. Fremling[9], Assaf Horesh[22], Joel Johansson[23], Patrick L. Kelly[24], Nikola Knežević[25], Sladjana Knežević[26], Kate Maguire[27], Anders Nyholm[2], Seméli Papadogiannakis[23], Tanja Petrushevska[28], Adam Rubin[29], Lin Yan[30], Yi Yang[1,7], Scott M. Adams[10], Filomena Bufano[31], Kelsey I. Clubb[7], Ryan J. Foley[32], Yoav Green[33], Jussi Harmanen[34], Anna Y. Q. Ho[7,10], Isobel M. Hook[35], Griffin Hosseinzadeh[36], D. Andrew Howell[37,38], Albert K. H. Kong[39], Rubina Kotak[34], Thomas Matheson[40], Curtis McCully[37,38], Dan Milisavljevic[41], Yen-Chen Pan[42], Dovi Poznanski[15], Isaac Shivvers[7], Sjoert van Velzen[43,44], and Kars K. Verbeek[45]

[1] Department of Particle Physics and Astrophysics, Weizmann Institute of Science, 234 Herzl Street, 76100 Rehovot, Israel; steve.schulze@weizmann.ac.il, steve.schulze@fysik.su.se
[2] Department of Astronomy, The Oskar Klein Centre, Stockholm University, AlbaNova, SE-10691 Stockholm, Sweden
[3] DTU Space, National Space Institute, Technical University of Denmark, Elektrovej 327, DK-2800 Kgs. Lyngby, Denmark
[4] Department of Physics of Complex Systems, Weizmann Institute of Science, 234 Herzl Street, 76100 Rehovot, Israel
[5] Ruhr-Universität Bochum, Astronomisches Institut, German Centre for Cosmological Lensing, Universitätsstr. 150, D-44801 Bochum, Germany
[6] Astrophysics Research Institute, Liverpool John Moores University, 146 Brownlow Hill, Liverpool, L3 5RF, UK
[7] Department of Astronomy, University of California, Berkeley, CA 94720-3411, USA
[8] Miller Institute for Basic Research in Science, University of California, Berkeley, CA 94720, USA
[9] Division of Physics, Mathematics, and Astronomy, California Institute of Technology, Pasadena, CA 91125, USA
[10] Cahill Center for Astrophysics, California Institute of Technology, 1200 E. California Boulevard, Pasadena, CA 91125, USA
[11] Lawrence Berkeley National Laboratory, 1 Cyclotron Road, MS 50B-4206, Berkeley, CA 94720, USA
[12] Department of Astronomy / Mount Laguna Observatory, San Diego State University, 5500 Campanile Drive, San Diego, CA 92812-1221, USA
[13] Kavli Institute for the Physics and Mathematics of the Universe (WPI), The University of Tokyo Institutes for Advanced Study, The University of Tokyo, Kashiwa, Chiba 277-8583, Japan
[14] School of Physics and Astronomy, University of Southampton, Southampton, SO17 1BJ, UK
[15] School of Physics and Astronomy, Tel Aviv University, Tel Aviv, 69978, Israel
[16] CIFAR Azrieli Global Scholars program, CIFAR, Toronto, Canada
[17] Department of Physics and Astronomy, University of Delaware, Newark, DE, 19716, USA
[18] Joseph R. Biden, Jr. School of Public Policy and Administration, University of Delaware, Newark, DE, 19716, USA
[19] Data Science Institute, University of Delaware, Newark, DE, 19716, USA
[20] Center for Urban Science and Progress, New York University, 370 Jay Street, Brooklyn, NY 11201, USA
[21] School of Physics, O'Brien Centre for Science North, University College Dublin, Belfield, Dublin 4, Ireland
[22] Racah Institute of Physics, The Hebrew University of Jerusalem, 91904 Jerusalem, Israel
[23] Department of Physics, The Oskar Klein Centre, Stockholm University, AlbaNova, SE-10691 Stockholm, Sweden
[24] Minnesota Institute for Astrophysics, University of Minnesota, 116 Church Street SE, Minneapolis, MN 55455, USA
[25] Department of Astronomy, Faculty of Mathematics, University of Belgrade, Studentski trg 16, 11000 Belgrade, Serbia
[26] Astronomical Observatory, Volgina 7, 11060 Belgrade, Republic of Serbia
[27] School of Physics, Trinity College Dublin, The University of Dublin, College Green, Dublin 2, Ireland
[28] Centre for Astrophysics and Cosmology, University of Nova Gorica, Vipavska 11c, 5270 Ajdovščina, Slovenia
[29] European Southern Observatory, Karl-Schwarzschild-Str 2, D-85748 Garching, Germany
[30] The Caltech Optical Observatories, California Institute of Technology, Pasadena, CA 91125, USA
[31] INAF - Osservatorio Astrofisico di Catania, Via Santa Sofia 78, I-95123, Catania, Italy
[32] Department of Astronomy and Astrophysics,University of California, Santa Cruz, CA 95064, USA
[33] Department of Mechanical Engineering, Ben-Gurion University of the Negev, 8410501 Beer-Sheva, Israel
[34] Department of Physics and Astronomy, University of Turku, FI-20014 Turku, Finland
[35] Department of Physics, Lancaster University, Lancaster, LA1 4YB, UK
[36] Center for Astrophysics | Harvard & Smithsonian, 60 Garden Street, Cambridge, MA 02138-1516, USA
[37] Las Cumbres Observatory, 6740 Cortona Drive, Suite 102, Goleta, CA 93117, USA
[38] University of California, Santa Barbara, Department of Physics, Santa Barbara, CA, 93111, USA
[39] Institute of Astronomy, National Tsing Hua University, Hsinchu 30013, Taiwan
[40] NSF's National Optical-Infrared Astronomy Research Laboratory, 950 North Cherry Avenue, Tucson, AZ 85719, USA
[41] Department of Physics and Astronomy, Purdue University, 525 Northwestern Avenue, West Lafayette, IN 47907, USA
[42] Graduate Institute of Astronomy, National Central University, 300 Jhongda Road, Zhongli, Taoyuan 32001, Taiwan
[43] Department of Astronomy, University of Maryland, College Park, MD 20742, USA
[44] Center for Cosmology and Particle Physics, New York University, NY 10003, USA
[45] Department of Astrophysics/IMAPP, Radboud University, P.O. Box 9010, 6500 GL Nijmegen, The Netherlands

Received 2020 August 13; revised 2021 April 15; accepted 2021 April 21; published 2021 August 10

Abstract

Several thousand core-collapse supernovae (CCSNe) of different flavors have been discovered so far. However, identifying their progenitors has remained an outstanding open question in astrophysics. Studies of SN host galaxies have proven to be powerful in providing constraints on the progenitor populations. In this paper, we present all CCSNe detected between 2009 and 2017 by the Palomar Transient Factory. This sample includes 888 SNe of 12 distinct classes out to redshift $z \approx 1$. We present the photometric properties of their host galaxies from the far-ultraviolet to the mid-infrared and model the host-galaxy spectral energy distributions to derive physical properties. The galaxy mass function of Type Ic, Ib, IIb, II, and IIn SNe ranges from 10^5 to $10^{11.5}\,M_\odot$, probing the entire mass range of star-forming galaxies down to the least-massive star-forming galaxies known. Moreover, the galaxy mass distributions are consistent with models of star-formation-weighted mass functions. Regular CCSNe are hence direct tracers of star formation. Small but notable differences exist between some of the SN classes. Type Ib/c SNe prefer galaxies with slightly higher masses (i.e., higher metallicities) and star formation rates than Type IIb and II SNe. These differences are less pronounced than previously thought. H-poor superluminous supernovae (SLSNe) and SNe Ic-BL are scarce in galaxies above $10^{10}\,M_\odot$. Their progenitors require environments with metallicities of < 0.4 and < 1 solar, respectively. In addition, the hosts of H-poor SLSNe are dominated by a younger stellar population than all other classes of CCSNe. Our findings corroborate the notion that low metallicity and young age play an important role in the formation of SLSN progenitors.

Unified Astronomy Thesaurus concepts: Supernovae (1668); Core-collapse supernovae (304); Galaxies (573); Galactic and extragalactic astronomy (563)

Supporting material: machine-readable tables

1. Introduction

Stars with zero-age-main-sequence (ZAMS) masses of at least 8 $M_\odot$ can presumably explode as core-collapse supernovae (CCSNe; for a review, see, e.g., Smartt 2009 and references therein), which can be detected out to large cosmological distances (Howell et al. 2013; Pan et al. 2017; Smith et al. 2018; Moriya et al. 2019; Curtin et al. 2019). Their large distances allow a wide range of stellar populations and even star formation environments that do not exist in the Milky Way galaxy to be examined. CCSNe are divided into three families (H poor, H rich, and interaction-powered SNe) and more than a dozen classes and subclasses based on the absence or presence of particular absorption and emission lines, line widths, and SN peak luminosities (e.g., Filippenko 1997; Gal-Yam 2017). How the different SN types are related to each other, what their progenitors are, and what the mapping between SN and progenitor properties is have remained outstanding problems in contemporary astrophysics.

Given the typical SN distances, a direct search of their progenitors is infeasible in most cases (e.g., Smartt 2009; Van Dyk 2017). Studies of their host galaxies have proven to be powerful to indirectly provide constraints on the progenitor populations. These studies have examined (i) the host morphologies and locations of SNe in their hosts and large-scale structures (e.g., van den Bergh 1997; Tsvetkov et al. 2004; Hakobyan et al. 2008; Habergham et al. 2010, 2012; Hakobyan et al. 2014, 2016), (ii) how SNe trace the light and star formation in their hosts (e.g., Fruchter et al. 2006; Kelly et al. 2008; Leloudas et al. 2010; Svensson et al. 2010; Anderson et al. 2012; Kelly & Kirshner 2012; Lunnan et al. 2015; Kangas et al. 2017), (iii) the galaxy masses, star formation rates (SFRs), and metallicities of the hosts (e.g., Prieto et al. 2008; Neill et al. 2011; Kelly & Kirshner 2012; Stoll et al. 2013; Taddia et al. 2013; Kelly et al. 2014; Lunnan et al. 2014; Leloudas et al. 2015; Angus et al. 2016; Perley et al. 2016; Schulze et al. 2018; Angus et al. 2019; Hosseinzadeh et al. 2019; Modjaz et al. 2020; Taggart & Perley 2021), (iv) the metallicities and stellar populations at the explosion sites (e.g., Modjaz et al. 2008; Leloudas et al. 2011; Kelly & Kirshner 2012; Sanders et al. 2012; Kuncarayakti et al. 2013a, 2013b; Taddia et al. 2015; Thöne et al. 2015; Galbany et al. 2016; Chen et al. 2017b; Thöne et al. 2017; Galbany et al. 2018; Izzo et al. 2018; Kuncarayakti et al. 2018), and (v) the frequency ratio between different SN types as a function of galaxy properties (e.g., Prantzos & Boissier 2003; Prieto et al. 2008; Boissier & Prantzos 2009; Arcavi et al. 2010; Li et al. 2011; Graur et al. 2017a, 2017b).

In addition, these studies revealed the commonalities and diversities of various SN classes as well as the interplay of SN and host-galaxy properties. Despite the success of these studies, most of them were based on small or statistically biased samples. Deep wide-field synoptic surveys led to overcoming both limitations and paved the path for the next milestones in SN science. The Palomar Transient Factory (PTF; Law et al. 2009; Rau et al. 2009) and its immediate successor, the intermediate Palomar Transient Factory (iPTF; Kulkarni 2013), is an example of such a survey. It used the 1.2 m (48 inch) Oschin Schmidt telescope (P48) at Palomar Observatory (USA) and was operated between 2009 and mid-2017. PTF was an untargeted transient survey designed to systematically map out existing gaps in the transient phase space and search for theoretically predicted but not yet detected phenomena. The crucial advantages of the PTF survey were its large field of view of 7.2 deg^2, to monitor a substantial area of the night sky, and its well-matched spectroscopic resources, to routinely obtain spectra of even the faintest transients detected with the P48. Between 2009 and mid-2017, PTF discovered over 3000 SNe ($\gtrsim$2100 SNe Ia and $\gtrsim$900 CCSNe).

In this paper, we present the CCSN sample and its host-galaxy properties. Our scope is to (i) deduce the distribution functions of the host-galaxy properties such as mass and SFR, (ii) quantify the environment dependence for the production efficiency of the main SN classes, and (iii) indirectly constrain the progenitor properties for the largest CCSN classes.

We assume ΛCDM cosmology with $H_0 = 67.8\ \mathrm{km\,s^{-1}\,Mpc^{-1}}$, $\Omega_M = 0.308$, and $\Omega_\Lambda = 0.692$ (Planck Collaboration et al. 2016). We report uncertainties at 1σ confidence. All magnitudes are given in the AB system (Oke & Gunn 1983). A machine-readable catalog of the PTF CCSN sample is available at http://www.github.com/steveschulze/PTF. SN classification spectra will be publicly available on WISeREP[46] (Yaron & Gal-Yam 2012). Further data products, such as tabulated versions of the probability distribution functions, detailed outputs from the galaxy spectral energy distribution (SED) modeling, and the host identification, will be released on the aforementioned GitHub page after acceptance of the paper.

---

[46] https://wiserep.weizmann.ac.il

2. Data

2.1. Supernova Data

2.1.1. Photometry

We retrieved fully reduced SN images obtained with P48 and the 1.5 m (60 inch) P60 telescopes from the NASA/IPAC Infrared Science Archive[47] and the P60 archive, respectively. The P48 image reduction is described by Laher et al. (2014), while the PTF photometric calibration and the photometric system are discussed by Ofek et al. (2012). We used these data only for the host-galaxy identification. The SN light curves and their analysis are beyond the scope of this paper.

2.1.2. Spectroscopy

Supernova spectra were obtained primarily with the low-resolution Double Beam Spectrograph (DBSP; Oke & Gunn 1982) on the 5 m (200 inch) Hale telescope (P200) at Palomar Observatory (USA), the Low-Resolution Imaging Spectrometer (LRIS; Oke et al. 1995) on the 10 m Keck I telescope on Maunakea (USA), and the Kast double spectrograph[48] on the 3 m Shane telescope at Lick Observatory on Mount Hamilton (USA).

We augmented this data set with observations obtained with

1. the Dual Imaging Spectrograph[49] (DIS) on the 3.5 m telescope at the Apache Point Observatory (APO; USA);
2. the low-resolution Gemini Multi-Object Spectrograph (GMOS; Hook et al. 2004) on the 8.1 m Gemini telescopes on Hawaii (USA) and Cerro Pachón (Chile);
3. the low-resolution spectrograph (LRS; Hill et al. 1998) at the 10 m Hobby-Eberly Telescope (USA);
4. the DeVeny Spectrograph[50] at the 4.3 m Lowell Discovery Telescope (USA);
5. the optical DEep Imaging Multi-Object Spectrograph (DEIMOS; Faber et al. 2003) on the 10 m Keck II telescope (USA);
6. the Ritchey-Chretien Focus Spectrograph[51] (RC) on the 4 m Kitt Peak National Observatory (KPNO) telescope (USA);
7. the Inamori Magellan Areal Camera and Spectrograph (IMACS; Bigelow & Dressler 2003) and the Folded port InfraRed Echellette spectrograph (FIRE; Simcoe et al. 2013) at the 6.5 m Magellan telescope at the Las Campanas Observatory, Chile;
8. the FLOYDS spectrographs at the northern (FTN; USA) and southern (FTS; Australia) 2 m Las Cumbres Observatory telescopes (Brown et al. 2013);
9. the Alhambra Faint Object Spectrograph Camera[52] (ALFOSC) on the 2.56 m Nordic Optical Telescope (NOT; Spain)
10. the low-dispersion integral-field spectrograph and imager SED Machine (SEDM; Blagorodnova et al. 2018) at the Palomar 60 inch (1.5 m) telescope (USA);
11. the Device Optimized for the LOw RESolution[53] (DOLORES) at the 3.58 m Telescopio Nazionale Galileo (TNG; Spain);
12. the Supernova Integral Field Spectrograph (SNIFS; Lantz et al. 2004) at the 88 inch (2.2 m) University of Hawaii Telescope (USA);
13. the optical-to-near-infrared echellete spectrograph X-shooter (Vernet et al. 2011) on the ESO 8.2 m Very Large Telescope (VLT; Chile); and
14. the Auxiliary-port CAMera (ACAM; Benn et al. 2008) and the Intermediate-dispersion Spectrograph and Imaging System[54] (ISIS) on the 4.2 m William Herschel Telescope (WHT; Spain).

For a few objects, we utilized publicly available spectra. A log of the spectroscopic observations, including references to the archival data, is presented in Table 8 in Appendix A.

2.2. Host-galaxy Data

2.2.1. Photometry

We retrieved science-ready coadded images from the Galaxy Evolution Explorer (GALEX) general release 6/7 (Martin et al. 2005), the Sloan Digital Sky Survey data release 9 (SDSS DR9; Ahn et al. 2012), the Panoramic Survey Telescope and Rapid Response System (PanSTARRS, PS1) DR1 (Chambers et al. 2016), the Two Micron All Sky Survey (2MASS; Skrutskie et al. 2006), and preprocessed WISE images (Wright et al. 2010) from the unWISE archive (Lang 2014).[55] The unWISE images are based on the public WISE data and include images from the ongoing NEOWISE-Reactivation mission R3 (Mainzer et al. 2014; Meisner et al. 2017).

Several fields were observed more than once with GALEX. We considered only those images where the respective SN was within $0\overset{\circ}{.}5$ from the center of a GALEX pointing to avoid regions where the GALEX zero point and astrometry begin to vary with distance from the pointing center (Bianchi et al. 2017). If a field was observed multiple times in a given filter, we chose the deepest observation. For the unWISE images, we only considered observations where a given SN was >50 pixels from the chip edge.

The hosts of $\sim$10% of our SN sample were not detected by these surveys. For those objects, we retrieved deeper optical images from the DESI Legacy Imaging Surveys (Legacy Surveys, LS; Dey et al. 2019) DR5–7, from the data archive of the 3.6 m Canada–France–Hawaii Telescope (USA), and images from the Hubble Space Telescope (HST). These data were provided as science-ready by the respective data archives. Furthermore, we augmented our data set with photometry presented by Lunnan et al. (2014), Cano et al. (2015), Angus et al. (2016), Vreeswijk et al. (2014), Perley et al. (2016), Toy et al. (2016), De et al. (2018), and Schulze et al. (2018).

The vital properties of the GALEX, LS, PS1, SDSS, 2MASS, and unWISE data are summarized in Table 1.

3. Methods

3.1. Host-galaxy Photometry

The survey images are characterized by different pixel (px) scales and point-spread functions (PSFs): the pixel scales vary

---

[47] https://irsa.ipac.caltech.edu/Missions/ptf.html

[48] https://mthamilton.ucolick.org/techdocs/instruments/kast/Tech%20Report%2066%20KAST%20Miller%20Stone.pdf

[49] https://www.apo.nmsu.edu/arc35m/Instruments/DIS

[50] https://jumar.lowell.edu/confluence/display/DCTIC/DCT+Information+Center+Home

[51] https://www.noao.edu/kpno/manuals/l2mspect/node1.html

[52] http://www.not.iac.es/instruments/alfosc

[53] http://www.tng.iac.es/instruments/lrs

[54] http://www.ing.iac.es/Astronomy/instruments/isis/index.html

[55] http://unwise.me

Table 1
Properties of the Different Imaging Surveys

Survey	Spectral Range (Å)	Filters	Depth (mag)	Pixel Scale ($''$/px)	FWHM(PSF) ($''$)	Ref.
GALEX	1542–2274	FUV, NUV	20, 21	1.5	5–6	1
SDSS	3595–8897	u', g', r', i', z'	22.2, 23.1, 22.7, 22.2, 20.7	0.396	1.3–1.5	2
PS1	4776–9603	$g_{\rm PS1}$, $r_{\rm PS1}$, $i_{\rm PS1}$, $z_{\rm PS1}$, $y_{\rm PS1}$	23.3, 23.2, 23.1, 22.3, 21.3	0.258	1.0–1.5	3
Legacy Surveys	4635–9216	g, r, z	24.0&24.7, 23.5&23.9, 22.5&23.0	0.262	1.1–1.3	4
2MASS	12350–21590	J, H, K_s	17.5, 17.2, 16.9	2	2.5–3.0	5
unWISE	33526–46028	$W1$, $W2$	20.4, 19.9	2.75	6	6

Note. The depths of the images are reported for point sources at the 5σ confidence level. For the DESI Legacy Imaging Surveys, we report the depths of DR5&DR7. The spectral ranges were taken from http://svo.cab.inta-csic.es/main/index.php. The column "FWHM" reports the span of the median FWHMs of all bands.

References. (1) Bianchi et al. (2014); (2) https://www.sdss.org/dr14/imaging/other_info; (3) Chambers et al. (2016); (4) Dey et al. (2019); (5) Skrutskie et al. (2006); (6) Meisner et al. (2017).

from $0\farcs26$/px (LS and PS1) to $2\farcs75$/px (unWISE), and the FWHM intensity of the PSFs varies from $1''$ (LS and PS1) to $6''$ (unWISE; Table 1). These differences need to be taken into account to measure the total flux of galaxies and preserve intrinsic galaxy colors. The software package `LAMBDAR`[56] (Lambda Adaptive Multi-Band Deblending Algorithm in R; Wright et al. 2016) was designed for this task, to conduct consistent photometry on images that are neither pixel nor seeing matched while performing deblending, sky subtraction, and error estimation. `LAMBDAR` has three critical input parameters for each image: the PSF, the zero point, and the source catalog of the field (see below). With this information in hand, `LAMBDAR` convolves each aperture with the PSF of a given image, reprojects the PSF-matched aperture on the new pixel scale, and iteratively removes neighboring objects that are blended with the host galaxy. An example of this technique is shown in Figure 1.

PSF—The GALEX PSFs are provided by the GALEX Technical Documentation[57]. We built the PSF of the unWISE images using the parameterization of Lang (2014). For 2MASS, PS1, and SDSS images, we measured the median FWHM of point sources in each image and assumed that a PSF could be approximated by a Gaussian profile.

Zero point—We used tabulated zero points for GALEX, PanSTARRS, SDSS, and unWISE images. Specifically, we set the zero points to

1. 18.82 and 20.08 mag for GALEX FUV and NUV data (Morrissey et al. 2007), respectively;
2. 22.5 mag for SDSS images[58];
3. $25 + 2.5 \times \log(\text{exposure time})$ mag for PS1 images[59], where the exposure time is given in seconds; and
4. 22.5 mag for the unWISE $W1$ and $W2$ images (Lang 2014).

To extract the zero points of the 2MASS images, we identified stars and compared their instrumental magnitudes to the tabulated magnitudes in the 2MASS Point Source Catalog (Skrutskie et al. 2006). The 2MASS and unWISE zero points were converted from the Vega system to the AB system using the offsets reported by Blanton & Roweis (2007) and Cutri et al. (2013, their Table 3 in Section 4.4h).

Source catalog—The source catalog of each field contains the positions and aperture properties (minor and major semiaxes and the orientation of the ellipse) of the host galaxy and contaminant sources (stars, galaxies, active galactic nuclei). We obtained these properties with `Source Extractor`[60] version 2.19.5 (Bertin & Arnouts 1996) and, where needed, adjusted the size of the elliptical apertures to measure the total flux.

The photometry of the LS and CFHT images was extracted with the aperture-photometry tool presented by Schulze et al. (2018)[61]. The photometry of this software and `LAMBDAR` agrees well for galaxies that are not very extended or blended with other objects.

All measurements are presented in Table 9 in Appendix B. Measurements were corrected for Galactic extinction using the Python package `sfdmap`[62] version 0.1.1 that makes use of the Schlafly & Finkbeiner (2011) extinction maps.

3.2. Supernova Spectroscopy

We used dedicated pipelines to reduce data of different instruments: Keck/LRIS data were processed with `LPIPE` (Perley 2019), VLT/X-shooter data with the ESO X-shooter instrument pipeline[63], and Gemini data with the `Gemini IRAF package`[64]. Data from other telescopes were reduced with the software package `IRAF`[65] (Tody 1986).

The typical steps of all software packages are bias subtraction, flat-fielding, source extraction in a statistically optimal way (Horne 1986), wavelength calibration (in the air reference system), and flux calibration with spectrophotometric standard stars. In most cases, a telluric correction was attempted, too. The wavelength calibration of instruments with multiple arms, such as LRIS and Kast, can be nontrivial. This can lead to velocity offsets of $\sim$200 km s^{-1} between different arms of the instruments.

3.3. Supernova Classification

All SNe were spectroscopically classified with either the software package `Supernova Identification`[66] version

---

[56] https://github.com/AngusWright/LAMBDAR

[57] http://www.galex.caltech.edu/wiki/Public:Documentation

[58] https://www.sdss.org/dr12/algorithms/magnitudes

[59] https://outerspace.stsci.edu/display/PANSTARRS/PS1+FAQ+-+Frequently+asked+questions

[60] https://www.astromatic.net/software/sextractor

[61] https://github.com/steveschulze/Photometry

[62] https://github.com/kbarbary/sfdmap

[63] https://www.eso.org/sci/software/pipelines

[64] http://www.gemini.edu/sciops/data-and-results/processing-software

[65] https://iraf-community.github.io

[66] https://people.lam.fr/blondin.stephane/software/snid

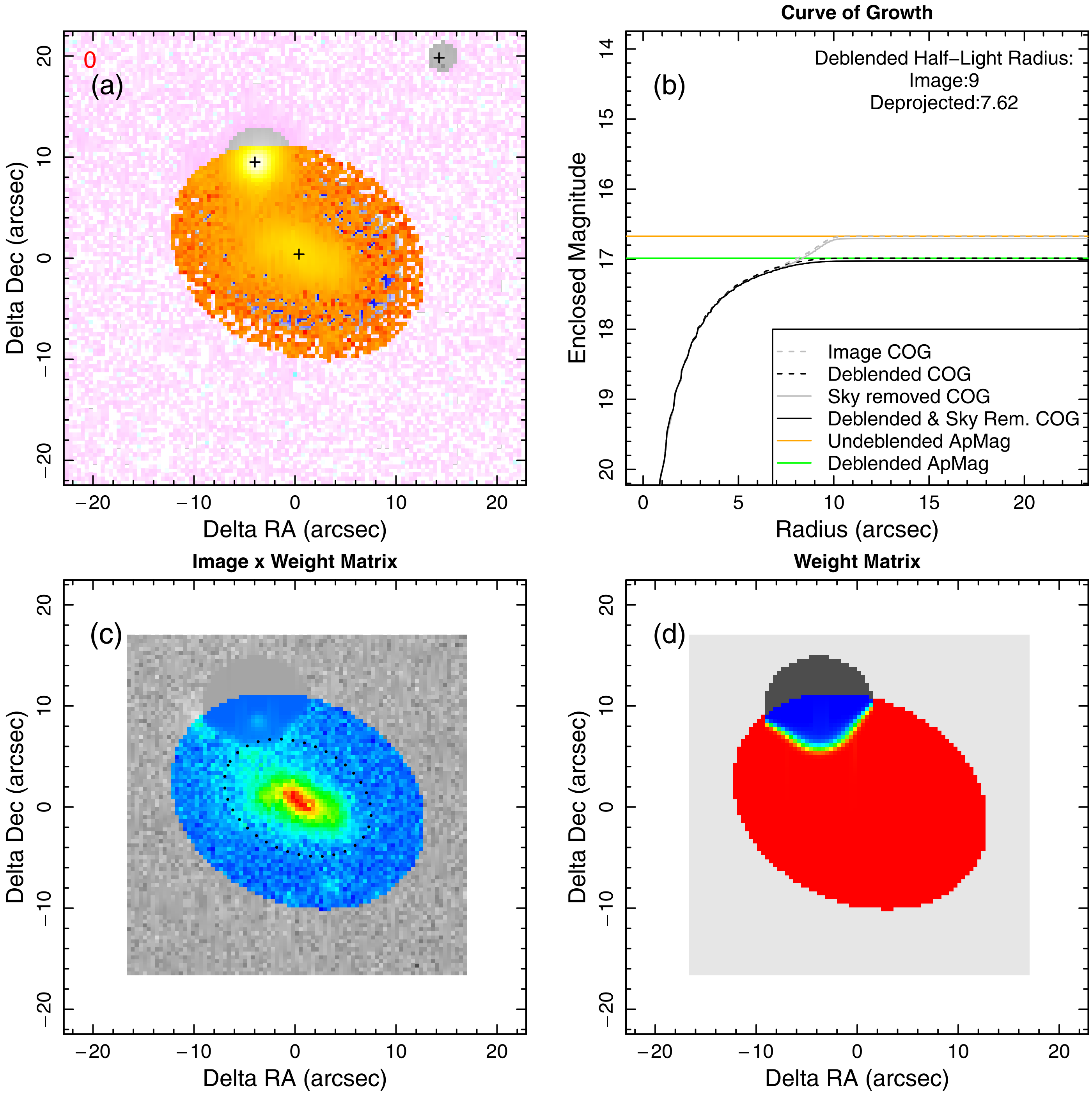

Figure 1. Example of the photometry measurement with `LAMBDAR` and the importance of deblending techniques to recover the flux of the host galaxy of PTF10fqg. Panel (a) shows the input SDSS r'-band image. Positive fluxes within the measurement aperture are shown in yellow. Pixels deemed to be part of the "sky" are indicated in pink. Panel (b) illustrates the curve of growth (CoG) of the object photometry. The gray lines indicate the radial integral of panel (a) (before deblending). The black lines show the radial integral of panel (c) (after deblending). Horizontal orange and green lines mark the measured aperture magnitude for the object before and after deblending, respectively. The text in that panel describes the circular and deprojected half-light radii, in arcseconds, with the deprojection being based on the input aperture (prior to convolution). Panel (c) shows the image stamp after deblending. The black dotted line marks the measured deblended and deprojected half-light radius. Panel (d) shows the deblend weights of the host galaxy. Colored and grayscale pixels in panels (c) and (d) mark those within and beyond the aperture, respectively. Figure adapted from Wright et al. (2016).

5.0 (`SNID`; Blondin & Tonry 2007) or `Superfit`[67] version 3.5 (Howell et al. 2005), if the host contamination was significant. For both packages, we generated template libraries that include spectra from Silverman et al. (2012), Modjaz et al. (2014), Liu et al. (2016), and Modjaz et al. (2016), and a private library built by S. Ben-Ami and extended by G. Leloudas to include superluminous supernovae (SLSNe) and other rare transients. We preferentially used spectra obtained around the time of maximum light. If not available or to break ambiguity in the classification, we used late-time data.

A minority of PTF CCSNe were classified by other teams, and we used these data if they were publicly available. In

---

[67] https://github.com/dahowell/superfit

addition, a number of PTF CCSNe were previously discussed in the literature (e.g., Fremling et al. 2018; Quimby et al. 2018; Taddia et al. 2019; Modjaz et al. 2020). For full consistency, we repeated classification of these objects using our tools.

3.4. Host-galaxy Identification

To identify the hosts, we retrieved two P48 or P60 images for each SN field: one image around the time of SN brightness maximum (PTF+SN) and one without SN contribution (PTF-SN). The PTF-SN image was chosen to have the seeing FWHM similar to the PTF+SN image and taken during dark/gray time. With both images in hand, we built the difference image (i.e., SN detection image). First, we aligned the images on the pixel level using `alipy`[68] and then subtracted the images from each other using the software `High Order Transform of Psf ANd Template Subtraction`[69] (`HOTPANTS`; Becker 2015) version 5.1.11.

After that, we aligned the world coordinate system of the PTF-SN image (usually in $r_{\rm PTF}$) to that of a host image (usually an r'-band image from LS, PS1, or SDSS) using the software `Software for Calibrating AstroMetry and Photometry`[70] (`SCAMP`; Bertin 2006) version 2.0.4 and applied the calibration of the world coordinate system on the difference image. In the final step, we built source catalogs of the host and difference images with the software `Source Extractor`. The closest object to the SN, within a reasonable distance (approximately the extent of a galaxy in the r' band plus 10 kpc), was declared as the host galaxy.

3.5. Spectral Energy Distribution Fitting

3.5.1. Description of the Method

To extract physical and phenomenological parameters of the host galaxies, we modeled the SEDs with the software package `Prospector`[71] version 0.3 (Leja et al. 2017; Johnson et al. 2019). `Prospector` uses the `Flexible Stellar Population Synthesis`[72] (`FSPS`) code (Conroy et al. 2009) to generate the underlying physical model and `python-fsps`[73] (Foreman-Mackey et al. 2014) to interface with in Python.

The SED model required assumptions for the star formation history (SFH), initial mass function (IMF), attenuation, and whether a contribution from the ionized gas should be taken into account. We used a linear-exponential SFH (functional form $t \times \exp(-t/\tau)$, where t is the age of the SFH episode and τ is the e-folding timescale), the Chabrier (2003) IMF, the Calzetti et al. (2000) attenuation model, and the Byler et al. (2017) model for the ionized gas contribution.

The priors were set as distribution functions with broad ranges as specified in Table 2. The physical parameters mass, SFR, age, e-folding timescale of the SFH, extinction, and metallicity were inferred in a Bayesian way by sampling the posterior probability functions with the dynamic nested sampling package `dynesty`[74] (Speagle 2020). For each model parameter, we report the median values of the marginalized posterior probability functions and their 1σ confidence intervals.

Table 2
Model Parameters and Their Priors of the Galaxy SED Modeling

Property	Type	Range
Galaxy mass ($\log M_\star/M_\odot$)	Uniform	5–13
V-band optical depth (τ_V)[a]	Uniform	0–8
Stellar metallicity ($\log Z/Z_\odot$)	Uniform	−2–0.5
Age of the SF episode ($t_{\rm age}$/Gyr)	LogUniform	0.001-13.8
e-folding timescale of the star formation episode (τ/Gyr)	LogUniform	0.1–100

Notes.
[a] The optical depth in the V band was converted to the selective-to-total extinction via $E(B-V) = 1.086 \times \tau_V/\kappa(V)$, where $\kappa(V)$ is the V-band opacity of the Calzetti et al. (2000) attenuation model.

We remark that our SED model assumes that stars evolve in single-star systems. However, Sana et al. (2012) concluded that >70% of all massive stars live in binary systems. This could affect galaxy spectra. Indeed, state-of-the-art population synthesis codes predict a significant impact of binary evolution on the stellar continuum and particularly on the emission-line fluxes both in young star-forming galaxies (e.g., Eldridge et al. 2017) and in galaxies with little-to-no ongoing star formation (e.g., Chen et al. 2015). Quantifying the impact of binary evolution on the host-galaxy properties is beyond the scope of this paper and is left for future work.

3.5.2. Quality of the SED Modeling

Figure 2 shows examples of the observed SEDs and their fits with `Prospector`. The average galaxy SED is observed in 13 bands from the far-ultraviolet (FUV) to the mid-infrared (MIR). After accounting for similarities between SDSS and PS1 filters, each SED has, on average, nine measurements. Our assumed model in `Prospector` provides an adequate description of most SEDs (e.g., Figure 2). The median χ^2 divided by the number of filters (n.o.f.) is 0.9. A minority of ∼3% have a reduced χ^2 between 3 and 12. Nonetheless, these fits are still useful (Figure 15 in Appendix C). The large reduced χ^2 is driven by (i) individual or a small number of data points with small measurement errors or elevated scatter (∼ 44%), (ii) artifacts in PanSTARRS images in the case of very extended galaxies[75] (∼ 26%), (iii) a mismatch between observed and model-predicted magnitudes in the case of low-mass galaxies with emission-line-dominated spectra (∼ 26%), and (iv) deblending issues (∼ 1%).

The derived physical parameters, such as galaxy mass ($M_\star$), SFR, and specific star formation rate (sSFR; = SFR/$M_\star$), are comparable to those of other galaxy samples and broadly consistent with results from the literature (Leloudas et al. 2015; Schulze et al. 2018; Modjaz et al. 2020; Taggart & Perley 2021). The galaxy masses and the SFRs are 0.1–0.2 dex smaller compared to the values reported by Schulze et al. (2018), Modjaz et al. (2020), and Taggart & Perley (2021), even if identical data sets are used. The bias-corrected rms of the galaxy mass, SFR, and sSFR vary between 0.3 and 1.3 dex. The uncertainties of the rms values reach up to 0.8 dex, making most of these differences statistically insignificant. Differences

---

[68] https://github.com/japs/alipy
[69] https://github.com/acbecker/hotpants
[70] https://www.astromatic.net/software/scamp
[71] https://github.com/bd-j/prospector
[72] https://github.com/cconroy20/fsps
[73] http://dfm.io/python-fsps/current/#
[74] https://github.com/joshspeagle/dynesty
[75] https://outerspace.stsci.edu/display/PANSTARRS/PS1+Image+artifacts+and+anomalies

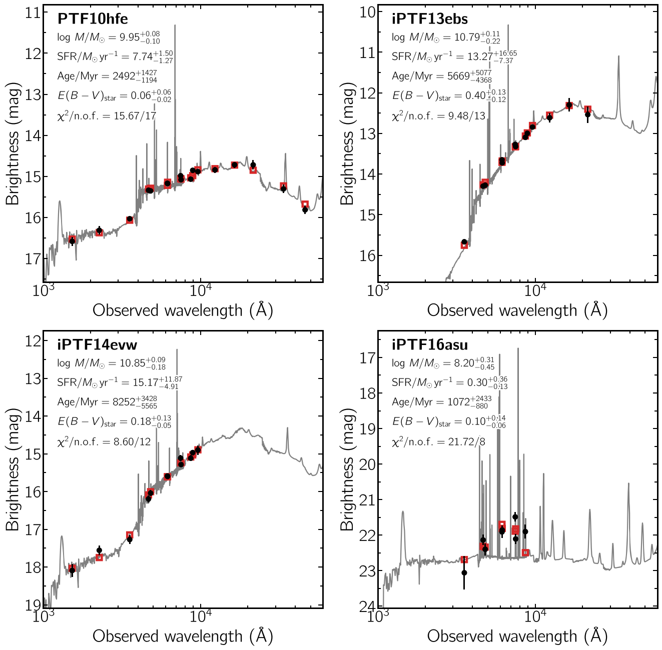

Figure 2. Selection of SEDs of SN host galaxies from 1000 to 60,000 Å (detections •; upper limits ▼). The solid line displays the best-fitting model of the SED. The squares represent the model-predicted magnitudes. The fitting parameters are shown in the upper-left corner. The abbreviation "n.o.f." stands for numbers of filters.

are also expected; they are due to the assumptions of the SED model (e.g., the nebular emission module, SFHs, stellar population synthesis models) and assumptions inherent to the SED modeling software packages.

3.5.3. Impact of Wavelength Coverage

Among the 876 identified SN host galaxies, 532 hosts are detected in the rest-frame UV (<3000 Å), 701 in the rest-frame near-infrared (NIR; >10000 Å), and 70 only in the optical (4000–10000 Å).[76] To quantify the systematic uncertainties in the galaxy mass, SFR, sSFR, ages, and attenuation measurements owing to the absence of individual spectral bands, we define a subsample of 475 host galaxies with detections in the UV, in the range 3000–4000 Å, and the NIR (all rest frame). Then, we removed one or more of these spectral bands and repeated the fit. The scatter plots in Figure 3 show how the galaxy mass, SFR, sSFR, age of the stellar population, and attenuation vary if only partial data sets are available.

The galaxy mass (first column in Figure 3) is the most robustly measured quantity and shows no dependence on the availability of NIR data. The bias levels between the measurements are negligible and the rms values are <0.1 dex. In comparison, the median error of the mass measurements is a factor of 2 larger if the full data set is used. This confirms findings by (Conroy 2013, and references therein). These authors also pointed out that NIR data are only constraining if dust reddening is significant and larger than in our CCSN sample. Furthermore, galaxies with ages between 0.1 and 1 Gyr and in particular starbursts have very uncertain mass-to-light ratios owing to the difficulty in constraining their SFH. As we show in Section 4.6, 4.5% of the entire PTF-SN sample is found in starburst galaxies. Their galaxy mass estimates can have larger systematic uncertainties than those reported here if rest-frame NIR data are not available.

In contrast to the robustness of the mass estimates, SFR measurements (second column in Figure 3) are on average overestimated by 0.2 dex if SEDs consist of only rest-frame UV +optical data, and underestimated by 0.3 dex if SEDs only consist of rest-frame optical+NIR data. SFR measurements are also more uncertain, which is illustrated by their large rms of 0.5–0.7 dex and the uncertainties of the rms values if UV and/or *U*-band data are lacking (Figure 3). The systematic offset of the SFRs by ∼0.2 dex of UV+optical is in agreement with Conroy et al. (2009). SFRs are more challenging to measure from SEDs because of the age–dust–metallicity degeneracy and the assumed SFHs. In addition, prominent emission lines in low-mass galaxies add a source of uncertainty to measuring SFRs accurately. Consequently, the uncertainties of the sSFRs increase (third column in Figure 3).

The fourth column in Figure 3 presents the dependence of the inferred ages on the wavelength coverage. The absence of wavelength regimes leads to an underestimation of the age of the stellar population. The ages derived from sole optical SEDs are skewed by 0.2 dex toward younger ages. This additional systematic error is smaller than the total error of the age measurements with full wavelength coverage. Although individual age measurements are notoriously difficult to measure accurately and precisely, there is a strong linear correlation between the ages derived from SEDs with complete and partial data sets. This means that we can compare the average ages of the SN host populations and use that to conclude whether an SN class is characterized by a particularly young or old stellar population.

The attenuation measurements (fifth column in Figure 3) are systematically overestimated if incomplete SEDs are used. Pure optical SEDs are affected most, and these attenuation measurements are overestimated by 0.08 mag. The rms is also of the same order. In contrast to the ages, the bias levels of the attenuation measurements are comparable to individual measurement errors. Furthermore, the median attenuation of SEDs with maximal wavelength coverage is 0.16 mag. This makes these measurements an unsuitable diagnostic to distinguish between different SN host populations.

4. Results

4.1. Supernova Classifications

Our input sample includes over 900 transients that were flagged as CCSNe on the PTF Marshal, a target and observation manager system. Among those, we robustly classify 888 objects using the methods described in Section 3.3. We divide the sample into 3 SN families and 12 SN classes: H-poor SNe—SLSN-I, SN Ic-BL, SN Ic, SN Ibc, SN Ib; H-rich SNe—SLSN-IIb, SLSN-II, SN IIb, SN II; and interacting SNe—SLSN-IIn[77], SN IIn, SN Ibn. Figure 4 shows examples of the SN spectra and the characteristic features. Table 3 summarizes the classifications and properties of the 888 CCSNe.[78]

---

[76] We declare a host as detected in a given band if the measurement error is <0.44 mag, i.e., a 2σ measurement.

[77] We use the classifications from G. Leloudas et al. (2021, in preparation) and added other luminous SNe IIn to this class. The origin of this class and its relationship to regular SNe IIn is highly debated (Gal-Yam 2012; Moriya et al. 2019; Gal-Yam 2019; Jerkstrand et al. 2020; Nicholl et al. 2020).

[78] Parallel to this paper, L. Hangard et al. (2021, in preparation) classified all SNe that were flagged as an SN Ia on the PTF Marshal.

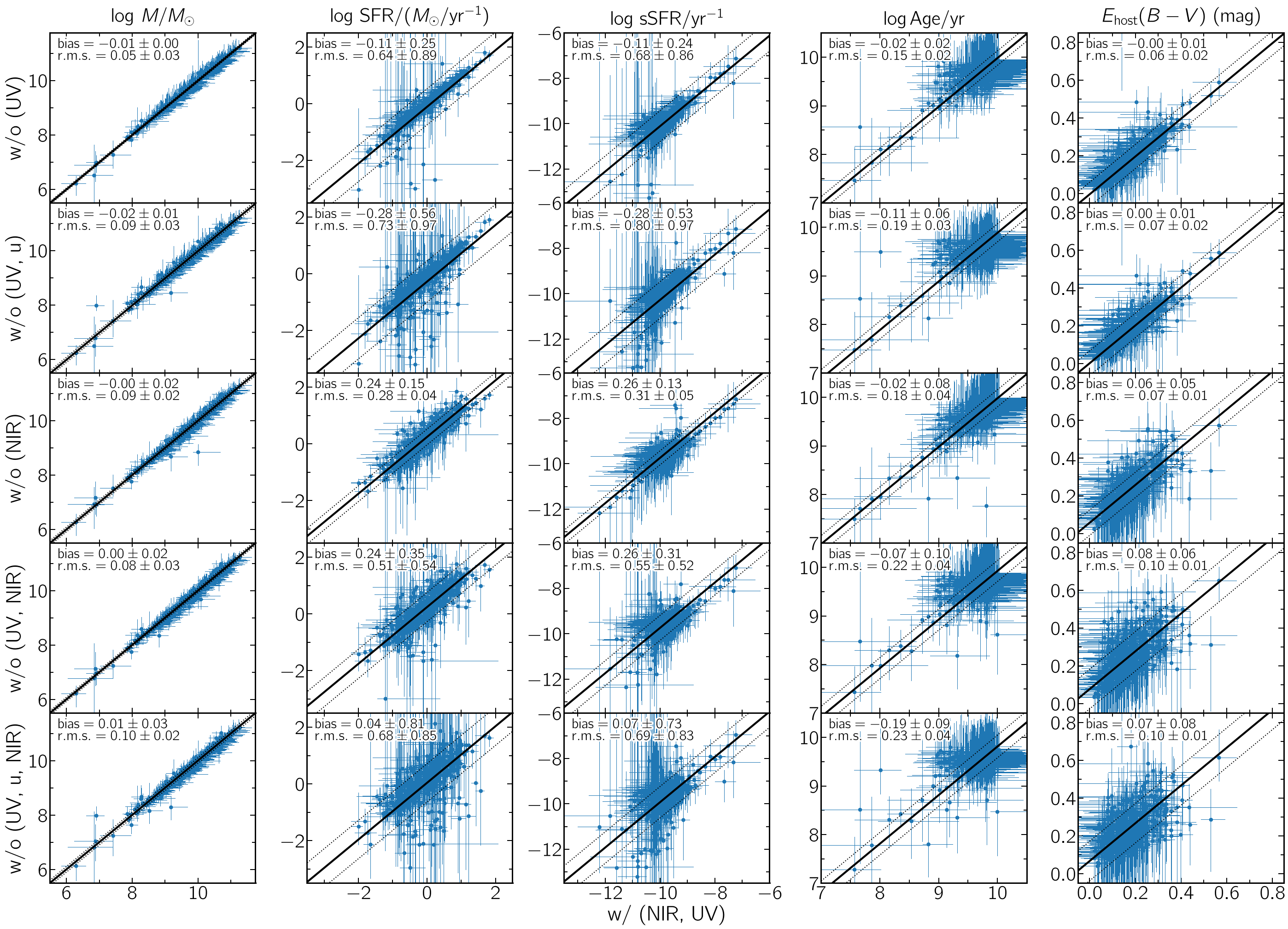

Figure 3. Comparison of various host properties derived from galaxy SEDs with detections in the UV, *U* band, optical, and NIR (all rest frame) and after removing one or more spectral regimes. The galaxy mass is the most robustly measured property (negligible bias and an rms of <0.1 dex). In contrast to that, the other parameters are sensitive to the wavelength coverage of the SEDs.

In addition, we make use of the classifications of SLSNe reported by Yan et al. (2015), Perley et al. (2016), Yan et al. (2017), Quimby et al. (2018), De Cia et al. (2018), Lunnan et al. (2018), and G. Leloudas et al. (2021, in preparation); SNe Ic-BL by Taddia et al. (2019) and Modjaz et al. (2020); SNe Ibc by Fremling et al. (2018) and Barbarino et al. (2020); SNe IIn by Nyholm et al. (2020); CCSNe in general by Arcavi et al. (2010); and tidal disruption events (TDEs) by Arcavi et al. (2014). In most cases, our classifications are identical to those reported in the papers mentioned above. For a few objects, we prefer a different classification. Information about those objects is provided in Appendix D.

Figure 5 displays the breakdown of our sample. It consists of ∼63% H-rich and ∼22% H-poor SNe. The remaining ∼15% exhibit signatures of strong interaction between the SN ejecta and circumstellar matter. The largest individual SN class in the PTF sample is Type II SNe with 56% due to their high volumetric rate (Li et al. 2011) and their long-lasting plateaus, which are less demanding for spectroscopic follow-up observations. On the other extreme, the Type Ibn SN sample contains only nine objects. Their light curves reach maxima within $\lesssim 10$ days and afterward decline by $\sim 0.1\,{\rm mag\,day}^{-1}$ (Hosseinzadeh et al. 2017). Therefore, in order to classify them, spectroscopic observations within a few days after discovery are essential.

4.2. Host-galaxy Recovery Rate

We detect the host galaxies of almost all CCSNe.[79] Only 10 hosts evaded detection; this set includes four SLSNe-I and one candidate SLSN-IIn, two SNe IIb, and one Type Ic-BL, Ic, and IIn SN each.[80] Three of the five SLSNe were found between redshift $z = 0.4$ and $z \approx 1$, and are expectedly beyond the reach of the Legacy Surveys (Figure 8; Table 1; Lunnan et al. 2014; Perley et al. 2016; Schulze et al. 2018; Angus et al. 2019). The fields of the five regular CCSNe were also covered by the Legacy Surveys, except for PTF12grr. Their nondetections in data from the Legacy Surveys, PanSTARRS, and SDSS imply luminosities of $M_R \gtrsim -13.6$ mag. As we show in Section 4.4, these host galaxies are among the faintest galaxies in our sample.

---

[79] We declare a host as detected if the measurement error in any image is better than 0.44 mag, i.e., a 2σ measurement.

[80] SLSNe-I: iPTF13bdl, 14tb, 15ii, 16bt; candidate SLSN-IIn: PTF10eoo; SNe IIb: PTF09dsj, 13dzy; SN Ic-BL: PTF12grr; SN Ic: iPTF14gqr; SN IIn: PTF10weh.

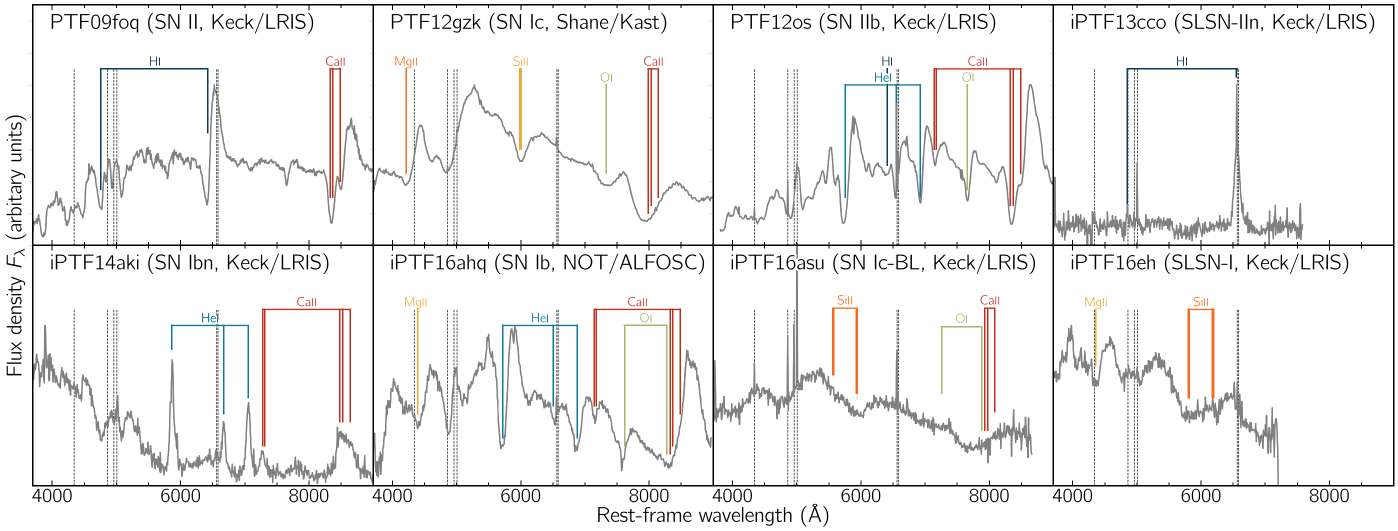

Figure 4. A collage of SN classification spectra. Overlaid are absorption and emission lines that are characteristic of each class. The black vertical dashed lines indicate the locations of expected emission lines from the underlying H II regions in the host galaxies. For presentation purposes, all spectra were rebinned to bin sizes of 8 Å.

Figure 6 shows postage stamps of a selection of fields in our sample. The blue circles mark the host galaxies' centers, and red crosshairs indicate the SN positions. The average total alignment error is 0″16 and only exceeds 0″5 in six cases. The coordinates of the SNe, host galaxies, and their projected distances to each other are summarized in Table 3.

We remark that the host identification of two SNe has some ambiguity. iPTF14gqr exploded in the outskirts of tidally interacting galaxies. As proposed by De et al. (2018), the tidal interaction could trigger star formation in collisional debris. We assume that the progenitor of iPTF14gqr was formed in such debris.

PTF12mja is located between two galaxies of a compact galaxy group (McConnachie et al. 2009). Spectroscopic information would be required to obtain the redshifts of the two galaxies and to identify the actual host. The host of PTF09bce is severely blended with another galaxy so that measuring the host flux alone is not possible. Owing to that, we do not include PTF09bce and 12mja in the discussion of the host properties.

4.3. Redshift and Distance Measurements

About 45% of the PTF CCSN host galaxies have redshift information listed in the SDSS catalog or the NASA/IPAC Extragalactic Database[81] (NED; Helou et al. 1991). Spectra of 333 additional SNe (∼38%) show absorption or emission lines from their host galaxies. The remaining 18% (158 SNe) have no redshift information. For those, we use the redshifts inferred by SN-template matching. These redshifts are typically accurate to within a few hundredths in redshift space (Blondin & Tonry 2007; Fremling et al. 2020). Table 3 summarizes all redshifts and how they are obtained.

Figure 7 displays the redshift distribution of each SN class (see also Table 5 for their median values). The median redshifts reflect the average luminosity of each class. Type Ibc, II, and IIb SNe have the lowest peak luminosities and are found only at low redshifts (median $z \approx 0.04$; Table 5). In contrast, SLSNe are detected at a median $z \approx 0.26$ (Table 5). The most distant CCSN in our sample (iPTF14tb) is, in fact, a H-poor SLSN at $z = 0.942$ (Table 3). The measured redshift distributions are confirmed with previous work by Perley (2019), Nyholm et al. (2020), and Modjaz et al. (2020), which are based on subsets of the PTF SLSN, SN IIn, and SN Ic-BL host-galaxy samples.

At very low redshift, peculiar velocities of galaxies can be significant and can hinder using redshifts as distance measurements (e.g., Davis et al. 2011). To quantify the impact of this issue, we compare the distance moduli inferred from the Tully–Fisher (TF) relation and ΛCDM cosmology without correction for peculiar motion. The NED database has a record of the distance moduli from the TF relation for 24 of 27 hosts at $z < 0.01$.[82] The distance moduli from ΛCDM cosmology and the TF relation differ by $0.18^{+0.71}_{-0.68}$ mag on average. This is smaller than the accuracy of the TF relation (0.3–0.4 mag; Freedman & Madore 2010). Given the general consistency between the distances inferred from ΛCDM cosmology and from the TF relation, we assume that all hosts are in the Hubble flow and that redshifts are a reliable distance measurement for all objects in this paper.[83]

4.4. Brightness and Luminosity

The top panel of Figure 8 shows the distribution of the hosts' observed r'-band brightness as a function of redshift and SN class. The distributions cover a wide range from $r' \approx 8$ mag to $r' \approx 26$ mag. Clear differences between the different SN classes are visible. Type Ib, Ic, IIb, and II SNe are found in galaxies with a median brightness of $r' \approx 16.6$ mag (horizontal line in the top panel of Figure 8; Table 5), whereas Type IIn/Ibn SNe are found in galaxies that are on average 1.5 mag

---

[81] http://ned.ipac.caltech.edu

[82] We limit the comparison to $z < 0.01$ because the completeness level of hosts with TF distance moduli plunges from ∼89% to 30% (23/76 hosts) as we go from $z < 0.01$ to $0.01 \leqslant z < 0.02$.

[83] The differences in the distance moduli of the hosts of iPTF14jku, 14ur, 14va, 15eqv, 16hgm, and 16tu differ by 1 to 2 mag. The TF distance moduli of iPTF15eqv and 16tu can be reconciled with their large measurement uncertainties. Understanding whether the differences of the other objects are significant requires knowledge of how the TF distances were obtained, but that is beyond the scope of this paper.

Table 3
PTF CCSN Sample

PTF	IAU Name	Type	Redshift	Method	R.A. (SN) (hh:mm:ss)	Decl. (SN) (dd:mm:ss)	R.A. (Host) (hh:mm:ss)	Decl. (Host) (dd:mm:ss)	Offset ($''$)	Offset (kpc)	$E_{\rm MW}(B-V)$ (mag)
09as	2009cb	SLSN-I	0.1866	3	12:59:15.862	+27:16:40.80	12:59:15.870	+27:16:40.71	0.15 ± 0.18	0.48 ± 0.57	0.01
09atu	⋯	SLSN-I	0.5010	3	16:30:24.537	+23:38:25.59	16:30:24.544	+23:38:25.52	0.11 ± 0.16	0.69 ± 0.99	0.04
09awk	⋯	SN Ib	0.0616	3	13:37:56.358	+22:55:04.78	13:37:56.359	+22:55:04.78	0.02 ± 0.17	0.02 ± 0.20	0.02
09axi	⋯	SN II	0.0640	3	14:12:40.850	+31:04:03.89	14:12:40.943	+31:04:03.40	1.29 ± 0.11	1.64 ± 0.14	0.01
09bce	⋯	SN II	0.0234	3	16:35:17.680	+55:37:59.33	16:35:17.657	+55:38:01.54	2.21 ± 0.11	1.08 ± 0.05	0.01
09bcl	⋯	SN II	0.0600	4	18:06:26.809	+17:51:43.15	18:06:26.442	+17:51:42.67	5.26 ± 0.06	6.30 ± 0.07	0.08
09be	⋯	SN II	0.1020	4	14:10:18.538	+16:53:38.71	14:10:18.493	+16:53:38.53	0.66 ± 0.25	1.28 ± 0.48	0.02
09bgf	⋯	SN II	0.0318	3	14:41:38.329	+19:21:43.80	14:41:38.351	+19:21:43.19	0.68 ± 0.14	0.45 ± 0.10	0.02
09bw	2009cw	SN Ib	0.1470	3	15:05:01.990	+48:40:03.49	15:05:02.035	+48:40:03.23	0.52 ± 0.12	1.37 ± 0.33	0.02
09cjq	⋯	SN II	0.0193	1	21:16:28.502	+00:49:39.70	21:16:27.606	+00:49:34.77	14.32 ± 0.14	5.79 ± 0.05	0.06
09cnd	⋯	SLSN-I	0.2583	3	16:12:08.838	+51:29:16.02	16:12:08.838	+51:29:15.49	0.53 ± 0.44	2.19 ± 1.82	0.02
09ct	2009cv	SN IIn	0.1560	3	11:42:13.827	+10:38:54.19	11:42:13.843	+10:38:53.87	0.40 ± 0.40	1.11 ± 1.13	0.03
09cu	2009ct	SN II	0.0569	1	13:15:23.135	+46:25:09.16	13:15:23.897	+46:25:13.47	8.98 ± 0.22	10.24 ± 0.25	0.01
09cvi	⋯	SN II	0.0360	4	21:47:09.947	+08:18:35.35	21:47:09.925	+08:18:35.55	0.38 ± 0.20	0.28 ± 0.15	0.07
09cwl	2009jh	SLSN-I	0.3500	3	14:49:10.108	+29:25:11.68	14:49:10.177	+29:25:12.78	1.42 ± 0.20	7.21 ± 1.04	0.01
09dah	⋯	SN IIb	0.0238	3	22:45:17.094	+21:49:15.27	22:45:17.102	+21:49:15.29	0.12 ± 0.07	0.06 ± 0.03	0.05
09dfk	⋯	SN Ib	0.0158	3	23:09:13.427	+07:48:15.31	23:09:13.483	+07:48:16.58	1.52 ± 0.13	0.51 ± 0.04	0.05
09dh	2009dr	SN Ic	0.0770	4	14:44:42.072	+49:43:45.17	14:44:42.105	+49:43:45.94	0.84 ± 0.08	1.26 ± 0.12	0.02
09dra	⋯	SN II	0.0766	1	15:48:11.483	+41:13:28.68	15:48:11.318	+41:13:31.54	3.42 ± 0.17	5.12 ± 0.25	0.01

Note. The IAU names were retrieved from the Transient Naming Server (https://wis-tns.weizmann.ac.il). The redshifts were obtained either from SDSS (method = 1), the NASA Extragalactic Database (method = 2), galaxy lines in SN spectra (method = 3), or SN-template matching (method = 4). The SN coordinates were measured after aligning SN and host images (for details see Sections 3.4, 4.2). The coordinates are reported in a conventional celestial reference system in the J2000.0 system.

(This table is available in its entirety in machine-readable form.)

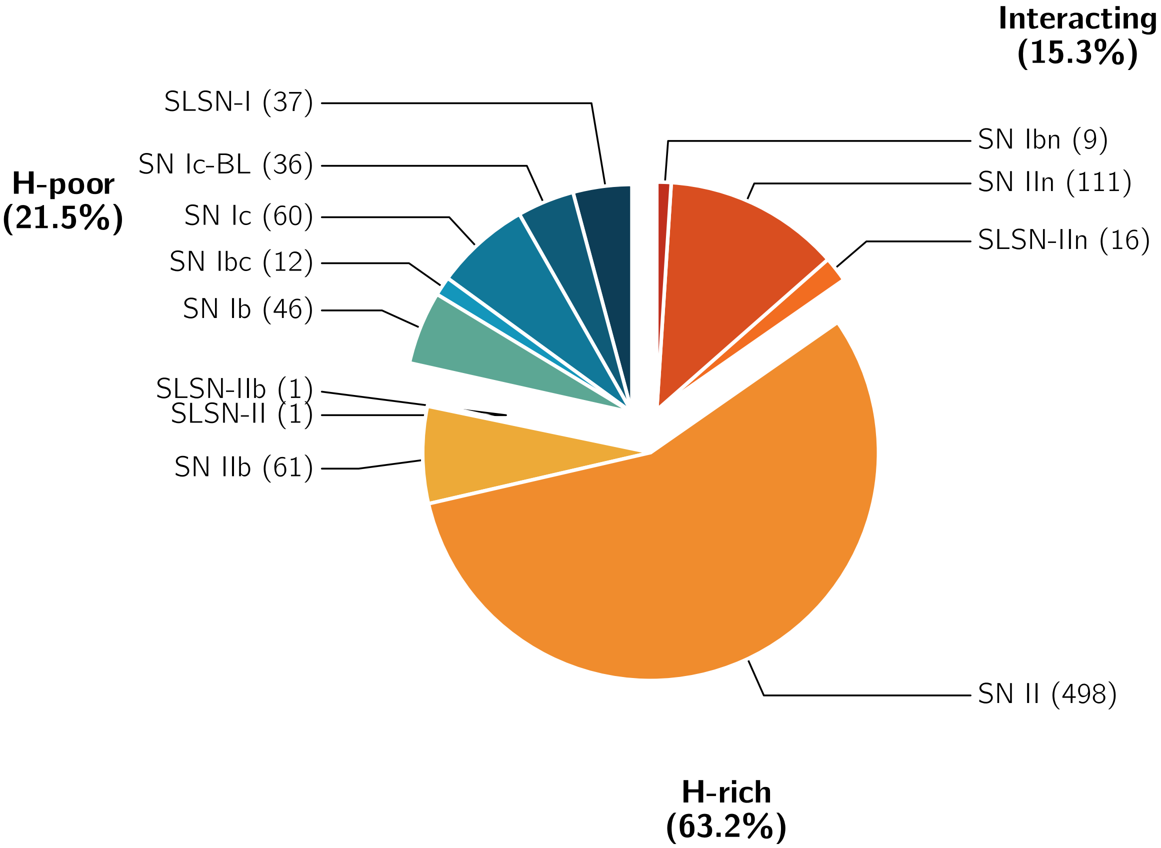

Figure 5. The PTF CCSN sample consists of 888 objects divided into 3 families and 12 classes. The size of each subclass and family is shown in the legend.

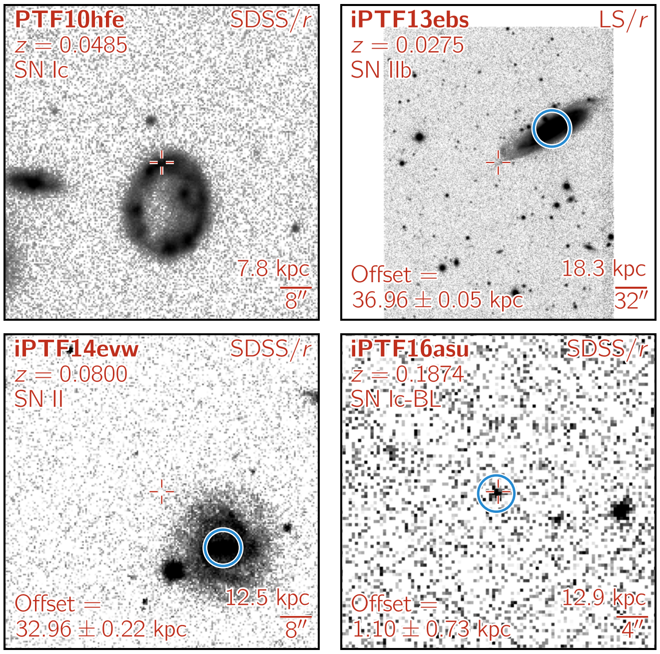

Figure 6. Selection of postage stamps of PTF CCSN host galaxies. The size of the cutouts varies between 40″ and 320″. In each panel, north is up and east is to the left. The crosshair marks the SN position, and the blue circle (arbitrary radius) marks the center of the host galaxy. The projected distance (in kiloparsec) between an SN and the center of its host galaxy is reported in the lower-left corner. A scale is shown in the lower-right corner. We report no distance between PTF10hfe and its host because the host galaxy has a ring morphology without a center.

fainter and SLSNe in galaxies that are ~6.3 mag fainter (Table 5).

A significant part of the differences can be attributed to the redshift intervals probed by the different SN populations. To corroborate this, we display the *B*-band luminosities in the bottom panels of Figure 8. Similar to the top panels, the horizontal lines display the median values of the probability distribution functions reported in Section 5.1 and summarized in Table 5. The *K*-corrected absolute magnitudes of SN IIn/Ibn hosts are almost identical to the hosts of SNe Ibc, SNe IIb, and SNe II. SLSNe and SNe Ic-BL exhibit a preference for low-luminosity galaxies, even after accounting for the evolution of the *B*-band luminosity function, in agreement with Lunnan et al. (2014), Leloudas et al. (2015), Perley et al. (2016), Chen et al. (2017a), Schulze et al. (2018), and Modjaz et al. (2020). Their median luminosities are between $M_B = -17.6$ and -18.3 mag, and a factor of ~2.4–5 lower than those of regular CCSN host galaxies (Table 5). The median luminosity of H-poor SLSN host galaxies is comparable to that of the Large Magellanic Cloud (LMC) at $z \approx 0$ (de Vaucouleurs 1960; McConnachie 2012).

The luminosity distribution of detected hosts extends from $M_B \approx -11$ to -23 mag. This interval covers the range from $10^{-4}\,L_\star$ to $10\,L_\star$, where $L_\star$ is the knee of the *B*-band luminosity functions reported by Ilbert et al. (2005). The least-luminous detected hosts in our sample are PTF09gyp (SN IIb, $M_B = -11.2^{+0.6}_{-0.4}$ mag; Table 4) and iPTF14ajx (SN IIn, $M_B = -11.4^{+0.3}_{-0.2}$ mag; Table 4). Including the SN hosts that evaded detection extends the distribution to galaxies

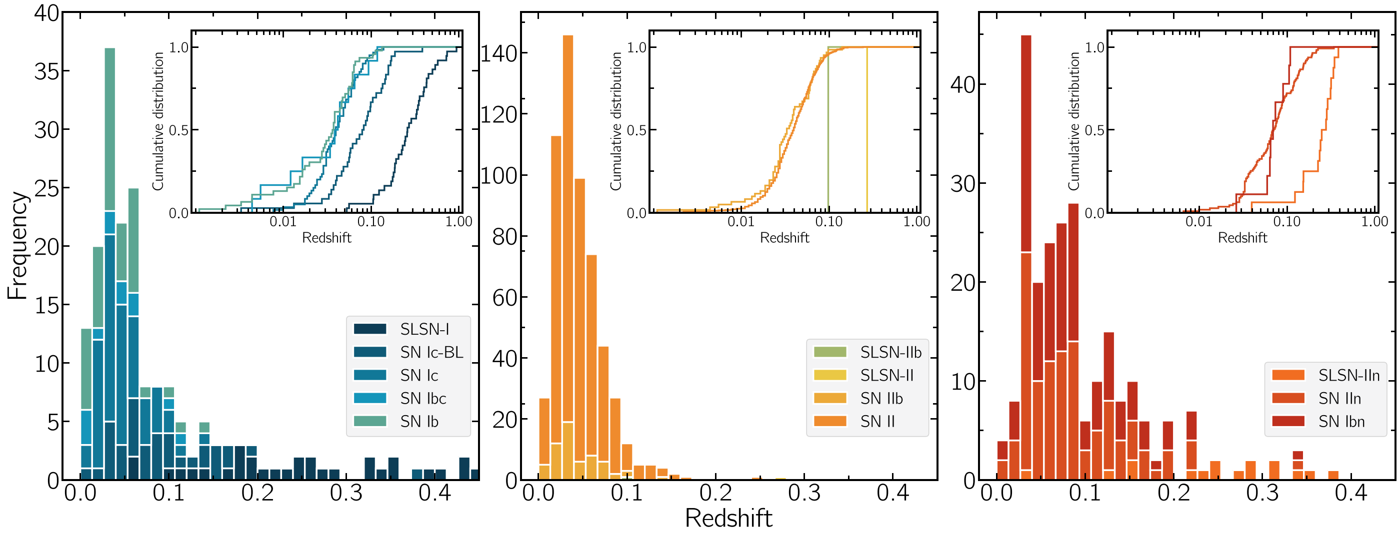

Figure 7. The redshift distribution of H-poor (left), H-rich (center), and interaction-powered (right) SNe. The stacked histograms are truncated at $z = 0.5$ for presentation purposes, whereas the full distributions are shown as cumulative plots in the insets. The highest-redshift SN in the PTF sample is the H-poor SLSN iPTF14tb at $z = 0.942$.

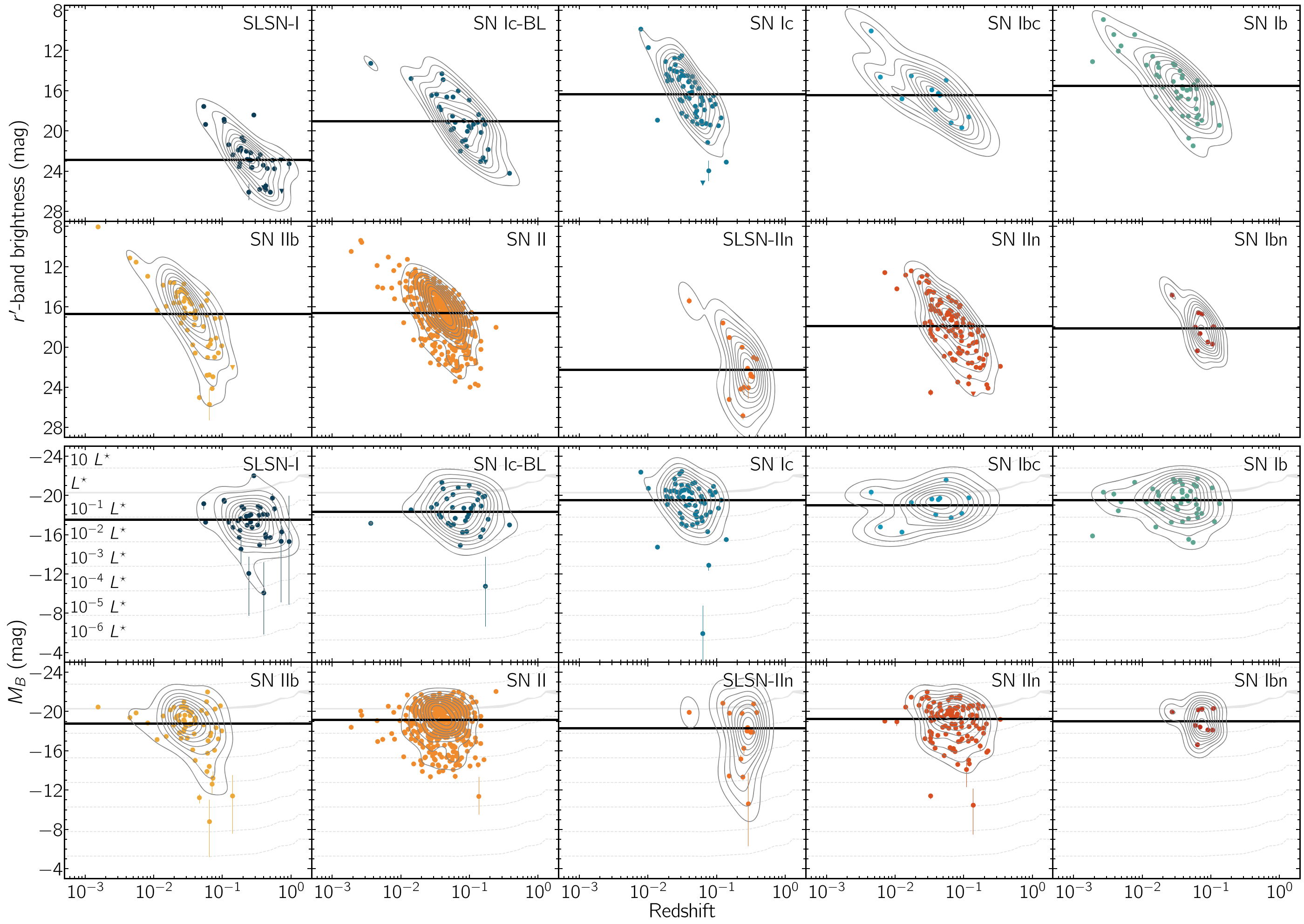

Figure 8. The evolution of the apparent r' magnitude (top) and absolute B magnitude (bottom) of the host-galaxy populations as a function of redshift and SN type. The average brightness (indicated by the black horizontal line) varies significantly with each SN type. These dissimilarities are primarily due to differences in the redshift distributions. After accounting for redshift, SLSNe-I are found in galaxies that are still a factor of 4.5 less luminous than SNe II. To guide the eye, contours from a kernel density estimate from 10% to 90% are overlaid in both figures. The characteristic luminosity, $L^{\star}$, of the B-band luminosity function of star-forming galaxies presented by Faber et al. (2007) and multiplies of it are displayed in gray.

Table 4

Results from the Host-galaxy SED Modeling with `Prospector`

PTF	Type	Redshift	χ^2/n.o.f.	$E_{\mathrm{host}}(B-V)$ (mag)	M_{FUV} (mag)	M_{B} (mag)	M_{Ks} (mag)	log SFR ($M_\odot$ yr^{-1})	log M ($M_\odot$)	log sSFR (yr^{-1})	Age (Gyr)
09as	SLSN-I	0.1866	8.21/9	0.20 ± 0.05	$-16.20^{+0.16}_{-0.10}$	$-17.62^{+0.11}_{-0.07}$	$-17.96^{+0.31}_{-0.28}$	$-0.22^{+0.28}_{-0.23}$	$8.19^{+0.36}_{-0.57}$	$-8.40^{+0.82}_{-0.55}$	$0.58^{+1.57}_{-0.50}$
09atu	SLSN-I	0.5010	2.94/7	0.23 ± 0.14	$-14.48^{+0.72}_{-0.58}$	$-15.70^{+0.27}_{-0.19}$	$-15.82^{+0.69}_{-0.64}$	$-0.59^{+0.72}_{-0.63}$	$6.84^{+0.70}_{-0.49}$	$-7.43^{+1.03}_{-1.15}$	$0.06^{+0.81}_{-0.05}$
09awk	SN Ib	0.0616	7.13/15	$0.19^{+0.15}_{-0.06}$	$-17.11^{+0.40}_{-0.14}$	$-19.07^{+0.12}_{-0.04}$	$-19.73^{+0.09}_{-0.16}$	$-0.14^{+0.51}_{-0.23}$	$9.56^{+0.12}_{-0.27}$	$-9.69^{+0.92}_{-0.27}$	$3.98^{+4.45}_{-2.86}$
09axi	SN II	0.0640	7.90/10	$0.13^{+0.23}_{-0.09}$	$-16.04^{+0.68}_{-0.53}$	$-18.47^{+0.22}_{-0.04}$	$-18.96^{+0.16}_{-0.43}$	$-0.82^{+1.01}_{-0.71}$	$9.17^{+0.12}_{-0.17}$	$-9.98^{+1.27}_{-0.71}$	$1.86^{+2.25}_{-0.99}$
09bce	SN II	0.0234	…	…	…	…	…	…	…	…	…
09bcl	SN IIn	0.0600	1.97/10	$0.20^{+0.14}_{-0.12}$	$-13.16^{+1.04}_{-3.99}$	$-21.19^{+0.39}_{-0.28}$	$-23.17^{+0.17}_{-0.07}$	$-2.62^{+3.12}_{-8.82}$	$11.09^{+0.18}_{-0.34}$	$-13.67^{+3.75}_{-8.90}$	$5.81^{+4.39}_{-3.48}$
09be	SN II	0.1020	0.23/3	$0.33^{+0.17}_{-0.16}$	$-12.75^{+1.03}_{-0.76}$	$-14.45^{+0.29}_{-0.22}$	$-14.95^{+0.58}_{-0.66}$	$-0.91^{+0.71}_{-0.65}$	$6.51^{+0.66}_{-0.42}$	$-7.39^{+0.92}_{-1.15}$	$0.05^{+0.74}_{-0.05}$
09bgf	SN II	0.0318	11.37/14	$0.04^{+0.08}_{-0.03}$	$-16.18^{+0.28}_{-0.13}$	$-17.49^{+0.15}_{-0.06}$	$-17.76^{+0.20}_{-0.13}$	$-1.01^{+0.21}_{-0.11}$	$8.67^{+0.14}_{-0.26}$	$-9.68^{+0.52}_{-0.19}$	$4.68^{+5.48}_{-3.49}$
09bw	SN II	0.1470	4.76/11	$0.17^{+0.09}_{-0.05}$	$-16.63^{+0.80}_{-0.29}$	$-18.54^{+0.09}_{-0.06}$	$-19.46^{+0.26}_{-0.13}$	$-0.24^{+0.28}_{-0.29}$	$9.31^{+0.14}_{-0.43}$	$-9.56^{+0.78}_{-0.34}$	$4.81^{+5.20}_{-3.90}$
09cjq	SN II	0.0193	25.25/17	$0.19^{+0.10}_{-0.05}$	$-17.98^{+0.44}_{-0.12}$	$-20.93^{+0.12}_{-0.04}$	$-22.47^{+0.13}_{-0.06}$	$0.30^{+0.24}_{-0.16}$	$10.81^{+0.09}_{-0.29}$	$-10.51^{+0.69}_{-0.16}$	$8.59^{+3.55}_{-5.72}$
09cnd	SLSN-I	0.2583	5.99/6	$0.14^{+0.14}_{-0.10}$	$-16.43^{+0.47}_{-0.30}$	$-17.28^{+0.10}_{-0.07}$	$-17.13^{+0.39}_{-0.49}$	$-0.46^{+0.59}_{-0.36}$	$7.91^{+0.37}_{-0.62}$	$-8.33^{+0.99}_{-0.63}$	$0.49^{+1.77}_{-0.45}$
09ct	SN IIn	0.1560	5.98/12	$0.22^{+0.11}_{-0.10}$	$-17.06^{+0.82}_{-0.37}$	$-19.39^{+0.08}_{-0.05}$	$-20.85^{+0.26}_{-0.11}$	$0.11^{+0.29}_{-0.27}$	$9.92^{+0.13}_{-0.28}$	$-9.81^{+0.66}_{-0.32}$	$5.34^{+5.04}_{-4.00}$
09cu	SN II	0.0569	16.71/15	$0.23^{+0.24}_{-0.06}$	$-18.29^{+0.70}_{-0.11}$	$-20.74^{+0.23}_{-0.04}$	$-21.87^{+0.08}_{-0.24}$	$0.52^{+0.77}_{-0.24}$	$10.54^{+0.10}_{-0.54}$	$-10.01^{+1.43}_{-0.28}$	$7.70^{+4.13}_{-6.96}$
09cvi	SN II	0.0360	7.46/4	$0.76^{+0.20}_{-0.24}$	$-9.64^{+1.33}_{-1.38}$	$-13.85^{+0.18}_{-0.17}$	$-16.19^{+0.41}_{-0.58}$	$-0.31^{+0.59}_{-0.66}$	$6.94^{+0.40}_{-0.23}$	$-7.21^{+0.62}_{-0.96}$	$0.04^{+0.32}_{-0.03}$
09cwl	SLSN-I	0.3500	4.18/7	$0.38^{+0.08}_{-0.14}$	$-13.00^{+0.65}_{-0.69}$	$-14.96^{+0.19}_{-0.18}$	$-15.79^{+0.35}_{-0.22}$	$-0.55^{+0.46}_{-0.63}$	$6.78^{+0.69}_{-0.40}$	$-7.36^{+0.88}_{-1.19}$	$0.05^{+0.77}_{-0.04}$
09dah	SN IIb	0.0238	55.67/17	$0.08^{+0.06}_{-0.02}$	$-16.30^{+0.30}_{-0.11}$	$-17.84^{+0.17}_{-0.04}$	-18.17 ± 0.09	$-0.88^{+0.23}_{-0.10}$	$9.01^{+0.11}_{-0.32}$	$-9.89^{+0.64}_{-0.14}$	$6.80^{+4.44}_{-4.89}$
09dfk	SN Ib	0.0158	31.60/14	$0.19^{+0.05}_{-0.03}$	$-14.46^{+0.46}_{-0.24}$	$-16.78^{+0.10}_{-0.04}$	$-17.57^{+0.07}_{-0.06}$	$-1.21^{+0.19}_{-0.18}$	$8.76^{+0.12}_{-0.20}$	$-9.99^{+0.45}_{-0.17}$	$4.28^{+4.54}_{-2.76}$
09dh	SN Ic	0.0770	1.67/3	$0.54^{+0.39}_{-0.31}$	$-9.77^{+2.49}_{-1.61}$	$-12.88^{+0.52}_{-0.25}$	$-14.57^{+1.40}_{-1.39}$	$-1.15^{+1.10}_{-0.92}$	6.54 ± 0.73	$-7.58^{+1.20}_{-1.29}$	$0.09^{+1.40}_{-0.08}$
09dra	SN II	0.0766	16.39/17	$0.21^{+0.05}_{-0.04}$	$-18.55^{+0.23}_{-0.13}$	$-20.83^{+0.12}_{-0.04}$	$-21.83^{+0.08}_{-0.10}$	$0.55^{+0.18}_{-0.12}$	$10.43^{+0.14}_{-0.27}$	$-9.89^{+0.58}_{-0.17}$	$5.38^{+4.75}_{-3.73}$

Note. The absolute magnitudes are not corrected for host reddening. The SFRs are corrected for host reddening. The abbreviation “n.o.f.” stands for a number of filters. The “age” in the last column refers to the age of the stellar population. For details of the SED modeling, see Section 3.5. We omitted modeling the SED of PTF09bce’s host because the host galaxy is severely blended with another galaxy and deblending them is impossible.

(This table is available in its entirety in machine-readable form.)

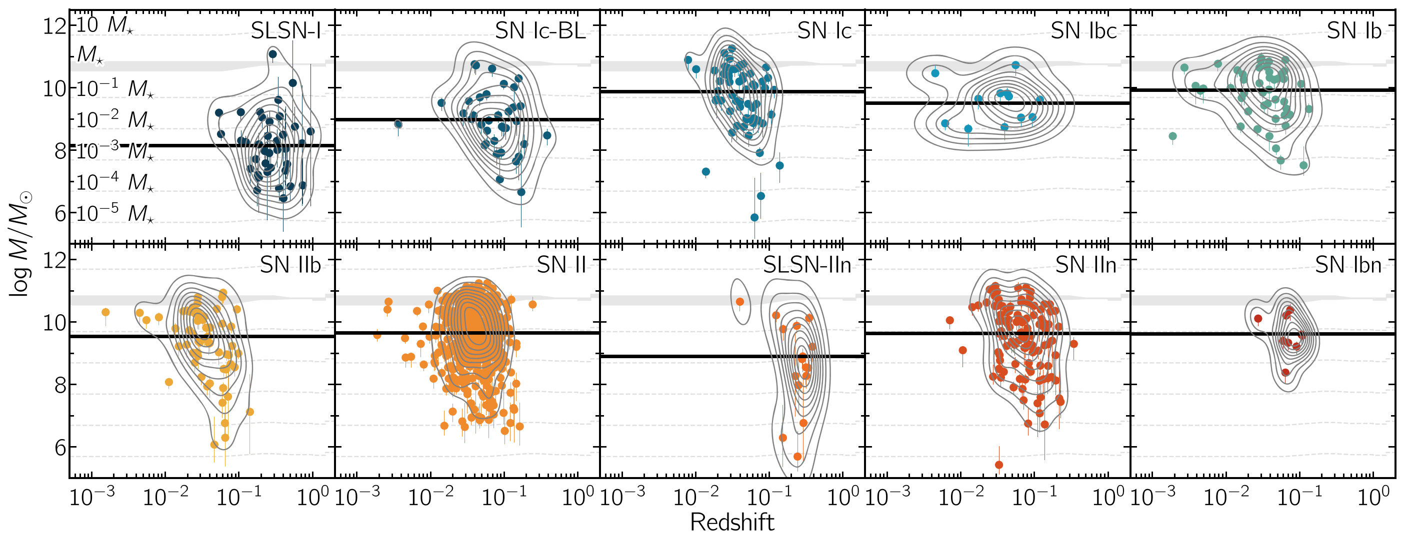

Figure 9. Host-galaxy mass vs. redshift. We overlay the characteristic mass $M_\star$ of the mass function from the GAMA (Baldry et al. 2012) and UltraVISTA (Muzzin et al. 2013) surveys in gray, as well as several mass tracks. To guide the eye, contours from 10% to 90% are overlaid on the data. The thick horizontal black line displays the median value of each sample. Note the difference of a factor of 5–25 between the masses of SLSNe and SNe Ib/c/II/IIb hosts.

fainter than −11 mag. This regime is comparable to the least-luminous star-forming galaxies in the Local Group (Mateo 1998; McConnachie 2012).

4.5. Stellar Masses

SED modeling gives access to the physical properties of the host galaxies. The primary properties we are interested in are the galaxy mass of the stellar component and the SFR. These measurements are summarized in Table 4.

Figure 9 shows the host masses as a function of redshift and SN class. The entire sample spans a range from $10^{5.4}$ to $10^{11.3}\,M_\odot$ (Table 4), corresponding to 10^{-5} to $10\,M_\star$, where $M_\star$ is the knee of Schechter-type galaxy mass functions (e.g., Baldry et al. 2012; Muzzin et al. 2013). About 29% and 11% of the sample are found in galaxies that are less massive than $10^9\,M_\odot$ and the $10^8\,M_\odot$[84], respectively. These values are consistent with those of Taggart & Perley (2021), who studied a more unbiased but significantly smaller SN sample. However, not all SN classes probe this parameter space in the same way. On average, H-poor and H-rich SLSNe and SNe Ic-BL have the least-massive galaxy populations. Their hosts are a factor of 5 – 25 less massive than the hosts of any other CCSN class (Table 5). Moreover, these samples exhibit a clear dearth of galaxies above $10^{10}\,M_\odot$ (Figure 9).

To examine these results further, we compare the median mass of a general population of star-forming galaxies to each SN sample. The CANDELS (Grogin et al. 2011; Koekemoer et al. 2011) and COSMOS (Scoville et al. 2007) surveys are the deepest galaxy surveys probing a sufficiently large cosmic volume and have a high level of completeness down to $10^8\,M_\odot$ at $z < 0.5$. This is still two to three orders of magnitude larger than the least-massive host in our sample. However, mass functions at $z < 0.5$ are well constrained and show no signs of plummeting at the low-mass end. We assume that the mass-function parameters are also valid for the range spanned by our host galaxies.

Under the working assumption that massive stars are the progenitors of all CCSN classes, we expect that their stellar mass functions should sample the mass function of star-forming galaxies weighted by their SFR. Using the mass-function parameterization from Tomczak et al. (2014) and the parameterization of the fundamental correlation between the galaxy stellar mass and SFR from Lee et al. (2015), we estimate that the SFR-weighted average galaxy mass in the mass interval probed by each of the SN samples is between $10^{9.5}\,M_\odot$ and $10^{9.9}\,M_\odot$.

These values match well the median host masses of most CCSN classes. Only the hosts of H-poor and H-rich SLSNe and Type Ic-BL SNe show a dearth of massive hosts compared to this model. Their median masses are $\log M/M_\odot \approx 8.15$ (SLSNe-I) and ∼8.9 (SNe Ic-BL and SLSN-IIn; Table 5), but the expected SFR-weighted average galaxy mass would be $10^{9.5}\,M_\odot$. The dearth of massive hosts is consistent with results reported by Perley et al. (2016), Chen et al. (2017a), Schulze et al. (2018), and Modjaz et al. (2020). In Section 5.2 we discuss this further.

Recently, Modjaz et al. (2020) studied a subsample of Type Ic and Ic-BL SNe and their host galaxies from the PTF survey. The median host mass of their SN Ic-BL sample is consistent with that of the entire PTF sample. However, the hosts of their SN Ic sample have masses that are 0.5 dex larger.

4.6. Star Formation Rates

To put the mass measurements in the context of star-forming galaxies, we present in Figure 10 the galaxy mass as a function of SN type. The vast majority of hosts occupy a narrow region of the SFR–$M_\star$ parameter space, with sSFR from 10^{-10} to 10^{-9} yr^{-1}. That part of the parameter space is also known as the locus of the galaxy main sequence of star-forming galaxies (thick dashed line in Figure 10), indicating that most SN host galaxies are normal star-forming galaxies. SLSNe are found in more vigorously star-forming galaxies with average values of $\sim 10^{-8.3}\,\mathrm{yr}^{-1}$, consistent with results reported by Perley et al. (2016), Schulze et al. (2018), and Taggart & Perley (2021). This places them in the regime of starbursting galaxies

---

[84] The masses of the SMC and the LMC are $10^{8.7}\,M_\odot$ and $10^{9.2}\,M_\odot$, respectively (McConnachie 2012).

Table 5

Statistical Properties of the SN Host-galaxy Samples

SN Class		log z	log Offset (kpc)	m_r (mag)	M_B (mag)	log M ($M_\odot$)	log SFR ($M_\odot$ yr^{-1})	log sSFR (yr^{-1})	log Age (yr)	$E_{\rm host}(B-V)$ (mag)
H-poor SNe										
SLSN-I	Median	$-0.570^{+0.045}_{-0.045}$	$0.283^{+0.068}_{-0.073}$	$22.90^{+0.33}_{-0.35}$	$-17.51^{+0.30}_{-0.28}$	$8.15^{+0.23}_{-0.24}$	$-0.23^{+0.16}_{-0.15}$	$-8.34^{+0.30}_{-0.32}$	$8.63^{+0.24}_{-0.27}$	$0.31^{+0.05}_{-0.04}$
	Mode	$-0.557^{+0.060}_{-0.055}$	$0.313^{+0.090}_{-0.105}$	$23.14^{+0.53}_{-0.84}$	$-17.63^{+0.33}_{-0.33}$	$8.20^{+0.43}_{-0.50}$	$-0.32^{+0.17}_{-0.14}$	$-8.33^{+0.69}_{-0.99}$	$9.05^{+0.49}_{-0.81}$	$0.15^{+0.03}_{-0.03}$ (37)
		(37)	(34)	(35)	(37)	(37)	(37)	(37)	(37)	
	FWHM	$0.680^{+0.114}_{-0.106}$	$0.827^{+0.228}_{-0.181}$	$4.89^{+1.73}_{-1.73}$	$4.34^{+0.83}_{-0.70}$	$2.58^{+0.60}_{-0.52}$	$1.97^{+0.48}_{-0.38}$	$2.36^{+0.61}_{-0.58}$	$2.21^{+0.49}_{-0.49}$	$0.70^{+0.46}_{-0.22}$
SNIc-BL	Median	$-1.112^{+0.052}_{-0.054}$	$0.479^{+0.062}_{-0.057}$	$19.03^{+0.44}_{-0.46}$	$-18.34^{+0.29}_{-0.29}$	$8.98^{+0.16}_{-0.16}$	$-0.33^{+0.15}_{-0.16}$	$-9.46^{+0.14}_{-0.13}$	$9.51^{+0.11}_{-0.13}$	$0.23^{+0.02}_{-0.01}$
	Mode	$-1.077^{+0.080}_{-0.095}$	$0.398^{+0.080}_{-0.055}$	$19.27^{+0.38}_{-0.46}$	$-18.33^{+0.38}_{-0.39}$	$8.95^{+0.21}_{-0.21}$	$-0.13^{+0.26}_{-0.49}$	$-9.57^{+0.18}_{-0.16}$	$9.78^{+0.14}_{-0.32}$	$0.14^{+0.02}_{-0.01}$ (36)
		(36)	(35)	(36)	(36)	(36)	(36)	(36)	(36)	
	FWHM	$0.725^{+0.129}_{-0.115}$	$0.779^{+0.134}_{-0.134}$	$6.02^{+1.18}_{-1.17}$	$4.62^{+0.60}_{-0.61}$	$2.23^{+0.42}_{-0.39}$	$1.48^{+0.29}_{-0.30}$	$1.65^{+0.46}_{-0.36}$	$1.12^{+0.32}_{-0.26}$	$0.38^{+0.06}_{-0.04}$
SN Ic	Median	$-1.389^{+0.033}_{-0.032}$	$0.540^{+0.059}_{-0.066}$	$16.36^{+0.39}_{-0.38}$	$-19.49^{+0.22}_{-0.21}$	$9.88^{+0.14}_{-0.14}$	$0.02^{+0.11}_{-0.12}$	$-9.79^{+0.07}_{-0.07}$	$9.50^{+0.04}_{-0.05}$	$0.25^{+0.01}_{-0.01}$
	Mode	$-1.382^{+0.045}_{-0.045}$	$0.694^{+0.065}_{-0.080}$	$15.88^{+1.42}_{-0.77}$	$-19.76^{+0.23}_{-0.21}$	$10.30^{+0.15}_{-0.35}$	$0.23^{+0.11}_{-0.14}$	$-9.81^{+0.06}_{-0.06}$	$9.75^{+0.05}_{-0.06}$	$0.17^{+0.02}_{-0.01}$ (60)
		(60)	(58)	(60)	(60)	(60)	(60)	(60)	(60)	
	FWHM	$0.648^{+0.075}_{-0.073}$	$0.957^{+0.134}_{-0.132}$	$5.90^{+0.81}_{-0.76}$	$4.96^{+0.52}_{-0.50}$	$2.01^{+0.30}_{-0.27}$	$1.87^{+0.32}_{-0.29}$	$1.57^{+0.19}_{-0.16}$	$1.16^{+0.12}_{-0.10}$	$0.39^{+0.04}_{-0.03}$
SN Ibc	Median	$-1.436^{+0.105}_{-0.153}$	$0.382^{+0.142}_{-0.199}$	$16.43^{+0.71}_{-0.65}$	$-19.00^{+0.51}_{-0.43}$	$9.51^{+0.21}_{-0.22}$	$-0.27^{+0.16}_{-0.17}$	$-9.83^{+0.14}_{-0.17}$	$9.50^{+0.09}_{-0.10}$	$0.22^{+0.03}_{-0.02}$
	Mode	$-1.322^{+0.105}_{-0.080}$	$0.629^{+0.060}_{-0.495}$	$16.22^{+1.80}_{-0.77}$	$-19.38^{+1.07}_{-0.32}$	$9.51^{+0.26}_{-0.51}$	$-0.28^{+0.17}_{-0.18}$	$-9.75^{+0.13}_{-0.13}$	$9.73^{+0.13}_{-0.15}$	$0.14^{+0.03}_{-0.03}$ (12)
		(12)	(12)	(12)	(12)	(12)	(12)	(12)	(12)	
	FWHM	$0.999^{+0.276}_{-0.360}$	$1.041^{+0.298}_{-0.314}$	$5.03^{+2.53}_{-1.49}$	$3.58^{+0.97}_{-0.99}$	$1.57^{+0.43}_{-0.46}$	$1.26^{+0.60}_{-0.39}$	$1.28^{+0.70}_{-0.42}$	$1.12^{+0.18}_{-0.19}$	$0.35^{+0.06}_{-0.04}$
SN Ib	Median	$-1.469^{+0.048}_{-0.054}$	$0.483^{+0.079}_{-0.089}$	$15.54^{+0.43}_{-0.42}$	$-19.51^{+0.26}_{-0.25}$	$9.92^{+0.13}_{-0.15}$	$0.01^{+0.14}_{-0.15}$	$-9.89^{+0.07}_{-0.07}$	$9.13^{+0.04}_{-0.05}$	$0.25^{+0.01}_{-0.01}$
	Mode	$-1.377^{+0.045}_{-0.050}$	$0.644^{+0.085}_{-0.105}$	$15.47^{+0.67}_{-0.67}$	$-19.61^{+0.39}_{-0.89}$	$10.26^{+0.16}_{-0.22}$	$0.31^{+0.24}_{-0.49}$	$-9.90^{+0.07}_{-0.07}$	$9.71^{+0.06}_{-0.07}$	$0.19^{+0.02}_{-0.01}$ (46)
		(46)	(46)	(45)	(46)	(46)	(46)	(46)	(46)	
	FWHM	$0.859^{+0.208}_{-0.162}$	$1.363^{+0.191}_{-0.187}$	$6.30^{+1.01}_{-0.98}$	$3.47^{+0.62}_{-0.62}$	$1.92^{+0.32}_{-0.32}$	$1.82^{+0.29}_{-0.28}$	$1.19^{+0.20}_{-0.17}$	$1.83^{+0.12}_{-0.09}$	$0.38^{+0.03}_{-0.03}$
H-rich SNe										
SN IIb	Median	$-1.447^{+0.037}_{-0.037}$	$0.432^{+0.065}_{-0.079}$	$16.71^{+0.41}_{-0.37}$	$-18.78^{+0.25}_{-0.23}$	$9.53^{+0.15}_{-0.16}$	$-0.30^{+0.12}_{-0.12}$	$-9.80^{+0.07}_{-0.07}$	$9.35^{+0.05}_{-0.06}$	$0.26^{+0.02}_{-0.02}$
	Mode	$-1.437^{+0.060}_{-0.050}$	$0.609^{+0.045}_{-0.050}$	$15.98^{+0.36}_{-0.33}$	$-19.32^{+0.33}_{-0.27}$	$10.04^{+0.15}_{-0.42}$	$-0.18^{+0.25}_{-0.29}$	$-9.84^{+0.12}_{-0.11}$	$9.74^{+0.06}_{-0.06}$	$0.15^{+0.02}_{-0.02}$ (61)
		(61)	(60)	(61)	(61)	(61)	(61)	(61)	(61)	
	FWHM	$0.709^{+0.100}_{-0.090}$	$1.162^{+0.163}_{-0.165}$	$7.42^{+1.18}_{-1.13}$	$4.35^{+0.92}_{-0.72}$	$2.25^{+0.37}_{-0.35}$	$1.78^{+0.30}_{-0.27}$	$1.08^{+0.33}_{-0.23}$	$1.49^{+0.20}_{-0.15}$	$0.46^{+0.10}_{-0.06}$
SN II	Median	$-1.408^{+0.012}_{-0.012}$	$0.537^{+0.023}_{-0.024}$	$16.60^{+0.13}_{-0.13}$	$-19.15^{+0.09}_{-0.09}$	$9.65^{+0.05}_{-0.05}$	$-0.24^{+0.04}_{-0.04}$	$-9.86^{+0.02}_{-0.02}$	$9.61^{+0.02}_{-0.02}$	$0.14^{+0.01}_{-0.01}$
	Mode	$-1.392^{+0.015}_{-0.020}$	$0.679^{+0.035}_{-0.040}$	$16.77^{+0.58}_{-1.10}$	$-19.75^{+0.34}_{-0.24}$	$9.77^{+0.47}_{-0.15}$	$-0.12^{+0.08}_{-0.09}$	$-9.86^{+0.04}_{-0.04}$	$9.80^{+0.02}_{-0.02}$	$0.12^{+0.04}_{-0.03}$ (496)
		(498)	(496)	(492)	(496)	(496)	(496)	(496)	(496)	
	FWHM	$0.664^{+0.027}_{-0.026}$	$1.054^{+0.057}_{-0.056}$	$4.88^{+0.30}_{-0.30}$	$3.76^{+0.25}_{-0.23}$	$1.96^{+0.13}_{-0.13}$	$1.72^{+0.09}_{-0.09}$	$1.09^{+0.09}_{-0.08}$	$0.98^{+0.05}_{-0.04}$	$0.19^{+0.01}_{-0.01}$
Interaction-powered SNe										
SLSN- IIn	Median	$-0.616^{+0.039}_{-0.047}$	$0.343^{+0.136}_{-0.142}$	$22.26^{+0.69}_{-0.78}$	$-18.30^{+0.69}_{-0.62}$	$8.89^{+0.38}_{-0.37}$	$-0.15^{+0.22}_{-0.21}$	$-9.10^{+0.33}_{-0.25}$	$9.03^{+0.20}_{-0.28}$	$0.28^{+0.06}_{-0.04}$
	Mode	$-0.577^{+0.030}_{-0.035}$	$0.321^{+0.283}_{-0.168}$	$22.78^{+0.89}_{-1.03}$	$-19.13^{+1.07}_{-0.87}$	$8.91^{+1.14}_{-0.47}$	$-0.16^{+0.34}_{-0.22}$	$-9.33^{+0.41}_{-0.22}$	$9.44^{+0.24}_{-0.32}$	$0.16^{+0.04}_{-0.03}$ (16)
		(16)	(15)	(15)	(16)	(16)	(16)	(16)	(16)	
	FWHM	$0.559^{+0.157}_{-0.109}$	$1.027^{+0.464}_{-0.356}$	$6.17^{+2.20}_{-1.99}$	$5.79^{+1.46}_{-2.13}$	$2.90^{+1.25}_{-1.13}$	$1.68^{+0.81}_{-0.55}$	$2.19^{+1.10}_{-0.86}$	$1.97^{+0.80}_{-0.60}$	$0.54^{+0.52}_{-0.17}$
SN IIn	Median	$-1.161^{+0.030}_{-0.030}$	$0.555^{+0.040}_{-0.042}$	$17.92^{+0.27}_{-0.28}$	$-19.25^{+0.20}_{-0.18}$	$9.63^{+0.12}_{-0.12}$	$-0.09^{+0.07}_{-0.07}$	$-9.70^{+0.07}_{-0.07}$	$9.29^{+0.04}_{-0.05}$	$0.25^{+0.01}_{-0.01}$
	Mode	$-1.137^{+0.045}_{-0.055}$	$0.594^{+0.065}_{-0.070}$	$17.93^{+0.41}_{-1.27}$	$-19.85^{+0.24}_{-0.23}$	$10.05^{+0.17}_{-0.25}$	$0.01^{+0.11}_{-0.11}$	$-9.80^{+0.08}_{-0.07}$	$9.67^{+0.05}_{-0.05}$	$0.17^{+0.01}_{-0.01}$ (111)
		(111)	(110)	(109)	(111)	(111)	(111)	(111)	(111)	
	FWHM	$0.722^{+0.062}_{-0.062}$	$0.919^{+0.111}_{-0.103}$	$5.67^{+0.73}_{-0.71}$	$3.92^{+0.44}_{-0.45}$	$2.35^{+0.26}_{-0.26}$	$1.59^{+0.19}_{-0.18}$	$1.69^{+0.26}_{-0.23}$	$1.53^{+0.12}_{-0.11}$	$0.39^{+0.03}_{-0.02}$
SN Ibn	Median	$-1.146^{+0.046}_{-0.054}$	$0.525^{+0.244}_{-0.193}$	$18.14^{+0.59}_{-0.65}$	$-19.02^{+0.48}_{-0.47}$	$9.62^{+0.21}_{-0.20}$	$-0.32^{+0.27}_{-0.30}$	$-9.87^{+0.18}_{-0.18}$	$9.49^{+0.09}_{-0.10}$	$0.23^{+0.02}_{-0.02}$
	Mode	$-1.122^{+0.045}_{-0.040}$	$0.458^{+0.566}_{-0.190}$	$18.45^{+0.82}_{-1.03}$	$-19.13^{+0.75}_{-0.83}$	$9.59^{+0.43}_{-0.18}$	$-0.25^{+0.46}_{-0.57}$	$-9.87^{+0.19}_{-0.17}$	$9.68^{+0.15}_{-0.16}$	$0.16^{+0.03}_{-0.03}$ (9)
		(9)	(9)	(9)	(9)	(9)	(9)	(9)	(9)	
	FWHM	$0.524^{+0.142}_{-0.124}$	$1.085^{+0.388}_{-0.366}$	$4.28^{+1.20}_{-1.33}$	$3.22^{+0.81}_{-0.89}$	$1.39^{+0.53}_{-0.47}$	$1.55^{+0.52}_{-0.54}$	$1.22^{+0.65}_{-0.42}$	$1.11^{+0.17}_{-0.18}$	$0.35^{+0.04}_{-0.04}$

Note. The medians, modes, and the FWHMs as well as their uncertainties were extracted from the KDEs. The values in parentheses display the number of objects that were used. The r-band brightness and the B-band luminosity are not corrected for host attenuation. We omit reporting the statistics for SLSNe-II and SLSNe-IIb because these classes consist of only one object each.

(Daddi et al. 2007; Elbaz et al. 2007; Noeske et al. 2007; Sargent et al.2012).

Starbursts are not exclusive to SLSN hosts. The most vigorously star-forming host galaxies of regular CCSNe reach sSFR values of $>10^{-8}\,{\rm yr}^{-1}$ (e.g., iPTF15eqq—SNII, $>10^{-7}\,{\rm yr}^{-1}$; PTF12eci—SN Ic-BL, $>10^{-7.1}\,{\rm yr}^{-1}$; PTF09cvi—SN Ic-BL, $>10^{-7.2}\,{\rm yr}^{-1}$; Table 4). More quantitatively, ∼11% of all regular CCSNe are found in galaxies with sSFR $> 10^{-9}\,{\rm yr}^{-1}$ (just above the galaxy main sequence) and 3% are found in extreme starbursts with sSFR $> 10^{-8}\,{\rm yr}^{-1}$. The frequency of extreme starburst galaxies hosting regular CCSNe is consistent with the results of Taggart & Perley (2021). In stark contrast to the low starburst fraction of regular CCSNe, 68^{+11}_{-8}% and 38^{+11}_{-8}% of all H-poor SLSNe exploded in galaxies with sSFR $> 10^{-9}\,{\rm yr}^{-1}$ and $> 10^{-8}\,{\rm yr}^{-1}$, respectively.

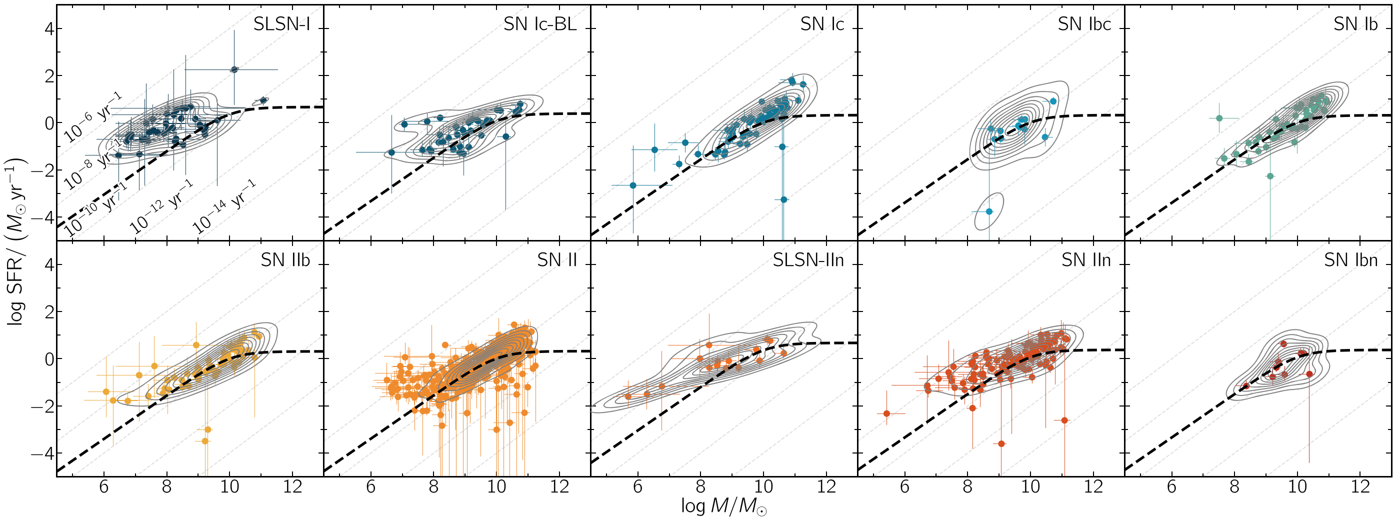

Figure 10. The host-galaxy populations in the mass–SFR plane. All SNe explode in galaxies whose SEDs are consistent with ongoing star formation. This is illustrated by their location with respect to the main sequence of star-forming galaxies (black dashed curve). The gray dotted diagonal lines display lines of constant specific star formation rate (SFR normalized by stellar mass). To guide the eye, contours from 10% to 90% are overlaid.

On the other extreme of the SFR spectrum, $\lesssim 2\%$ of the hosts of regular CCSNe (Ibc, IIb, II, and IIn) have SFR $\lesssim 0.01\, M_\odot\, \mathrm{yr}^{-1}$ and sSFR between $10^{-14}\, \mathrm{yr}^{-1}$ and $10^{-11}\, \mathrm{yr}^{-1}$, albeit with very large uncertainties. Whether these galaxies are barely star-forming or perhaps not star-forming at all requires additional data, such as far-infrared measurements to assess dust-obscured star formation and integral-field spectroscopy to search for star-forming regions at SN sites. The binary evolution of massive stars could provide an additional explanation for this result. Sana et al. (2012) concluded that binary evolution of massive stars produces a merger in a third of the cases. This could result in new SN channels (Zapartas et al. 2017) where two intermediate-mass stars, which cannot explode as CCSNe alone, merge and then explode as a CCSN. Such progenitor systems have much longer lifetimes and could therefore be found in galaxies with little-to-no star formation. This scenario was discussed for the SN II iPTF16hil that exploded in the outskirts of an elliptical galaxy (Irani et al. 2019).

4.7. Projected Distances between SNe and Hosts

The projected distances (summarized in Table 3) between SNe and the center of their host galaxies extend from 0.02 ± 0.20 kpc (PTF09awk, Type II; Figure 6) to 37.00 ± 0.05 kpc (iPTF13ebs; Type IIb)[85,86]. At the same time, the masses of the host galaxies vary from 10^5 to $10^{11.5}\, M_\odot$ and therefore the sizes of the host galaxies are expected to vary considerably.

To better understand this behavior and whether certain SN classes are found in peculiar host locations, we present the offsets as a function of host-galaxy mass and SN type in Figure 11. We also overlay the relation between the 80%-light radius (r_{80}) and galaxy mass, which is thought to trace the stellar mass content of galaxies independently of whether they are star-forming (Miller et al. 2019; Mowla et al. 2019). The overwhelming majority of CCSNe are found within r_{80}. Fewer than 15% of each SN class are found at distances larger than r_{80}. After propagating uncertainties, the fraction of SNe at large distances decreases to $< 8\%$ (3σ confidence level). Either way, this percentage of SNe with large offsets is expected because we compare their distance to the 80%-light radius. This result reassures us that we reliably identified the host galaxies of most CCSNe in our sample.

5. Discussion

5.1. Distribution Functions

In the previous sections, we focused on a general description of the host-galaxy population. Here, we construct and examine the distribution functions. The observed distribution functions suffer from the combined effect of the measurement errors and selection bias. Taking selection effects into account requires detailed knowledge of how the survey was operated, how transients were identified, how objects were selected for classification, and how successful were these classification efforts (e.g., Frohmaier et al. 2017; Feindt et al. 2019) —issues beyond the scope of this paper. To account for measurement errors, we perform a Monte Carlo simulation (30,000 samples per host property and SN class) and bootstrap each sample. In the Monte Carlo simulation, each data point is resampled as follows.

1. Redshifts have very small statistical and systematic errors, which are assumed to be negligible.
2. SN-host offsets are represented by the Rice distribution because the offsets are never negative and Gaussian noise superimposed on a vector results in a non-Gaussian probability distribution (Rice 1945).
3. The r'-band magnitudes are represented by a normal distribution. In the case of a nondetection, a measurement is represented by a uniform distribution where the bright and faint bounds are set to the 3σ limiting magnitude and the faintest host in the sample (dimmed by an additional 0.5 mag), respectively.

---

[85] In addition to PTF09bce, PTF12mja, and the 10 "hostless" SNe, we removed two more hosts in the host-offset analysis. The host of PTF10hfe is a ring galaxy without a center (Figure 6). PTF11aun exploded in a dwarf galaxy; however, the host is severely blended with a foreground star, and the galaxy center cannot be reliably measured.

[86] The offset measurements of PTF10cd and iPTF17bsi are based on the SN coordinates on the PTF Marshal owing to an absence of publicly available SN images.

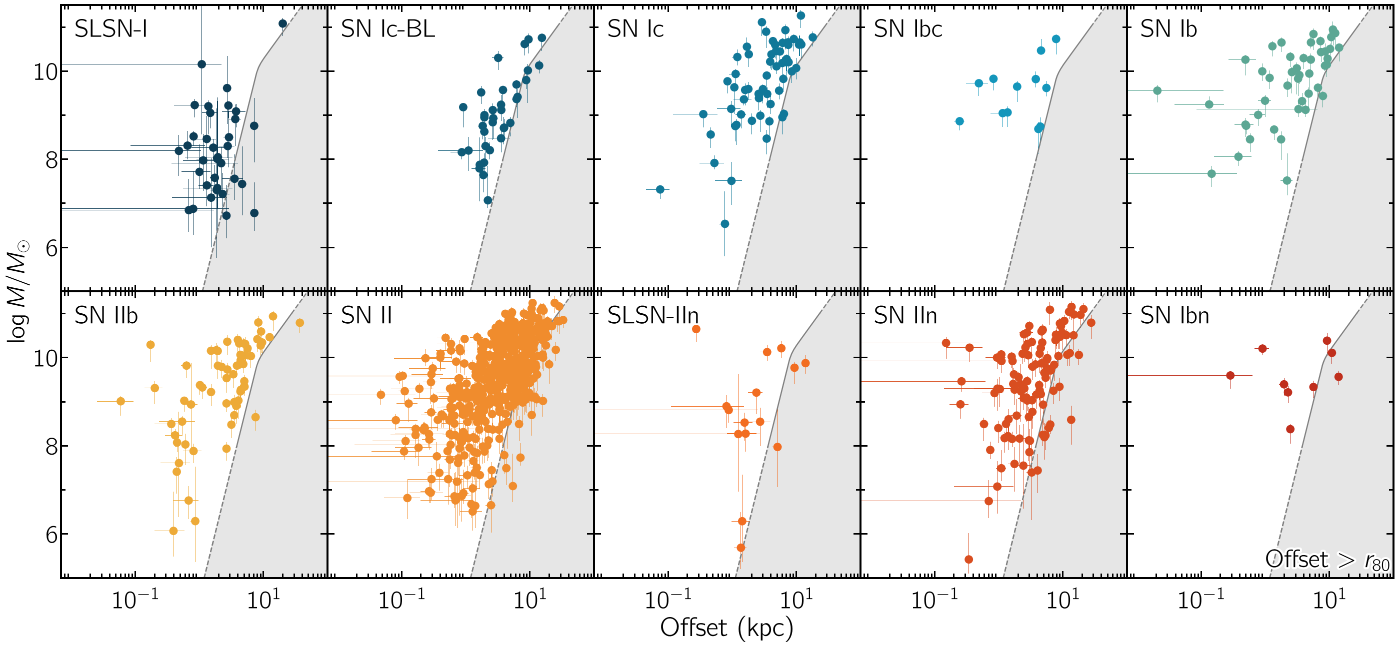

Figure 11. Galaxy mass versus supernova-host offset. Most SNe are located within the 80%-light radius of their host galaxies. Up to 15% of each SN class are found at larger galactocentric distances. This is expected because the offsets are compared to the curves of 80% light.

4. For the age of the stellar population, attenuation, galaxy mass, M_B, SFR, and sSFR, we use the marginalized posteriors from the SED modeling.

We estimate the probability distribution functions using kernel density estimate (KDE) techniques. The critical parameter of the KDEs is the bandwidth —that is, the smoothing parameter. For each sample, we estimate an adequate value using the leave-one-out cross-correlation method. For samples with fewer than 20 objects (e.g., SNe Ibn and SLSNe-IIn), we set the bandwidth parameter to the median value of the other host samples. To compute the pointwise 1σ confidence intervals, we compute the 68% confidence interval around the median KDE of each distribution function.

Figure 12 shows the KDEs and the pointwise 1σ confidence intervals of all host properties. Table 5 summarizes the median, mode, and FWHM of each KDE. The distribution functions can exhibit complex shapes; they are unimodal, but they can display asymmetries and pronounced wings primarily toward the faint end, independent of sample size and SN/host property. The asymmetries and the wings reflect, in part, the intrinsic shape of the luminosity and mass functions. Moreover, the existence of pronounced tails in the KDEs limits the effectiveness of median values and widths to identify hosts with outstanding properties. As an auxiliary data product of this paper, we release tabulated versions of KDEs to identify singular hosts more easily.

We remark that the multiple peaks seen in the distribution functions are most likely artifacts due to the small sample sizes. As a sanity check, we generated fake samples from symmetric and asymmetric unimodal distributions, where we vary the sample sizes between 30 and 500. Multiple peaks and shoulders are generally observed in the distribution functions with $\lesssim 100$ objects, causing deviations from the actual underlying distributions.

5.2. *Environmental Effects on the Formation of CCSNe*

5.2.1. *Metallicity-dependent SN Production Efficiency*

In Section 4.5, we found a dearth of galaxies above $10^{10}\,M_\odot$ hosting SLSNe-I/IIn and SNe Ic-BL, while other CCSN classes seem to select galaxies solely based on their star formation activity. This could point to an environment-dependent production efficiency of progenitor systems of some CCSN classes, as demonstrated by Perley et al. (2016) and Schulze et al. (2018). The primary parameter that could regulate the production efficiency is the galaxy mass because it is known to correlate well with the average galaxy metallicity (e.g., Tremonti et al. 2004; Mannucci et al. 2010; Andrews & Martini 2013). Metallicity, in turn, has a strong effect on the evolution of massive stars through line-driven stellar winds (e.g., Kudritzki & Puls 2000).

To quantify the metallicity-dependent production efficiencies, we apply the method from Schulze et al. (2018) that we also applied in Section 4.5, as follows. We start with the stellar mass function $\Phi(M)$ of star-forming galaxies from CANDELS and use the parameterization of the mass function for galaxies of Tomczak et al. (2014, their Table 2). This yields the number density of galaxies per stellar mass bin. Next, we weigh each mass bin by its contribution to the cosmic star formation at a given redshift using the fundamental relationship between galaxy mass and SFR and the parameterization of Lee et al. (2015), which is valid from $10^{8.5}$ to $10^{11.25}\,M_\odot$. The functional form of the SFR-weighted mass function is $w\{\mathrm{SFR}(M)\} \times \Phi\{M\}$, where w is the SFR weight.

To find the best-fitting model, we generate 30,000 samples of the observed data of each SN class as described in Section 5.1. Within each trial, we also vary the galaxy mass function parameters within their uncertainties and the location of the bin centers and find the best-fitting model parameters using least-squares fitting. In the final step, we build distribution functions of the model parameters and extract the median value and its uncertainties for each parameter.

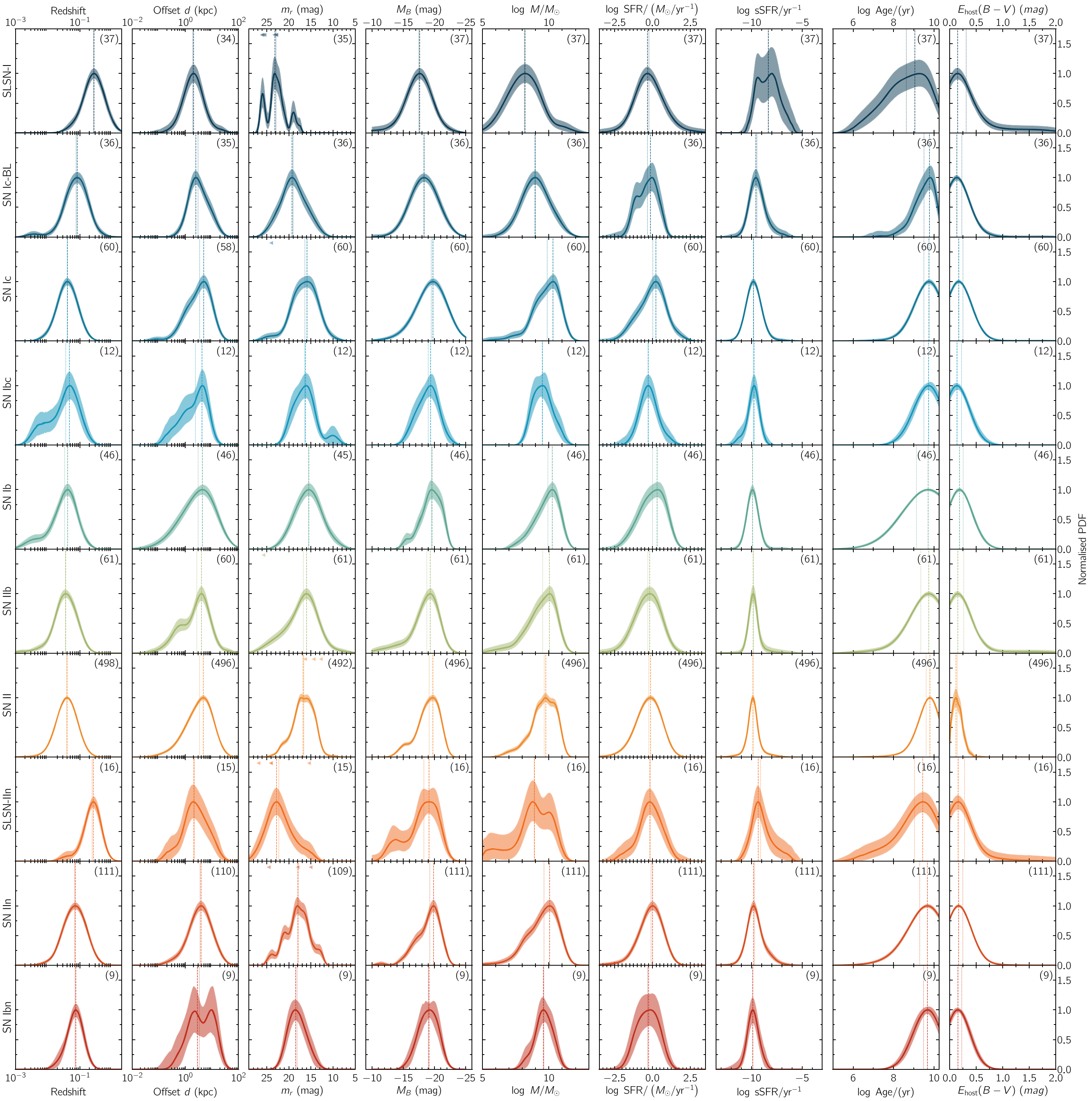

Figure 12. Kernel density estimates (KDE) of SN and host properties. The shaded regions display the pointwise 1σ confidence intervals. The vertical dashed and dotted lines indicate the mode and the median, respectively. The numbers in parentheses quote the sample sizes. To guide the eye, the KDEs are normalized to have the same peak height. Upper limits in the r-band brightness are indicated by left-pointing triangles in the upper half of a panel.

Figure 13 shows the observed mass distributions of the eight largest SN classes and in gray the best-fit SFR-weighted mass functions. The predicted mass functions provide excellent matches to the samples of hosts of SNe Ibc[87], SNe II/IIb SNe, and SNe IIn. This means that their occurrence is independent of global galaxy metallicity to the level we are sensitive and driven by the star formation activity of their hosts.

In contrast to the agreement between the observed mass distributions and the SFR-weighted mass functions for the hosts of SNe Ib, Ic, Ibc + Ib + Ic, II, IIb, and IIn, the mass distributions of SLSN and SN Ic-BL host galaxies peak one to two orders of magnitudes lower than predicted by the SFR-weighted mass functions. To account for the relative lack of massive galaxies, we introduce a function that describes an efficiency $\rho(M)$ of producing SNe from star formation. Similar to Schulze et al. (2018), we chose $\rho(M)$ as an exponential function of the form $\rho(M) = \exp(-M/M_0)$, where M_0 is a

---

[87] In this analysis and in Section 5.2.2, we combined SNe Ib, Ic, and Ibc to maximize the sample size.

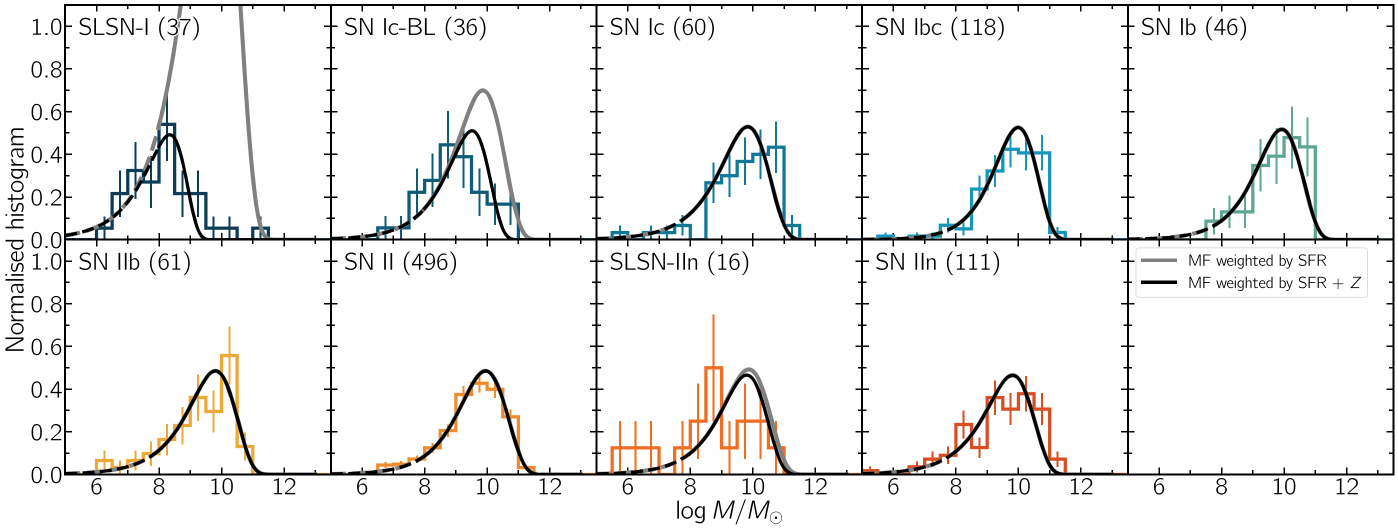

Figure 13. Host-mass distributions of each CCSN class. The SFR-weighted mass-function model (gray curves) provides an adequate description of the mass distributions of SN Ib/c, IIb, II, and IIn host galaxies. The observed mass distributions of SLSN-I and SN Ic-BL hosts show a clear dearth of massive host galaxies. This absence can be accounted for by adding a metallicity-dependent SN production efficiency (black curves). The production efficiencies of SLSNe-I and SNe Ic-BL are stifled in environments with oxygen abundances exceeding $8.26^{+0.22}_{-0.30}$ and $8.66^{+0.20}_{-0.14}$, respectively. The sample of SLSN-IIn hosts is too small to conclude whether SLSNe-IIn require particular environments. The host sample of SNe Ibc includes the Type Ib, Ic, and Ibc SNe, to maximize the sample size. We remark that the galaxy mass functions were extrapolated for masses $<10^8\,M_\odot$. This is indicated by the dashed lines. Note, the gray and the black curves differ only for the host-galaxy samples of SLSNe and SNe Ic-BL.

Table 6
Summary of the Cutoff Mass and Metallicities of the Metallicity-dependent SN Production Efficiencies

SN class	$\log M_0/M_\odot$	$12 + \log \mathrm{O/H}$	χ^2/d.o.f.
SLSN-I	$8.64^{+0.46}_{-0.64}$	$8.26^{+0.26}_{-0.30}$	4.6/9
SN Ic-BL	$9.47^{+0.42}_{-0.30}$	$8.65^{+0.20}_{-0.14}$	2.0/8
SLSN-IIn	$9.67^{+1.56}_{-0.87}$	$8.75^{+0.33}_{-0.41}$	1.9/7

Note. The abbreviation "d.o.f." stands for the degree of freedom.

characteristic cutoff mass and therefore a cutoff metallicity. The functional form of the metallicity-dependent SFR-weighted mass function is $\rho\{M\} \times w\{\mathrm{SFR}(M)\} \times \Phi\{M\}$.

The best fits are shown by the black curves in Figure 13, and fit parameters are summarized in Table 6. This model adequately describes the observed mass distributions of SLSN-I, SN Ic-BL, and SLSN-IIn host galaxies, albeit the sample size of the SLSN-IIn class is too small to draw a firm conclusion. We convert these mass cutoffs into a cutoff oxygen abundance using Equation (5) of Mannucci et al. (2010). The best-fitting models point to stifled production efficiencies at oxygen abundances exceeding $12 + \log \mathrm{O/H} = 8.26^{+0.26}_{-0.30}$, $8.65^{+0.20}_{-0.14}$, and $8.75^{+0.33}_{-0.41}$ for SLSNe-I, SNe Ic-BL, and SLSNe-IIn, respectively. This translates to cutoff metallicities of ~0.4, ~1, and ~1.1 solar metallicity for SLSNe-I, SNe Ic-BL, SLSNe-IIn (respectively), using the solar oxygen abundance reported by Asplund et al. (2009).

The value of H-poor SLSNe is consistent with those reported by Perley et al. (2016), Chen et al. (2017a), and Schulze et al. (2018). Furthermore, the hosts of H-poor SLSNe are characterized by the youngest stellar population. Their median age is $\log(\mathrm{Age/yr}) \approx 8.6$, in contrast to the average age of $\log(\mathrm{Age/yr}) \approx 9.7$ of all regular CCSN host galaxies (Table 5). Measuring ages is notoriously difficult. However, as we demonstrated in Section 3.5.3, the inferred ages are reliable in a comparative sense—samples of young galaxies remain young and samples of evolved galaxies remain old independent of the wavelength coverage of the SEDs or the assumptions of the SED model. This means that the difference in the age distributions reflects a genuine difference. Therefore, not only low metallicity but also young age play important roles in the formation of SLSN-I progenitors. This corroborates the conjecture by Leloudas et al. (2015), Thöne et al. (2015), and Schulze et al. (2018) that SLSNe could be connected with the death of very massive stars (see also Taggart & Perley 2021).

Our result for SNe Ic-BL is consistent with that of Modjaz et al. (2020). These authors analyzed a subsample of the entire PTF SN Ic-BL sample and reported a median oxygen abundance of $12 + \log \mathrm{O/H} \approx 8.5$. The median mass of the entire SN Ic-BL host sample is $\log M/M_\odot \approx 8.98$ (Table 5). This value translates to a median oxygen abundance of ~8.4 using Equation (5) of Mannucci et al. (2010). Our analysis expands upon that of Modjaz et al. (2020) by providing a critical galaxy metallicity ($0.9^{+0.5}_{-0.3}$ solar) above which the production is stifled.

Long-duration gamma-ray bursts (GRBs) are thought to be accompanied by SNe Ic-BL (for a recent review, see Cano et al. 2017, but see Fynbo et al. 2006; Greiner et al. 2015; Michałowski et al. 2018; Tanga et al. 2018; Kann et al. 2019). An outstanding question in the SN and GRB fields is how both subpopulations of SNe Ic-BL are connected (e.g., Modjaz et al. 2020). GRBs also show a pronounced environmental dependence. At $z < 1$, their production efficiency is stifled above 0.5–0.9 solar metallicity (Krühler et al. 2015; Schulze et al. 2015; Vergani et al. 2015; Perley et al. 2016; Vergani et al. 2017; Schulze et al. 2018), consistent with our measurement of SNe Ic-BL. However, the comparison is limited by the large statistical errors.

The sample of SLSNe-IIn is too small to draw a firm conclusion on any environment-dependent production efficiency, similar to SNe Ibn, which are even rarer in the PTF sample.

5.2.2. Differences between SNe Ibc and SNe II/IIb

To identify more subtle differences in the SN environments, we directly compare the mass, SFR, and sSFR distribution functions. Critical for this analysis is that the redshift

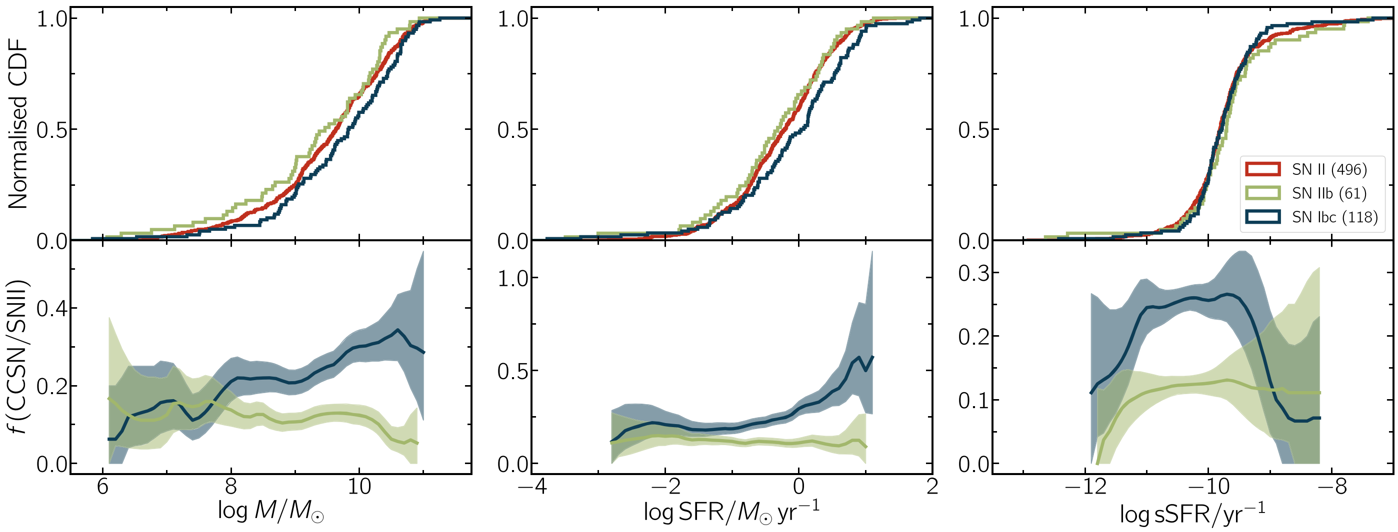

Figure 14. Comparison of the distribution functions (top) and number ratios between Type Ibc, IIb, and II SNe (bottom) as a function of different galaxy properties. SNe Ibc are found in significantly more massive galaxies with higher absolute SFRs (but similar values of sSFR) than SNe II and SNe IIb. In contrast to that, SNe IIb explode in galaxies very similar to those of SNe II. The shaded regions indicate the 1σ confidence interval of the number ratio (see main text for details). The ratios do not extend to the ends of the distribution because of low number statistics.

distributions are statistically identical to minimize the impact of the secular evolution of SN and host properties. This limits the comparison to SNe Ibc, IIb, and II.

The top panels of Figure 14 show the cumulative distribution functions of the galaxy mass, the SFR, and the sSFR of the three samples, in all cases spanning the same range. To quantify dissimilarities between the SN classes, we apply the Anderson–Darling test on 30,000 resampled distributions for each SN class and host property (generated as described in Section 5.1). Our null hypothesis is that the test sample is drawn from the parent sample. We reject the null hypothesis if the chance probability $p_{\rm ch}$ is smaller than 5%.

The mass, SFR, and sSFR distribution functions of SN IIb and SN II host galaxies are statistically identical. The chance probabilities to randomly draw a mass, SFR, or sSFR distribution from the SN II host sample, which are as extreme as the SN IIb host sample, are between 12% and 24% (Table 7). Similarly, the mass, the SFR, and the sSFR distributions of SN Ib and SN Ic hosts are statistically identical ($p_{\rm ch} = 19$–35%; Table 7).

As the SN Ib and SN Ic host populations are shown to be similar, we combine the SN Ib, Ibc, and Ic samples. This gives us the larger statistical power to trace differences between the host populations of SNe Ibc and SNe II, and of SNe Ibc and SNe IIb. Indeed, there are statistically significant differences between the mass and SFR distributions of SN Ibc and SN IIb as well as SN II hosts. The chance probabilities vary between 0.4% and 4%, which are below our threshold of rejecting the null hypothesis (Table 7).

To illustrate these results differently, we present in the bottom panels of Figure 14 the number ratios between Type Ibc and Type II SNe (blue) and Type IIb and II SNe (green) as a function of galaxy mass, SFR, and sSFR. We computed this ratio for moving bins (bin width 1 dex and bin step size 0.1 dex) for each resampled distribution, and then extracted the median ratio and its 1σ confidence interval at each bin step. SNe Ibc are found in more massive galaxies with higher absolute SFR but the same sSFR as SNe II. In contrast to that, the number ratio between SNe IIb and SNe II does not change with host properties.

In summary, any difference in the production efficiencies of regular CCSNe is only mildly dependent on global galaxy properties. Understanding the mapping between SNe and their progenitors may require examining the particular conditions of the explosion sites across the full spectrum of host-galaxy properties (e.g., colors, metallicities, SFR densities, and ages of the stellar populations; Modjaz et al. 2008; Leloudas et al. 2011; Kelly & Kirshner 2012; Sanders et al. 2012; Kuncarayakti et al. 2013a; Kelly et al. 2014).

Previously, Arcavi et al. (2010) reported the CCSN number ratio based on PTF Year-1 data, which included 72 CCSNe of various types. They concluded that SNe Ic are almost exclusively found in galaxies brighter than $M_r < -19$ mag. In less-luminous galaxies, the stripped-envelope SN population is dominated by SNe Ib and SNe Ic-BL. Furthermore, these authors found an excess of SNe IIb in low-luminosity galaxies. To explain their results, Arcavi et al. (2010) hypothesized that metallicity-driven mass loss leads to reduced stripping of SN Ic progenitors in low-metallicity environments, which allows their progenitors to retain some hydrogen and helium.

Using the full PTF sample, we cannot recover several of these suggested trends. Type II, IIb, Ib, and Ic SNe are found in galaxies from 10^6 to $10^{12}\,M_\odot$ (Section 4.5), and they select their hosts according to their star formation activity (Section 5.2). We also do not recover the overabundance of SNe IIb in low-mass galaxies in our complete sample. However, SNe Ic and SNe Ib are found in slightly more massive galaxies with higher absolute SFRs than SNe II and SNe IIb (Figure 14; Table 7), similar to what was seen by Arcavi et al. (2010).

The interpretation suggested by Arcavi et al. (2010), and in particular, that similar progenitors produce SNe Ib at high metallicity (more massive galaxies) and SNe IIb at lower metallicity, is not evident in our data. Localized metallicity studies at SN explosion sites, or direct progenitor metallicity studies of individual SN progenitors possible through rapid Hubble Space Telescope UV spectroscopy of infant SNe, could further illuminate this issue.

Graur et al. (2017b, 2017a) used the volume-limited Lick Observatory Supernova Search that primarily targeted massive

Table 7
Summary of the Anderson–Darling Tests

Sample	Sample Sizes	Chance Probability			
		Redshift	log M ($M_\odot$)	log SFR ($M_\odot \mathrm{yr}^{-1}$)	log sSFR (yr^{-1})
SN Ib versus SN Ic	46/60	0.048	0.345	0.287	0.191
SN Ic versus SN IIb	46/61	0.143	0.025	0.040	0.258
SN Ib versus SN IIb	46/61	0.187	0.025	0.032	0.155
SN Ic versus SN II	60/496	0.378	0.066	0.011	0.213
SN Ib versus SN II	46/496	0.025	0.076	0.018	0.206
SN Ibc versus SN IIb	118/61	0.233	0.015	0.032	0.190
SN Ibc versus SN II	118/496	0.112	0.035	0.004	0.206
SN IIb versus SN II	61/496	0.148	0.175	0.244	0.123

Note. The null hypothesis is that the test distribution is drawn from the parent distribution. We reject the null hypothesis if the chance probability is smaller than 5%.

galaxies at low redshifts. These authors reported that SNe Ibc are a factor of 2.5–3 less frequent in galaxies between $10^{9.5}$ and $10^{10.7}\,M_\odot$ and that the SN Ibc/SN II number ratio is the same in low-mass and high-mass galaxies. These authors also found a flattening of the SN Ibc/SN II ratio in galaxies with $M > 10^{10}\,M_\odot$. Our data set does not support the claimed rapid increase of the SN Ibc/SN II number ratio with galaxy mass. We find a moderate increase of the SN Ibc/SN II ratio by 25% from $\sim 10^{9.5}\,M_\odot$ to $\sim 10^{10.7}\,M_\odot$ (bottom-left panel in Figure 14). We do confirm that the SN IIb/SN II number ratio does not evolve with galaxy properties at a statistically significant level. Our data are inconclusive about whether the SNe Ibc/SN II number ratio is flattening in galaxies more massive than $\sim 10^{10}\,M_\odot$.

6. Conclusions

In this paper, we have presented all core-collapse supernovae detected by the Palomar Transient Factory between 2009 and mid-2017, and their host galaxies. This sample includes 888 objects from 12 distinct classes out to $z \approx 1$. We measured the brightness of the hosts from the FUV to the mid-IR and modeled their SEDs with stellar population nsynthesis models to extract physical properties, such as galaxy masses and star formation rates, as well as phenomenological properties, such as absolute magnitudes. Our main conclusions are as follows.

1. The PTF CCSN sample probes the complete spectrum of star-forming galaxies from $10^{5.4}$ to $10^{11.3}\,M_\odot$, including galaxies comparable to the least-massive star-forming galaxies in the Local Group. About 29% and 11% of the entire CCSN sample are found in galaxies less massive than 10^9 and $10^8\,M_\odot$, respectively. About 3% of all regular CCSNe are found in starbursting galaxies with specific star formation rates of $> 10^{-8}\,\mathrm{yr}^{-1}$. If SLSNe are included, the starburst frequency increases to 4.5%.
2. Regular CCSNe (Type Ib/c, IIb, II, and IIn) are direct tracers of star formation. Their mass functions are consistent with those of the general population of star-forming galaxies weighted by their star formation activity. The production efficiencies of their progenitor systems are nearly independent of the host-integrated metallicity and sSFR. Explosion-site studies are needed to identify the true environmental differences between these SN classes.
3. The mass, SFR, and sSFR distribution functions of Type Ib, Ic, IIb, and II SN host galaxies span the same ranges. However, the mass and SFR distribution functions of SN Ib+Ic+Ibc host galaxies (as individual classes and combined) are skewed toward galaxies with slightly higher masses and higher SFRs. These differences are less pronounced than in previous studies that were based on smaller and/or heterogeneous samples.
4. H-poor SLSNe, as well as SNe Ic-BL, are biased tracers of star formation. This bias can be corrected by introducing a metallicity-dependent production efficiency. The occurrence of H-poor SLSNe and SNe Ic-BL is stifled above an oxygen abundance of $12 + \log \mathrm{O/H} = 8.26^{+0.26}_{-0.30}$ ($\sim 0.4\,Z_\odot$) and $8.65^{+0.20}_{-0.14}$ ($\sim 1\,Z_\odot$), respectively, confirming previous studies. In addition, H-poor SLSNe are found in galaxies with younger stellar populations ($10^{8.3}$ versus $10^{9.7}$ yr) and higher sSFR $> 10^{-8}\,\mathrm{yr}^{-1}$ than all other SN classes discussed in this paper. This lends further support to the notion that low metallicity and young age play an important role in the formation of SLSN progenitors.
5. The samples of H-rich SLSNe and SNe Ibn are still too small to conclude whether their progenitors require special galaxy environments such as low metallicities.
6. The distribution functions of the projected distances of SNe to the center of their host galaxies extend to 37 kpc. In most cases, the projected distances are smaller than the expected 80%-light radii of their host galaxies. Fewer than 14% of all CCSNe (of all types) are found at larger distances, but in most cases still within the extent of the diffuse galaxy light.

On a more technical note, we conclude the following.

1. Galaxy surveys with limiting magnitudes of ~24.5 mag, such as the DESI Legacy Imaging Surveys, are sufficient to detect the host galaxies of almost every CCSN in transient surveys with limiting magnitudes of ~21. The host recovery rate of SLSNe is lower owing to their larger redshifts and their preference for low-luminosity galaxies.
2. The probability distributions of the host properties are characterized by a Gaussian core with different levels of asymmetry and pronounced wings, in particular toward the faint end. These shapes are reminiscent of the underlying luminosity and mass functions of star-forming galaxies and need to be taken into account to identify singular CCSN host galaxies.

We presented the host galaxies of the most common CCSN classes and indirectly constrained their progenitor populations. However, rare classes such as SNe Ibn and various flavors of

H-rich SLSNe (SLSN-II, SLSN-IIb, and SLSN-IIn) are still too scarce to constrain their host properties and quantify environment-dependent production efficiencies. The Zwicky Transient Facility (ZTF; Bellm et al. 2019; Graham et al. 2019) build larger and more homogeneous samples in a shorter period of time (Fremling et al. 2020; Perley et al. 2020). Like PTF, it uses the P48 telescope, but with a new camera having a 6× larger field of view. Furthermore, the implementation of a sophisticated alert-distribution system (Patterson et al. 2019) allows unbiased surveys with reproducible selection functions to be defined (such as the public ZTF Bright Transient Survey; Fremling et al. 2020), which can build samples containing thousands of CCSNe within a mere few years. The absence of an alert-distribution system inhibits us from quantifying the selection effects of the PTF survey.

Large and well-defined SN samples offer novel techniques to address open questions in galaxy science. The PTF CCSN sample revealed extreme environments of star formation, such as early-type galaxies (Irani et al. 2019), extremely low-mass galaxies (De et al. 2018), and starburst galaxies (Leloudas et al. 2015; Perley et al. 2016; Schulze et al. 2018). Galaxies with such extreme properties are also rare in an absolute sense. In S. Schulze et al. (2021, in preparation), we examine these peculiar environments in detail and show how SNe can be used as probes to identify these extreme environments in real time.

We thank the referee for a careful reading of the manuscript and for helpful comments that improved this paper.

We thank Nino Cucchiara, Thomas de Jaeger, Harald Ebeling, David Levitan, Bruce Margon, Jon Mauerhan, Jacob Rex, David Sand, Jeffrey M. Silverman, Vicky Toy, and Brad Tucker for performing some of the observations, and Ido Irani and Maryam Modjaz for valuable discussions.

I.A. is a CIFAR Azrieli Global Scholar in the Gravity and the Extreme Universe Program and acknowledges support from that program, from the European Research Council (ERC) under the European Unions Horizon 2020 research and innovation program (grant agreement 852097), from the Israel Science Foundation (grants 2108/18 and 2752/19), from the United States—Israel Binational Science Foundation (BSF), and from the Israeli Council for Higher Education Alon Fellowship. J.S.B. was partially supported by a Gordon and Betty Moore Foundation Data-Driven Discovery grant. The UCSC team is supported in part by National Aeronautics and Space Administration (NASA) grant NNG17PX03C, the Gordon & Betty Moore Foundation, the Heising-Simons Foundation, and by a fellowship from the David and Lucile Packard Foundation to R. J. Foley. A.V.F. acknowledges support from the US National Science Foundation (NSF), the Christopher R. Redlich Fund, the TABASGO Foundation, and the U.C. Berkeley Miller Institute for Basic Research in Science (in which he is a Miller Senior Fellow). M.F. is supported by a Royal Society—Science Foundation Ireland University Research Fellowship. A.G.-Y.'s research is supported by the EU via ERC grant 725161, the ISF GW excellence center, an IMOS space infrastructure grant and BSF/Transformative and GIF grants, as well as The Benoziyo Endowment Fund for the Advancement of Science, the Deloro Institute for Advanced Research in Space and Optics, The Veronika A. Rabl Physics Discretionary Fund, Paul and Tina Gardner, Yeda-Sela and the WIS-CIT joint research grant; A.G.-Y. is the recipient of the Helen and Martin Kimmel Award for Innovative Investigation. A.Y.Q.H. was supported by an NSF Graduate Research Fellowship under grant DGE1144469 and by the GROWTH project funded by the NSF under PIRE grant 1545949. D.A.H., G.H., and C.M. were supported by NSF grant AST-1313484. M. M.K. acknowledges support by the GROWTH (Global Relay of Observatories Watching Transients Happen) project funded by the NSF under PIRE Grant No. 1545949. S.K. was supported by the Ministry of Education, Science and Technological Development of the Republic of Serbia through contract 451-03-68/2020/14/20002 made with the Astronomical Observatory of Belgrade. G.L. is supported by a research grant (19054) from VILLUM FONDEN. R.L. is supported by a Marie Skłodowska-Curie Individual Fellowship within the Horizon 2020 European Union (EU) Framework Programme for Research and Innovation (H2020-MSCA-IF-2017-794467). K.M. acknowledges funding from EU H2020 ERC grant 758638. T.P. acknowledges the financial support from the Slovenian Research Agency (grants I0-0033, P1-0031, J1-8136, and Z1-1853). S.S. gratefully acknowledges support provided by the Feinberg Graduate School at the Weizmann Institute, Israel. A.H.W. is supported by a European Research Council Consolidator Grant (770935).

The Palomar Transient Factory project is a scientific collaboration among the California Institute of Technology, Los Alamos National Laboratory, the University of Wisconsin, Milwaukee, the Oskar Klein Center, the Weizmann Institute of Science, the TANGO Program of the University System of Taiwan, and the Kavli Institute for the Physics and Mathematics of the Universe. LANL participation in iPTF is supported by the US Department of Energy as a part of the Laboratory Directed Research and Development program.

This work makes use of data from the Las Cumbres Observatory network. Some of the data presented herein were obtained at the W. M. Keck Observatory, which is operated as a scientific partnership among the California Institute of Technology, the University of California, and NASA; the observatory was made possible by the generous financial support of the W. M. Keck Foundation. Research at Lick Observatory is partially supported by a generous gift from Google. The data presented herein were obtained in part with ALFOSC, which is provided by the Instituto de Astrofísica de Andalucía (IAA) under a joint agreement with the University of Copenhagen and NOTSA. The Cerro Tololo Inter-American Observatory and the National Optical Astronomy Observatory are operated by the Association of Universities for Research in Astronomy (AURA) under cooperative agreement with the NSF. We thank the staff of the various observatories at which data were obtained for their excellent assistance.

Funding for the Sloan Digital Sky Survey IV has been provided by the Alfred P. Sloan Foundation, the US Department of Energy Office of Science, and the Participating Institutions. SDSS-IV acknowledges support and resources from the Center for High-Performance Computing at the University of Utah. The SDSS website is www.sdss.org.

SDSS-IV is managed by the Astrophysical Research Consortium for the Participating Institutions of the SDSS Collaboration, including the Brazilian Participation Group, the Carnegie Institution for Science, Carnegie Mellon University, the Chilean Participation Group, the French Participation Group, the Harvard-Smithsonian Center for Astrophysics, Instituto de Astrofísica de Canarias, The Johns Hopkins University, Kavli Institute for the Physics and Mathematics of the Universe (IPMU)/University of Tokyo, Lawrence Berkeley National Laboratory, Leibniz Institut für Astrophysik

Potsdam (AIP), Max-Planck-Institut für Astronomie (MPIA Heidelberg), Max-Planck-Institut für Astrophysik (MPA Garching), Max-Planck-Institut für Extraterrestrische Physik (MPE), National Astronomical Observatories of China, New Mexico State University, New York University, University of Notre Dame, Observatário Nacional/MCTI, The Ohio State University, Pennsylvania State University, Shanghai Astronomical Observatory, United Kingdom Participation Group, Universidad Nacional Autónoma de México, University of Arizona, University of Colorado Boulder, University of Oxford, University of Portsmouth, University of Utah, University of Virginia, University of Washington, University of Wisconsin, Vanderbilt University, and Yale University.

The Pan-STARRS1 Surveys (PS1) have been made possible through contributions of the Institute for Astronomy, the University of Hawaii, the PanSTARRS Project Office, the Max-Planck Society and its participating institutes, the Max Planck Institute for Astronomy, Heidelberg, and the Max Planck Institute for Extraterrestrial Physics, Garching, The Johns Hopkins University, Durham University, the University of Edinburgh, Queen's University Belfast, the Harvard-Smithsonian Center for Astrophysics, the Las Cumbres Observatory Global Telescope Network Incorporated, the National Central University of Taiwan, the Space Telescope Science Institute, NASA under grant NNX08AR22G issued through the Planetary Science Division of the NASA Science Mission Directorate, the NSF under grant AST-1238877, the University of Maryland, and Eötvös Loránd University (ELTE).

This publication makes use of data products from the Two Micron All Sky Survey, which is a joint project of the University of Massachusetts and the Infrared Processing and Analysis Center/California Institute of Technology, funded by NASA and the NSF. This publication also makes use of data products from the Wide-field Infrared Survey Explorer, which is a joint project of the University of California, Los Angeles, and the Jet Propulsion Laboratory/California Institute of Technology, funded by NASA.

The LBNL Physics Division is supported by the US Department of Energy Office of Science High Energy Physics.

The National Energy Research Scientific Computing Center, which is supported by the Office of Science of the US Department of Energy under Contract DE-AC02-05CH11231, provided staff, computational resources, and data storage for this project.

The Computational HEP program in the Department of Energy's Science Office of High Energy Physics provided resources through the "Cosmology Data Repository" project (grant #KA2401022).

Software: Astropy v3.2.3 (Astropy Collaboration et al. 2013; 2018), Flexible Stellar Population Synthesis (FSPS; Conroy et al. 2009), High Order Transform of Psf ANd Template Subtraction v5.1.11 (Hotpants; Becker 2015), IRAF (Tody 1986), LAMBDAR (Wright et al. 2016), Prospector v0.3 (Leja et al. 2017), python-fsps (Foreman-Mackey et al. 2014) scikit-learn v0.21.2 (Pedregosa et al. 2011), Software for Calibrating AstroMetry and Photometry (SCAMP; Bertin 2006) v2.0.4, Source Extractor v2.19.5 (Bertin & Arnouts 1996), Supernova Identification v5.0 (Blondin & Tonry 2007), Superfit v3.5 (Howell et al. 2005).

Appendix A
Spectroscopic Log

A log of the spectroscopic observations, including references to the archival data, is shown in Table 8.

Table 8
Log of the Spectroscopic Observations

Object	Telescope/ Instrument	MJD (day)	Reference
PTF09as	Keck/LRIS	54921.55	2
PTF09atu	Keck/LRIS	55032.43	2
PTF09awk	Keck/LRIS	55034.31	3
PTF09axi	Keck/LRIS	55034.33	1
PTF09bce	Lick/Kast	55037.41	1
PTF09bcl	WHT/ISIS	55055.00	4
PTF09bcl	Keck/LRIS	55128.28	1
PTF09be	P200/DBSP	54948.33	1
PTF09bgf	Lick/Kast	55037.27	1
PTF09bw	Keck/LRIS	54921.57	1
PTF09cjq	Keck/LRIS	55126.00	1
PTF09cjq	Keck/LRIS	55126.32	1
PTF09cnd	WHT/ISIS	55055.00	2
PTF09ct	Keck/LRIS	54999.00	1
PTF09cu	P200/DBSP	54948.39	1
PTF09cvi	WHT/ISIS	55055.00	1
PTF09cvi	Keck/LRIS	55126.00	1
PTF09cvi	Keck/LRIS	55126.28	1
PTF09cwl	Keck/LRIS	55068.29	2, 5
PTF09dah	WHT/ISIS	55090.00	3
PTF09dfk	Keck/LRIS	55126.00	3
PTF09dh	Keck/LRIS	55097.00	3
PTF09dra	Keck/LRIS	55068.34	1
PTF09drs	Keck/LRIS	55233.00	1
PTF09dsj	Keck/LRIS	55068.26	3
PTF09due	Keck/LRIS	55126.00	1
PTF09due	Keck/LRIS	55126.25	1
PTF09dxv	WHT/ISIS	55115.00	3
PTF09dxv	Keck/LRIS	55126.00	1
PTF09dxv	Keck/LRIS	55126.41	1
PTF09dzt	Keck/LRIS	55097.00	3
PTF09ecm	P200/DBSP	55095.00	1
PTF09ecm	WHT/ISIS	55116.00	1
PTF09eqb	P200/DBSP	55126.00	1
PTF09fae	WHT/ISIS	55115.00	3
PTF09fae	WHT/ISIS	55115.86	1
PTF09fbf	WHT/ISIS	55115.00	1
PTF09fbf	Keck/LRIS	55128.00	1
PTF09fma	WHT/ISIS	55116.00	1
PTF09fma	Keck/LRIS	55127.00	1
PTF09fmk	WHT/ISIS	55116.00	1
PTF09foq	Keck/LRIS	55146.55	1
PTF09foy	Keck/LRIS	55126.00	1
PTF09foy	Keck/LRIS	55126.43	1
PTF09fqa	Keck/LRIS	55126.00	1
PTF09fsr	Keck/LRIS	55128.00	3
PTF09fsr	Keck/LRIS	55501.00	1
PTF09g	P200/DBSP	54910.49	1
PTF09gof	Keck/LRIS	55238.26	1
PTF09gpn	P200/DBSP	55143.41	6
PTF09gtt	Keck/LRIS	55146.00	1
PTF09gxq	Keck/LRIS	55146.00	3
PTF09gyp	Keck/LRIS	55146.00	3
PTF09hdo	Keck/LRIS	55146.40	1
PTF09hnq	HET/LRS	55160.00	3
PTF09hzg	Keck/LRIS	55184.00	1
PTF09iex	Keck/LRIS	55238.48	1
PTF09ige	Keck/LRIS	55233.00	1
PTF09igz	Keck/LRIS	55238.39	1
PTF09ij	P200/DBSP	54972.28	7
PTF09inv	P200/DBSP	55205.00	1

Table 8
(Continued)

Object	Telescope/ Instrument	MJD (day)	Reference
PTF09iqd	Keck/LRIS	55205.29	3
PTF09ism	P200/DBSP	55205.00	3
PTF09ps	Keck/LRIS	55008.00	3
PTF09q	P200/DBSP	54910.29	2
PTF09r	P200/DBSP	54910.50	1
PTF09sh	Keck/LRIS	55008.50	1
PTF09sk	Keck/LRIS	55008.30	1
PTF09t	P200/DBSP	54910.31	1
PTF09tm	Lick/Kast	55037.24	4
PTF09uj	Lick/Kast	55010.26	8
PTF09ut	Lick/Kast	55010.29	3
PTF09uy	Keck/LRIS	55008.28	2
PTF10aaes	WHT/ACAM	55507.01	1
PTF10aagc	Keck/LRIS	55505.00	2
PTF10aaho	Keck/LRIS	55538.40	1
PTF10aako	WHT/ACAM	55506.94	1
PTF10aauo	P200/DBSP	55543.00	1
PTF10aauu	P200/DBSP	55574.00	1
PTF10aauv	Lick/Kast	55530.28	1
PTF10aavz	WHT/ISIS	55530.00	9
PTF10aaxf	Keck/LRIS	55505.00	1
PTF10aazn	Keck/LRIS	55505.00	1
PTF10abav	Keck/LRIS	55538.48	1
PTF10abca	WHT/ISIS	55615.86	1
PTF10abck	Lick/Kast	55530.14	10
PTF10abcl	P200/DBSP	55536.00	1
PTF10abkc	P200/DBSP	55530.00	1
PTF10abmc	P200/DBSP	55530.00	1
PTF10abpr	Lick/Kast	55565.00	1
PTF10abrq	P200/DBSP	55536.00	1
PTF10absf	Keck/LRIS	55560.00	1
PTF10abte	P200/DBSP	55543.00	1
PTF10abui	P200/DBSP	55536.00	4
PTF10abyy	Lick/Kast	55574.00	1
PTF10acbu	P200/DBSP	55543.00	3
PTF10acbu	KPNO/RC Spec	55593.00	1
PTF10acfd	Keck/LRIS	55560.00	1
PTF10acff	Gemini-North/GMOS	55544.00	3
PTF10acgq	Keck/LRIS	55560.00	3
PTF10achk	Keck/LRIS	55560.00	1
PTF10acrm	Keck/LRIS	55560.00	1
PTF10acrt	P200/DBSP	55601.00	1
PTF10acsq	KPNO/RC Spec	55662.00	1
PTF10ad	P200/DBSP	55205.00	1
PTF10bau	VLT/X-Shooter	55228.00	1
PTF10bau	Keck/DEIMOS	55242.00	1
PTF10bau	Keck/LRIS	55269.27	1
PTF10bfz	Keck/LRIS	55234.58	2
PTF10bgl	Keck/LRIS	55233.00	1
PTF10bhu	WHT/ISIS	55249.00	3
PTF10bip	WHT/ISIS	55249.00	3
PTF10bjb	Keck/LRIS	55262.00	1
PTF10bjp	Keck/LRIS	55262.00	2
PTF10bld	Keck/LRIS	55262.00	1
PTF10bwo	Keck/LRIS	55262.00	1
PTF10bzf	Gemini-North/GMOS	55256.00	11
PTF10cd	Keck/LRIS	55205.30	1
PTF10ciw	Keck/LRIS	55262.00	6
PTF10con	P200/DBSP	55273.00	1
PTF10cqh	P200/DBSP	55273.00	1
PTF10cs	P200/DBSP	55205.00	1
PTF10cwl	Keck/LRIS	55269.63	6
PTF10cwr	P200/DBSP	55273.00	5
PTF10cwx	P200/DBSP	55273.00	4
PTF10cxq	P200/DBSP	55273.00	1
PTF10cxx	P200/DBSP	55273.00	3
PTF10czn	Keck/LRIS	55322.47	1
PTF10dk	P200/DBSP	55205.00	1
PTF10dvb	P200/DBSP	55294.00	1
PTF10ehy	Keck/LRIS	55331.00	1
PTF10eoo	WHT/ACAM	55357.10	1
PTF10eqe	P200/DBSP	55323.00	1
PTF10eqi	P200/DBSP	55294.00	3
PTF10eqz	WHT/ISIS	55286.00	1
PTF10ewc	WHT/ISIS	55285.00	4
PTF10fbv	Keck/LRIS	55291.00	3
PTF10fei	Keck/LRIS	55385.00	1
PTF10fel	Keck/LRIS	55384.45	1
PTF10feq	WHT/ISIS	55318.00	3
PTF10ffx	Keck/LRIS	55322.49	1
PTF10fgz	P200/DBSP	55294.00	1
PTF10fhk	Gemini-North/GMOS	55296.00	1
PTF10fia	Keck/LRIS	55302.00	3
PTF10fjh	Gemini-North/GMOS	55300.00	4
PTF10fjh	WHT/ISIS	55319.00	1
PTF10fjq	WHT/ISIS	55319.00	1
PTF10flx	Gemini-North/GMOS	55299.00	4
PTF10fmr	WHT/ISIS	55320.00	3
PTF10fmx	Keck/LRIS	55331.00	3
PTF10fmx	P200/DBSP	55360.00	1
PTF10fou	Keck/LRIS	55301.00	1
PTF10fqg	P200/DBSP	55323.00	3
PTF10fqx	P200/DBSP	55323.00	1
PTF10fya	Keck/LRIS	55359.00	1
PTF10gki	Lick/Kast	55330.00	1
PTF10glp	P200/DBSP	55396.00	1
PTF10gmf	Lick/Kast	55330.00	3
PTF10gnc	Keck/LRIS	55322.28	1
PTF10gnc	Keck/LRIS	55385.00	1
PTF10gqf	P200/DBSP	55323.00	1
PTF10gtn	Keck/LRIS	55385.00	1
PTF10gva	Keck/LRIS	55359.00	1
PTF10gvb	Keck/LRIS	55331.00	2
PTF10gvd	Keck/LRIS	55322.43	4
PTF10gvf	Keck/LRIS	55322.52	7
PTF10gvf	Keck/LRIS	55331.00	1
PTF10gxi	P200/DBSP	55360.00	1
PTF10gym	Keck/LRIS	55355.00	1
PTF10hbf	P200/DBSP	55337.00	1
PTF10hcr	P200/DBSP	55337.00	1
PTF10hdq	Keck/LRIS	55359.00	1
PTF10heh	Keck/LRIS	55419.00	1
PTF10hfe	Keck/LRIS	55355.00	3
PTF10hgi	Keck/LRIS	55385.26	2
PTF10hie	Keck/DEIMOS	55358.00	3
PTF10hif	P200/DBSP	55337.00	1
PTF10hlc	Lick/Kast	55365.00	1
PTF10hmg	P200/DBSP	55337.00	1
PTF10hny	Keck/LRIS	55355.00	1
PTF10hpa	P200/DBSP	55391.00	1
PTF10hsn	Keck/LRIS	55355.00	1
PTF10hv	Keck/LRIS	55210.00	1

Table 8
(Continued)

Object	Telescope/ Instrument	MJD (day)	Reference
PTF10hvz	Keck/LRIS	55385.00	1
PTF10hyq	Lick/Kast	55418.00	1
PTF10ikr	Keck/LRIS	55385.00	1
PTF10in	Keck/LRIS	55233.00	3
PTF10inj	P200/DBSP	55391.00	3
PTF10iue	Keck/LRIS	55385.00	12
PTF10iwb	WHT/ISIS	55409.00	1
PTF10jkx	Keck/LRIS	55385.00	1
PTF10jop	Keck/DEIMOS	55358.00	1
PTF10jwd	Keck/LRIS	55384.48	1
PTF10jwr	Keck/LRIS	55384.42	1
PTF10jws	P200/DBSP	55392.00	1
PTF10ksq	Keck/LRIS	55364.00	1
PTF10kui	Keck/LRIS	55385.00	3
PTF10lbo	Keck/LRIS	55364.00	3
PTF10llv	Keck/LRIS	55419.00	1
PTF10lnx	WHT/ISIS	55383.00	1
PTF10lyb	P200/DBSP	55416.00	1
PTF10mug	P200/DBSP	55416.00	1
PTF10mwt	P200/DBSP	55391.00	1
PTF10myz	Keck/LRIS	55419.00	1
PTF10nbf	Keck/LRIS	55419.00	1
PTF10ndr	P200/DBSP	55384.00	1
PTF10ngx	P200/DBSP	55384.00	1
PTF10nmn	Keck/LRIS	55384.43	1
PTF10nmn	Keck/LRIS	55977.00	2
PTF10npd	Keck/LRIS	55444.47	1
PTF10oet	WHT/ISIS	55410.00	1
PTF10ofb	P200/DBSP	55391.00	1
PTF10ood	P200/DBSP	55396.00	1
PTF10ooe	Keck/LRIS	55444.24	1
PTF10osn	Keck/LRIS	55419.00	3
PTF10osr	Lick/Kast	55480.00	1
PTF10oug	P200/DBSP	55396.00	4
PTF10pbi	Keck/LRIS	55419.00	3
PTF10pjg	P200/DBSP	55445.00	1
PTF10prt	P200/DBSP	55422.00	1
PTF10pzp	Keck/LRIS	55419.00	3
PTF10qaf	Keck/LRIS	55419.00	1
PTF10qif	Keck/LRIS	55444.44	3
PTF10qkg	Keck/LRIS	55419.00	1
PTF10qob	Keck/LRIS	55444.53	1
PTF10qqd	Keck/LRIS	55419.50	3
PTF10qqh	KPNO/RC Spec	55480.00	1
PTF10qrl	Keck/LRIS	55444.46	3
PTF10qts	P200/DBSP	55444.00	13
PTF10qwu	P200/DBSP	55421.00	4
PTF10qwz	Lick/Kast	55419.41	1
PTF10rad	Keck/LRIS	55444.50	1
PTF10raj	Keck/LRIS	55444.63	1
PTF10rem	Keck/DEIMOS	55481.00	1
PTF10rex	P200/DBSP	55422.00	1
PTF10rin	P200/DBSP	55422.00	1
PTF10rjs	P200/DBSP	55445.00	1
PTF10rmn	Lick/Kast	55424.46	1
PTF10s	Keck/LRIS	55234.52	1
PTF10scc	Keck/LRIS	55472.00	1
PTF10svt	P200/DBSP	55536.00	3
PTF10tel	Gemini-North/GMOS	55434.00	14
PTF10tff	Lick/Kast	55442.00	1
PTF10tjr	Lick/Kast	55442.00	1
PTF10tpa	Keck/LRIS	55472.00	1
PTF10tpz	Keck/LRIS	55501.00	1
PTF10tqi	P200/DBSP	55443.00	3
PTF10tqv	P200/DBSP	55441.00	9
PTF10tru	KPNO/RC Spec	55503.00	1
PTF10ts	Keck/LRIS	55210.00	1
PTF10ttd	P200/DBSP	55441.00	1
PTF10ttm	Keck/DEIMOS	55481.00	1
PTF10ttp	Keck/LRIS	55483.00	1
PTF10ttz	Keck/LRIS	55501.00	1
PTF10tud	P200/DBSP	55443.00	3
PTF10tue	KPNO/RC Spec	55478.00	1
PTF10tuj	KPNO/RC Spec	55480.00	1
PTF10tyd	P200/DBSP	55443.00	4
PTF10tzh	Keck/DEIMOS	55481.00	1
PTF10u	Keck/LRIS	55233.00	1
PTF10uhf	Keck/LRIS	55472.28	2
PTF10uiy	Lick/Kast	55480.00	1
PTF10uiz	Keck/LRIS	55472.00	1
PTF10ujc	Lick/Kast	55455.37	1
PTF10uls	KPNO/RC Spec	55480.00	1
PTF10umz	WHT/ISIS	55499.00	1
PTF10uqg	Keck/LRIS	55472.00	1
PTF10uqn	Keck/LRIS	55472.00	1
PTF10vag	Lick/Kast	55454.21	4
PTF10vdl	HET/LRS	55468.00	15
PTF10vgv	Lick/Kast	55470.00	16
PTF10viv	KPNO/RC Spec	55480.00	1
PTF10vns	P200/DBSP	55499.00	3
PTF10vnv	P200/DBSP	55477.00	3
PTF10vqv	Keck/LRIS	55538.44	2
PTF10vwg	Keck/LRIS	55483.00	2
PTF10wal	Keck/LRIS	55501.00	3
PTF10wcy	Keck/LRIS	55472.00	1
PTF10weh	KPNO/RC Spec	55503.00	1
PTF10wmf	Lick/Kast	55502.00	1
PTF10wmk	Keck/LRIS	55505.00	1
PTF10wnp	KPNO/RC Spec	55479.00	1
PTF10wop	KPNO/RC Spec	55478.00	1
PTF10wve	Keck/LRIS	55472.00	1
PTF10xem	Keck/LRIS	55501.00	9
PTF10xfh	Keck/LRIS	55501.00	1
PTF10xfl	P200/DBSP	55486.00	3
PTF10xfw	KPNO/RC Spec	55478.00	1
PTF10xgo	Keck/LRIS	55507.29	1
PTF10xif	Keck/LRIS	55501.00	1
PTF10xik	P200/DBSP	55486.00	3
PTF10xiw	P200/DBSP	55536.00	1
PTF10xjr	P200/DBSP	55486.00	3
PTF10xjv	Lick/Kast	55515.00	1
PTF10xla	KPNO/RC Spec	55504.00	1
PTF10xlr	KPNO/RC Spec	55502.00	1
PTF10xmi	Keck/LRIS	55501.00	1
PTF10xtq	P200/DBSP	55536.00	1
PTF10xzs	KPNO/RC Spec	55502.00	1
PTF10yna	P200/DBSP	55536.00	1
PTF10yow	WHT/ISIS	55500.00	1
PTF10ypi	P200/DBSP	55536.00	1
PTF10ysd	P200/DBSP	55486.00	9
PTF10ysx	Keck/LRIS	55515.00	1
PTF10yxk	Keck/LRIS	55538.33	1

Table 8
(Continued)

Object	Telescope/ Instrument	MJD (day)	Reference
PTF10yyc	Keck/LRIS	55505.00	1
PTF10yzt	Lick/Kast	55515.00	1
PTF10zcn	KPNO/RC Spec	55502.00	1
PTF10ze	Keck/LRIS	55238.27	1
PTF11acz	P200/DBSP	55630.00	1
PTF11aib	KPNO/RC Spec	55593.00	1
PTF11ajz	P200/DBSP	55630.00	1
PTF11akn	Keck/LRIS	55624.00	1
PTF11ams	P200/DBSP	55706.00	1
PTF11asb	Keck/LRIS	55714.50	1
PTF11aun	WHT/ISIS	55615.90	1
PTF11awe	Keck/LRIS	55629.00	1
PTF11bgl	WHT/ISIS	55683.00	1
PTF11bli	UH88/SNIFS	55650.00	1
PTF11bni	P200/DBSP	55674.00	1
PTF11bov	KPNO/RC Spec	55692.00	1
PTF11bpx	P200/DBSP	55706.00	1
PTF11cag	WHT/ISIS	55721.00	1
PTF11cda	WHT/ISIS	55683.00	1
PTF11cgx	KPNO/RC Spec	55694.00	1
PTF11cmh	WHT/ISIS	55683.00	9
PTF11csc	Gemini-North/GMOS	55701.41	1
PTF11cwi	KPNO/RC Spec	55694.00	1
PTF11cyw	P200/DBSP	55706.00	1
PTF11dad	P200/DBSP	55706.00	1
PTF11dhf	P200/DBSP	55706.00	1
PTF11dij	P200/DBSP	55706.00	2
PTF11dlg	Keck/LRIS	55714.00	1
PTF11dqk	P200/DBSP	55706.00	1
PTF11dqr	Keck/LRIS	55714.00	1
PTF11dqr	Keck/LRIS	55714.48	1
PTF11dsf	Keck/LRIS	55714.00	1
PTF11dsz	KPNO/RC Spec	55719.00	1
PTF11dtd	KPNO/RC Spec	55719.00	1
PTF11ecp	P200/DBSP	55768.00	1
PTF11ekj	Keck/DEIMOS	55747.51	1
PTF11emc	KPNO/RC Spec	55719.00	1
PTF11emo	P200/DBSP	55801.00	1
PTF11eon	P200/DBSP	55736.00	3
PTF11epi	Keck/LRIS	55715.00	1
PTF11fma	P200/DBSP	55736.00	1
PTF11fss	P200/DBSP	55736.00	1
PTF11ftc	Lick/Kast	55748.00	1
PTF11ftr	WHT/ISIS	55771.00	1
PTF11fuu	Keck/LRIS	55804.00	1
PTF11fuv	P200/DBSP	55736.00	1
PTF11fve	P200/DBSP	55779.00	1
PTF11fvi	P200/DBSP	55736.00	1
PTF11fzz	P200/DBSP	55736.00	4
PTF11gcj	P200/DBSP	55741.00	3
PTF11gdz	P200/DBSP	55741.00	1
PTF11gls	P200/DBSP	55776.22	1
PTF11go	P200/DBSP	55589.00	1
PTF11gtr	Keck/LRIS	55744.54	1
PTF11hqs	WHT/ISIS	55827.00	1
PTF11hrq	P200/DBSP	55921.00	2
PTF11hsj	P200/DBSP	55779.00	1
PTF11htj	Lick/Kast	55777.42	1
PTF11hyg	P200/DBSP	55768.00	3
PTF11iil	Keck/DEIMOS	55774.00	1
PTF11ilr	WHT/ISIS	55770.00	3
PTF11img	Keck/LRIS	55775.39	9
PTF11iqb	P200/DBSP	55825.00	1
PTF11iwl	WHT/ISIS	55772.00	1
PTF11ixk	P200/DBSP	55768.00	3
PTF11izq	TNG/DOLORES	55792.00	3
PTF11izt	WHT/ISIS	55804.00	17
PTF11jgj	P200/DBSP	55779.00	3
PTF11jgp	Keck/LRIS	55804.00	1
PTF11jx	P200/DBSP	55589.00	1
PTF11kaa	TNG/DOLORES	55793.00	3
PTF11kjk	Keck/DEIMOS	55833.00	1
PTF11kku	WHT/ISIS	55828.00	1
PTF11klg	P200/DBSP	55807.00	3
PTF11kpa	P200/DBSP	55807.00	1
PTF11ktr	Keck/LRIS	55801.34	1
PTF11lbm	P200/DBSP	55825.00	9
PTF11lmn	WHT/ISIS	55827.00	3
PTF11lnq	UH88/SNIFS	55813.28	1
PTF11me	P200/DBSP	55589.00	1
PTF11mhh	WHT/ISIS	55828.00	1
PTF11mhr	Keck/LRIS	56421.58	1
PTF11mlk	APO/DIS	55851.49	1
PTF11mmk	P200/DBSP	55825.00	1
PTF11mnb	P200/DBSP	55864.00	2
PTF11mpg	Keck/DEIMOS	55833.00	4
PTF11mpv	WHT/ISIS	55828.00	1
PTF11msk	WHT/ISIS	55827.00	1
PTF11msl	WHT/ISIS	55828.00	1
PTF11mtq	UH88/SNIFS	55828.23	1
PTF11mwk	Keck/DEIMOS	55833.00	3
PTF11ner	Keck/LRIS	55897.54	1
PTF11oey	Keck/DEIMOS	55865.00	1
PTF11oiy	P200/DBSP	55864.00	1
PTF11oxu	WHT/ISIS	55872.00	4
PTF11pab	UH88/SNIFS	55856.47	1
PTF11pbo	P200/DBSP	55864.00	1
PTF11pdj	WHT/ISIS	55913.00	3
PTF11pnq	Keck/DEIMOS	55863.00	3
PTF11po	Keck/LRIS	55624.00	3
PTF11prr	Keck/LRIS	55926.00	3
PTF11pym	P200/DBSP	55922.00	1
PTF11qax	Lick/Kast	55913.20	1
PTF11qcc	P200/DBSP	55916.00	1
PTF11qcj	WHT/ISIS	55872.00	18
PTF11qcm	P200/DBSP	55916.00	1
PTF11qgw	WHT/ISIS	55916.00	1
PTF11qiq	P200/DBSP	55895.00	3
PTF11qju	Keck/LRIS	55977.00	3
PTF11qnf	Keck/LRIS	55891.54	4
PTF11qqj	KPNO/RC Spec	55952.00	1
PTF11qux	Keck/LRIS	55897.64	1
PTF11rfh	Keck/LRIS	55926.00	19
PTF11rfr	P200/DBSP	56127.00	1
PTF11rka	Keck/LRIS	55921.65	20
PTF11rkm	Keck/DEIMOS	56006.56	3
PTF11rks	P200/DBSP	55922.00	2
PTF11rlv	KPNO/RC Spec	55953.00	4
PTF11vb	Lick/Kast	55601.00	1
PTF11vb	WHT/ISIS	55615.13	1
PTF12as	APO/DIS	55928.54	9
PTF12bbm	Keck/LRIS	56001.47	1

Table 8
(Continued)

Object	Telescope/ Instrument	MJD (day)	Reference
PTF12bdp	WHT/ISIS	55988.00	1
PTF12bnv	Keck/LRIS	56001.47	1
PTF12boj	Keck/LRIS	56001.56	1
PTF12bpy	P200/DBSP	56046.00	1
PTF12bro	P200/DBSP	56046.00	17
PTF12bup	P200/DBSP	56006.00	1
PTF12bvh	Lick/Kast	56068.17	1
PTF12bwq	WHT/ACAM	56022.00	3
PTF12cbo	P200/DBSP	56046.00	1
PTF12cdc	WHT/ISIS	56104.00	1
PTF12cde	Keck/LRIS	56046.55	3
PTF12cfu	P200/DBSP	56046.00	1
PTF12cgb	WHT/ISIS	56104.00	1
PTF12cix	WHT/ACAM	56022.00	1
PTF12cjy	P200/DBSP	56037.00	3
PTF12cli	APO/DIS	56029.27	1
PTF12cod	TNG/DOLORES	56078.00	17
PTF12csy	Gemini-North/GMOS	56034.00	1
PTF12cxj	Gemini-North/GMOS	56035.00	4
PTF12dam	Lick/Kast	56067.32	2
PTF12dcp	Keck/LRIS	56064.42	3
PTF12dcp	Keck/LRIS	56064.42	1
PTF12dke	Keck/LRIS	56069.00	1
PTF12dtf	Keck/LRIS	56124.44	3
PTF12eaw	P200/DBSP	56076.00	3
PTF12eci	Keck/LRIS	56064.25	4
PTF12eec	TNG/DOLORES	56076.00	1
PTF12efk	Keck/LRIS	56094.46	1
PTF12eje	WHT/ISIS	56072.00	3
PTF12elh	Keck/LRIS	56094.56	1
PTF12emw	Gemini-North/GMOS	56065.00	1
PTF12eog	P200/DBSP	56135.00	1
PTF12epg	Keck/LRIS	56069.00	1
PTF12esl	Keck/LRIS	56069.00	1
PTF12eur	Keck/DEIMOS	56270.00	1
PTF12exc	Lick/Kast	56092.43	1
PTF12fes	Keck/LRIS	56124.39	3
PTF12ffs	P200/DBSP	56129.00	1
PTF12fgw	APO/DIS	56104.36	3
PTF12fhz	Keck/LRIS	56158.28	3
PTF12fip	P200/DBSP	56129.00	1
PTF12fkp	Keck/LRIS	56123.27	1
PTF12fo	Lick/Kast	55959.00	1
PTF12frn	P200/DBSP	56135.00	1
PTF12ftc	Keck/LRIS	56123.32	1
PTF12fxj	Lick/Kast	56119.48	3
PTF12gcx	Keck/DEIMOS	56124.00	6
PTF12gdy	P200/DBSP	56123.00	1
PTF12ggi	Keck/DEIMOS	56184.00	1
PTF12glz	P200/DBSP	56123.00	21
PTF12gnn	WHT/ISIS	56160.00	1
PTF12gnt	P200/DBSP	56134.00	1
PTF12gpn	Lick/Kast	56125.46	3
PTF12gps	P200/DBSP	56135.00	3
PTF12grj	P200/DBSP	56127.00	17
PTF12grr	P200/DBSP	56129.00	1
PTF12gty	P200/DBSP	56135.00	2
PTF12gvr	UH88/SNIFS	56133.40	3
PTF12gwu	Keck/LRIS	56421.40	22
PTF12gxj	P200/DBSP	56135.00	1
PTF12gzk	TNG/DOLORES	56145.00	3
PTF12gzk	Keck/LRIS	56544.46	1
PTF12hni	Lick/Kast	56148.42	2
PTF12hno	WHT/ISIS	56160.00	1
PTF12hsx	WHT/ISIS	56160.00	1
PTF12hvv	WHT/ISIS	56160.00	3
PTF12hvv	Keck/DEIMOS	56193.00	1
PTF12hxz	Keck/DEIMOS	56214.59	1
PTF12iet	Keck/LRIS	56217.21	1
PTF12iif	Lick/Kast	56177.00	1
PTF12iqw	Keck/DEIMOS	56214.60	3
PTF12izy	P200/DBSP	56244.00	1
PTF12jaa	P200/DBSP	56238.00	3
PTF12jfp	P200/DBSP	56244.00	1
PTF12jfv	Keck/DEIMOS	56214.30	1
PTF12jgd	APO/DIS	56211.13	1
PTF12jgi	WHT/ISIS	56222.00	1
PTF12jiv	UH88/SNIFS	56206.47	1
PTF12jje	Gemini-North/GMOS	56206.00	1
PTF12jje	UH88/SNIFS	56206.41	1
PTF12jjg	Keck/DEIMOS	56214.58	1
PTF12jqj	Keck/DEIMOS	56214.62	1
PTF12jut	P200/DBSP	56238.00	1
PTF12jvp	Keck/DEIMOS	56270.00	1
PTF12jvy	Keck/LRIS	56273.48	1
PTF12jxd	Keck/DEIMOS	56301.40	3
PTF12jxe	Lick/Kast	56237.00	1
PTF12khf	P200/DBSP	56238.00	1
PTF12khj	P200/DBSP	56238.00	1
PTF12kph	Keck/LRIS	56273.31	1
PTF12krf	P200/DBSP	56266.00	1
PTF12kso	P200/DBSP	56238.00	6
PTF12ksy	P200/DBSP	56238.00	4
PTF12kth	P200/DBSP	56238.00	1
PTF12ktu	P200/DBSP	56238.00	3
PTF12lbj	Keck/LRIS	56273.53	1
PTF12ldy	Keck/DEIMOS	56270.00	1
PTF12ljg	Keck/LRIS	56360.22	1
PTF12lpo	P200/DBSP	56266.00	3
PTF12ltw	Keck/LRIS	56273.45	3
PTF12lvj	P200/DBSP	56266.00	1
PTF12lvs	P200/DBSP	56266.00	1
PTF12lvt	P200/DBSP	56266.00	3
PTF12mau	APO/DIS	56265.09	1
PTF12mav	APO/DIS	56265.06	1
PTF12mca	P200/DBSP	56341.00	1
PTF12mfx	Keck/DEIMOS	56300.38	3
PTF12mhg	Keck/LRIS	56279.51	1
PTF12mja	Keck/LRIS	56279.62	1
PTF12mkp	Keck/LRIS	56279.49	1
PTF12mue	Keck/DEIMOS	56300.33	1
PTF12mxx	Keck/LRIS	56279.28	2
PTF12ne	P200/DBSP	55956.00	1
PTF12os	Keck/LRIS	55977.00	23
PTF12th	KPNO/RC Spec	55952.00	1
PTF12th	NOT/ALFOSC	55983.00	1
PTF12xv	P200/DBSP	55958.00	1
iPTF13aaz	P200/DBSP	56395.00	1
iPTF13ab	P200/DBSP	56341.00	3
iPTF13aby	Keck/LRIS	56391.55	3
iPTF13agz	P200/DBSP	56445.00	1
iPTF13ajg	Keck/DEIMOS	56390.00	24

Table 8
(Continued)

Object	Telescope/ Instrument	MJD (day)	Reference
iPTF13ajn	P200/DBSP	56446.00	3
iPTF13akg	Keck/DEIMOS	56449.00	1
iPTF13aki	Keck/DEIMOS	56449.00	1
iPTF13al	P200/DBSP	56341.00	1
iPTF13ala	P200/DBSP	56414.17	1
iPTF13alq	P200/DBSP	56395.00	9
iPTF13ao	P200/DBSP	56341.00	1
iPTF13aoj	P200/DBSP	56414.20	1
iPTF13aoo	P200/DBSP	56414.46	3
iPTF13aot	P200/DBSP	56478.00	3
iPTF13aqf	Keck/DEIMOS	56485.00	1
iPTF13aqj	Keck/LRIS	56452.33	1
iPTF13asr	Keck/LRIS	56421.28	4
iPTF13ast	APO/DIS	56470.19	3
iPTF13b	APO/DIS	56328.35	1
iPTF13bdl	Keck/DEIMOS	56448.00	1
iPTF13beo	P200/DBSP	56446.00	25
iPTF13bg	Keck/LRIS	56332.40	1
iPTF13bjx	P200/DBSP	56478.00	1
iPTF13bjz	Keck/LRIS	56452.31	1
iPTF13bks	Keck/DEIMOS	56484.00	1
iPTF13bld	P200/DBSP	56478.00	1
iPTF13blq	Keck/DEIMOS	56485.38	3
iPTF13bnu	Magellan/IMACS	56459.00	1
iPTF13bsg	P200/DBSP	56478.00	1
iPTF13bt	APO/DIS	56342.35	1
iPTF13btt	P200/DBSP	56478.00	1
iPTF13bu	Keck/LRIS	56391.46	1
iPTF13bvn	P200/DBSP	56478.00	26
iPTF13bxj	P200/DBSP	56489.00	1
iPTF13bxl	Keck/DEIMOS	56506.00	9
iPTF13bxl	Keck/DEIMOS	56506.00	1
iPTF13c	APO/DIS	56328.34	1
iPTF13cab	P200/DBSP	56507.00	3
iPTF13cac	P200/DBSP	56507.00	1
iPTF13cbf	P200/DBSP	56507.00	3
iPTF13ccj	Keck/DEIMOS	56506.00	3
iPTF13cco	Keck/LRIS	56544.59	1
iPTF13ccu	P200/DBSP	56518.00	1
iPTF13cjq	P200/DBSP	56507.00	1
iPTF13ckf	Magellan/IMACS	56538.00	1
iPTF13clj	P200/DBSP	56539.35	1
iPTF13cly	Magellan/IMACS	56538.00	1
iPTF13cnk	Keck/DEIMOS	56569.00	1
iPTF13co	APO/DIS	56342.33	1
iPTF13cp	APO/DIS	56342.32	1
iPTF13cr	P200/DBSP	56341.00	3
iPTF13cuf	Keck/DEIMOS	56545.00	4
iPTF13cuv	P200/DBSP	56539.00	3
iPTF13czn	Magellan/IMACS	56538.00	1
iPTF13czt	Magellan/IMACS	56538.00	1
iPTF13d	APO/DIS	56328.42	1
iPTF13dao	Magellan/IMACS	56538.00	1
iPTF13daz	Gemini-North/GMOS	56533.00	1
iPTF13dcc	Keck/LRIS	56630.46	1
iPTF13dhq	Keck/LRIS	56544.52	1
iPTF13dht	Keck/LRIS	56544.52	3
iPTF13djf	APO/DIS	56561.27	3
iPTF13dkk	P200/DBSP	56570.19	1
iPTF13dkz	P200/DBSP	56598.46	1
iPTF13dla	Keck/LRIS	56628.38	1
iPTF13dmv	P200/DBSP	56570.12	1
iPTF13dmv	P200/DBSP	56598.10	1
iPTF13dnt	P200/DBSP	56569.20	9
iPTF13dol	P200/DBSP	56569.21	3
iPTF13dqy	P200/DBSP	56598.21	27
iPTF13dug	P200/DBSP	56598.49	3
iPTF13duv	Keck/LRIS	56980.20	1
iPTF13dza	Keck/LRIS	56628.48	1
iPTF13dzb	FTS/FLOYDS	56623.45	1
iPTF13dzy	Keck/LRIS	56629.35	1
iPTF13eal	P200/DBSP	56622.00	1
iPTF13ebs	Keck/LRIS	56628.53	3
iPTF13ebw	Keck/LRIS	56630.49	1
iPTF13ece	Keck/DEIMOS	56625.00	1
iPTF13ecn	Keck/LRIS	56628.55	1
iPTF13ecz	Keck/LRIS	56628.54	1
iPTF13edf	Keck/DEIMOS	56625.00	3
iPTF13edi	Keck/DEIMOS	56625.00	1
iPTF13eds	Keck/DEIMOS	56625.00	1
iPTF13eeh	P200/DBSP	56663.00	28
iPTF13eeo	Keck/LRIS	56628.52	1
iPTF13eer	Keck/LRIS	56628.53	1
iPTF13eew	Keck/LRIS	56628.47	1
iPTF13efs	Keck/DEIMOS	56637.59	1
iPTF13ehe	Keck/DEIMOS	56658.00	1
iPTF13ejp	APO/DIS	56666.12	1
iPTF13h	P200/DBSP	56341.00	1
iPTF13jw	P200/DBSP	56368.00	1
iPTF13nu	P200/DBSP	56395.00	3
iPTF13oh	Lick/Kast	56386.00	1
iPTF13qu	P200/DBSP	56368.00	1
iPTF13rk	P200/DBSP	56368.00	1
iPTF13u	P200/DBSP	56341.00	9
iPTF13ua	P200/DBSP	56368.00	1
iPTF13um	P200/DBSP	56368.00	1
iPTF13ut	Magellan/FIRE	56386.00	1
iPTF13v	APO/DIS	56328.44	3
iPTF13z	P200/DBSP	56341.00	29
iPTF13zl	HET/LRS	56388.00	1
iPTF14aag	APO/DIS	56739.34	3
iPTF14abc	P200/DBSP	56751.00	1
iPTF14adz	Keck/LRIS	56776.38	1
iPTF14afz	P200/DBSP	56781.36	1
iPTF14ait	P200/DBSP	56751.00	3
iPTF14ajh	APO/DIS	56756.37	1
iPTF14ajq	APO/DIS	56756.35	1
iPTF14ajx	P200/DBSP	56781.26	1
iPTF14aki	Keck/LRIS	56805.38	19
iPTF14ald	Keck/LRIS	56805.32	1
iPTF14amd	P200/DBSP	56781.18	1
iPTF14aoi	Lick/Kast	56838.00	1
iPTF14aol	Keck/DEIMOS	56774.00	1
iPTF14apl	P200/DBSP	56781.19	3
iPTF14asz	APO/DIS	56783.33	1
iPTF14atc	APO/DIS	56783.37	3
iPTF14atc	Keck/LRIS	56805.35	1
iPTF14awf	P200/DBSP	56801.00	1
iPTF14axx	NOT/ALFOSC	56790.00	1
iPTF14ayo	APO/DIS	56798.32	1

Table 8
(Continued)

Object	Telescope/ Instrument	MJD (day)	Reference
iPTF14bag	Keck/LRIS	56837.25	1
iPTF14bas	Keck/LRIS	56899.30	3
iPTF14bbs	P200/DBSP	56814.00	1
iPTF14bcw	Keck/DEIMOS	56803.00	4
iPTF14bcz	Keck/DEIMOS	56803.00	1
iPTF14bfu	Keck/LRIS	56837.55	1
iPTF14bgp	APO/DIS	56817.22	1
iPTF14bgw	P200/DBSP	56832.31	1
iPTF14bpa	P200/DBSP	56832.28	4
iPTF14bpy	P200/DBSP	56832.30	3
iPTF14cvn	Keck/LRIS	56868.30	1
iPTF14cwd	Keck/LRIS	56869.43	1
iPTF14cyn	Keck/LRIS	56869.30	3
iPTF14dby	Keck/LRIS	56837.40	9
iPTF14dck	Keck/LRIS	56837.37	1
iPTF14dek	Keck/LRIS	56868.32	1
iPTF14deq	Keck/LRIS	56869.59	1
iPTF14det	Keck/LRIS	56837.54	1
iPTF14dfy	Keck/LRIS	56951.25	1
iPTF14efq	Keck/LRIS	56899.40	1
iPTF14eif	Keck/LRIS	56922.58	1
iPTF14eil	P200/DBSP	56898.28	1
iPTF14evw	P200/DBSP	56931.00	1
iPTF14fe	P200/DBSP	56689.50	1
iPTF14flu	Keck/LRIS	56980.24	1
iPTF14fuz	P200/DBSP	56931.00	3
iPTF14gao	Keck/DEIMOS	56924.54	3
iPTF14gaq	P200/DBSP	56931.00	1
iPTF14ghs	Keck/LRIS	56951.37	1
iPTF14gik	P200/DBSP	56961.39	1
iPTF14gjt	Keck/LRIS	56980.36	1
iPTF14gjv	FTS/FLOYDS	56942.52	3
iPTF14gqr	Keck/LRIS	56951.41	30
iPTF14grv	Keck/DEIMOS	57012.19	1
iPTF14gvb	Keck/LRIS	57008.31	1
iPTF14gyn	Keck/LRIS	56954.45	1
iPTF14gyn	Keck/LRIS	57008.29	1
iPTF14hac	Keck/LRIS	56980.35	1
iPTF14hls	NOT/ALFOSC	57064.12	31
iPTF14hqg	APO/DIS	56992.21	1
iPTF14hvw	Keck/LRIS	57008.64	1
iPTF14igl	P200/DBSP	56983.45	3
iPTF14igm	Keck/LRIS	57008.22	1
iPTF14ih	P200/DBSP	56680.30	1
iPTF14ikn	APO/DIS	56992.14	3
iPTF14jfc	Keck/LRIS	57008.24	3
iPTF14jfy	P200/DBSP	57013.00	1
iPTF14jgt	Lick/Kast	56987.54	10
iPTF14jku	NOT/ALFOSC	56959.15	1
iPTF14oe	Keck/DEIMOS	56717.00	1
iPTF14tb	Keck/LRIS	56776.29	1
iPTF14to	P200/DBSP	56751.00	1
iPTF14ur	Magellan/IMACS	56725.00	3
iPTF14us	Keck/LRIS	56805.31	1
iPTF14uw	P200/DBSP	56713.00	1
iPTF14va	Keck/DEIMOS	56717.00	3
iPTF14vh	P200/DBSP	56713.00	1
iPTF14vs	P200/DBSP	56713.00	1
iPTF14we	Keck/DEIMOS	56717.00	1
iPTF14x	P200/DBSP	56663.00	1
iPTF14ym	Keck/DEIMOS	56742.64	3
iPTF14yx	Magellan/IMACS	56725.00	1
iPTF15acp	NOT/ALFOSC	57124.07	3
iPTF15acr	P200/DBSP	57122.00	3
iPTF15adv	Keck/DEIMOS	57128.41	3
iPTF15afv	Keck/DEIMOS	57192.57	3
iPTF15afw	P200/DBSP	57122.25	3
iPTF15agj	Keck/DEIMOS	57128.54	1
iPTF15agp	Gemini-North/GMOS	57123.00	1
iPTF15agq	Keck/LRIS	57186.43	1
iPTF15ags	Keck/DEIMOS	57128.36	1
iPTF15aiw	Keck/LRIS	57134.46	3
iPTF15ak	Keck/LRIS	57044.26	1
iPTF15akq	Keck/LRIS	57158.55	19
iPTF15alq	P200/DBSP	57187.00	1
iPTF15asq	Keck/LRIS	57162.43	1
iPTF15axu	Keck/LRIS	57186.39	1
iPTF15axz	Keck/LRIS	57186.35	1
iPTF15aym	NOT/ALFOSC	57175.98	4
iPTF15ayo	P200/DBSP	57190.00	1
iPTF15ayt	Gemini-North/GMOS	57203.37	1
iPTF15ban	Gemini-North/GMOS	57233.26	1
iPTF15bcm	P200/DBSP	57187.00	1
iPTF15beu	Keck/LRIS	57186.57	1
iPTF15bky	NOT/ALFOSC	57196.03	4
iPTF15blp	P200/DBSP	57226.00	4
iPTF15btp	P200/DBSP	57226.00	1
iPTF15bxa	Keck/DEIMOS	57282.31	1
iPTF15bxb	Keck/DEIMOS	57282.33	1
iPTF15bxe	NOT/ALFOSC	57240.97	1
iPTF15bze	Keck/DEIMOS	57282.45	1
iPTF15cam	Keck/LRIS	57305.32	3
iPTF15cdy	Keck/DEIMOS	57333.34	1
iPTF15cfw	Keck/DEIMOS	57282.28	1
iPTF15cna	Keck/LRIS	57362.00	3
iPTF15cno	Keck/DEIMOS	57282.35	1
iPTF15cpq	Keck/DEIMOS	57282.48	3
iPTF15crj	FTN/FLOYDS	57288.26	1
iPTF15cyk	VLT/X-Shooter	57308.00	1
iPTF15cym	Keck/DEIMOS	57282.61	1
iPTF15cyq	Keck/DEIMOS	57282.57	1
iPTF15czf	Keck/DEIMOS	57333.49	1
iPTF15daw	Gemini-North/GMOS	57298.51	1
iPTF15dda	FTN/FLOYDS	57314.49	1
iPTF15dff	Keck/DEIMOS	57333.48	1
iPTF15dh	FTN/FLOYDS	57046.60	1
iPTF15dhx	Keck/DEIMOS	57333.25	3
iPTF15dio	Keck/LRIS	57308.64	1
iPTF15dip	Keck/LRIS	57308.63	1
iPTF15dix	Keck/DEIMOS	57333.34	1
iPTF15dkm	TNG/DOLORES	57324.00	1
iPTF15dld	Keck/DEIMOS	57333.32	1
iPTF15dlj	TNG/DOLORES	57324.00	1
iPTF15dlk	NTT/EFOSC2	57344.11	32
iPTF15dmk	Keck/DEIMOS	57333.38	1
iPTF15dof	P200/DBSP	57401.00	1
iPTF15dpa	Gemini-North/GMOS	57327.51	3
iPTF15dqb	Keck/DEIMOS	57333.56	3
iPTF15dqg	Keck/LRIS	57362.00	9
iPTF15dqi	Keck/DEIMOS	57333.35	1

Table 8
(Continued)

Object	Telescope/ Instrument	MJD (day)	Reference
iPTF15dsr	Keck/DEIMOS	57363.23	1
iPTF15dtg	Keck/LRIS	57362.00	6
iPTF15dtq	Keck/LRIS	57337.61	1
iPTF15dum	Gemini-North/GMOS	57339.44	1
iPTF15dvg	TNG/DOLORES	57368.92	3
iPTF15enr	Lijang/YFOSC	57298.70	33
iPTF15eoc	P200/DBSP	57363.00	3
iPTF15eon	Lick/Kast	57279.40	1
iPTF15eot	Keck/LRIS	57362.00	1
iPTF15eov	Keck/DEIMOS	57395.00	9
iPTF15epp	Keck/DEIMOS	57363.37	1
iPTF15eqc	Keck/DEIMOS	57363.65	1
iPTF15eqq	Keck/LRIS	57362.00	1
iPTF15eqr	Keck/LRIS	57362.00	4
iPTF15eqv	P200/DBSP	57363.00	3
iPTF15eqy	Keck/DEIMOS	57363.41	1
iPTF15erh	Keck/DEIMOS	57363.32	1
iPTF15esb	Keck/DEIMOS	57372.00	34
iPTF15eta	P200/DBSP	57367.00	1
iPTF15eta	P200/DBSP	57401.00	1
iPTF15ewh	Gemini-North/GMOS	57369.56	1
iPTF15ezl	Keck/LRIS	57399.61	1
iPTF15fdv	Gemini-North/GMOS	57385.27	1
iPTF15fhl	Gemini-North/GMOS	57385.59	3
iPTF15fkc	P60/SEDM	57400.00	1
iPTF15fkc	P200/DBSP	57401.00	1
iPTF15fmk	P60/SEDM	57402.00	1
iPTF15fmr	LDT/Deveny+LMI	57403.38	1
iPTF15fnk	P60/SEDM	57462.00	1
iPTF15gc	P200/DBSP	57066.00	1
iPTF15ii	P200/DBSP	57066.00	1
iPTF15il	Ekar/AFOSC	57052.99	35
iPTF15jg	P200/DBSP	57066.00	1
iPTF15km	Gemini-North/GMOS	57070.00	1
iPTF15n	Keck/LRIS	57104.32	3
iPTF15ul	Gemini-North/GMOS	57102.00	19
iPTF15vo	P200/DBSP	57108.00	1
iPTF16ahq	NOT/ALFOSC	57519.91	3
iPTF16alo	Keck/DEIMOS	57512.35	1
iPTF16alp	Keck/DEIMOS	57512.39	1
iPTF16ama	Keck/DEIMOS	57512.62	1
iPTF16aqo	FTN/FLOYDS	57568.36	1
iPTF16asu	Keck/LRIS	57549.00	9
iPTF16axb	P200/DBSP	57539.00	1
iPTF16bad	Keck/LRIS	57546.49	34
iPTF16baq	Keck/LRIS	57546.40	1
iPTF16bde	Keck/DEIMOS	57543.43	1
iPTF16bfy	P200/DBSP	57549.17	3
iPTF16bgg	P60/SEDM	57555.00	1
iPTF16bkn	P200/DBSP	57564.27	1
iPTF16bn	P200/DBSP	57447.00	1
iPTF16br	Keck/DEIMOS	57449.00	1
iPTF16bt	Keck/LRIS	57425.58	1
iPTF16bw	SOAR/Goodman	57427.13	36
iPTF16by	TNG/DOLORES	57430.02	1
iPTF16cft	P60/SEDM	57616.00	1
iPTF16coi	NOT/ALFOSC	57656.08	1
iPTF16drc	P60/SEDM	57606.00	1
iPTF16eh	P200/DBSP	57445.00	37
iPTF16emo	P60/SEDM	57602.00	1
iPTF16emv	P60/SEDM	57603.00	1
iPTF16eob	P60/SEDM	57628.00	1
iPTF16euq	P60/SEDM	57619.00	1
iPTF16exv	P60/SEDM	57612.87	38
iPTF16fak	P60/SEDM	57633.00	1
iPTF16fau	P200/DBSP	57626.00	1
iPTF16fb	P200/DBSP	57445.00	4
iPTF16fcg	P60/SEDM	57637.00	1
iPTF16fee	P200/DBSP	57626.00	1
iPTF16fip	P200/DBSP	57626.00	1
iPTF16fir	TNG/DOLORES	57899.17	1
iPTF16fiz	P60/SEDM	57627.00	1
iPTF16fji	P200/DBSP	57662.00	1
iPTF16flq	NOT/ALFOSC	57646.06	3
iPTF16foa	P60/SEDM	57633.00	1
iPTF16foo	P60/SEDM	57638.00	1
iPTF16fop	LDT/Deveny+LMI	57683.26	1
iPTF16ftb	P200/DBSP	57662.00	1
iPTF16gdv	Keck/LRIS	57661.28	1
iPTF16gdw	Keck/DEIMOS	57685.00	1
iPTF16geg	P200/DBSP	57662.00	1
iPTF16gkm	P60/SEDM	57710.00	1
iPTF16gop	P60/SEDM	57660.00	1
iPTF16gor	P60/SEDM	57670.00	1
iPTF16gox	P200/DBSP	57662.00	9
iPTF16goy	P200/DBSP	57662.00	1
iPTF16gqr	Keck/LRIS	57720.39	1
iPTF16grk	FTS/FLOYDS	57683.42	1
iPTF16gtl	P200/DBSP	57662.00	1
iPTF16gts	P200/DBSP	57667.00	1
iPTF16gwm	P200/DBSP	57687.00	1
iPTF16gyp	P60/SEDM	57680.00	1
iPTF16gzr	P60/SEDM	57698.00	1
iPTF16gzs	P60/SEDM	57683.00	1
iPTF16he	P200/DBSP	57445.00	3
iPTF16hfb	P60/SEDM	57698.00	1
iPTF16hgm	P60/SEDM	57683.00	1
iPTF16hgp	Keck/LRIS	57694.31	3
iPTF16hhj	P200/DBSP	57687.00	1
iPTF16hhz	P200/DBSP	57687.00	1
iPTF16hil	Keck/LRIS	57692.49	39
iPTF16hlu	Keck/LRIS	57694.53	1
iPTF16hrv	Ekar/AFOSC	57722.48	40
iPTF16hzg	FTN/FLOYDS	57709.30	1
iPTF16ied	P60/SEDM	57771.00	1
iPTF16ilg	P60/SEDM	57718.00	1
iPTF16ilj	NOT/ALFOSC	57720.97	9
iPTF16iyy	MDM/OSMOS	57761.26	41
iPTF16lb	P200/DBSP	57445.00	1
iPTF16pl	P200/DBSP	57522.00	1
iPTF16pq	SOAR/Goodman	57401.16	42
iPTF16qw	Keck/DEIMOS	57512.27	1
iPTF16rk	Keck/LRIS	57453.49	1
iPTF16tu	P200/DBSP	57535.00	1
iPTF16vz	NTT/EFOSC2	57432.36	43
iPTF16wf	Keck/DEIMOS	57512.35	1
iPTF17aal	P200/DBSP	57786.36	1
iPTF17aub	P60/SEDM	57800.00	1
iPTF17axg	P200/DBSP	57809.39	1
iPTF17bbq	P200/DBSP	57807.00	1

Table 8
(Continued)

Object	Telescope/ Instrument	MJD (day)	Reference
iPTF17bck	Keck/LRIS	57811.54	1
iPTF17beb	LT/SPRAT	57722.13	44
iPTF17bkj	Keck/LRIS	57811.42	1
iPTF17bsi	P200/DBSP	57828.49	1
iPTF17btx	P200/DBSP	57816.18	1
iPTF17bxk	P200/DBSP	57816.36	1
iPTF17cw	Keck/LRIS	57811.44	9
iPTF17jg	P200/DBSP	57807.00	1
iPTF17pq	P200/DBSP	57828.19	1
iPTF17vi	P200/DBSP	57828.43	1
iPTF17wj	P200/DBSP	57785.30	1
iPTF17xf	P200/DBSP	57785.35	1
iPTF17zg	LDT/Deveny+LMI	57828.23	1

Note. All spectra are publicly available on WISeREP (https://wiserep.weizmann.ac.il).

References. (1) This paper; (2) (Quimby et al. 2018); (3) C. Fremling et al. (2021, in preparation); (4) Nyholm et al. (2020); (5) Quimby et al. (2011); (6) Taddia et al. (2016); (7) Khazov et al. (2016); (8) Ofek et al. (2010); (9) Taddia et al. (2019); (10) Shivvers et al. (2019); (11) Corsi et al. (2011); (12) Ben-Ami et al. (2014); (13) Walker et al. (2014); (14) Ofek et al. (2013); (15) Gal-Yam et al. (2011); (16) Corsi et al. (2012); (17) Rubin et al. (2016); (18) Corsi et al. (2014); (19) Hosseinzadeh et al. (2017); (20) Pian et al. (2020); (21) Soumagnac et al. (2019); (22) Perley et al. (2016); (23) Fremling et al. (2016); (24) Vreeswijk et al. (2014); (25) Gorbikov et al. (2014); (26) Fremling et al. (2014); (27) Yaron et al. (2017); (28) Yan et al. (2015); (29) Nyholm et al. (2017); (30) De et al. (2018); (31) Arcavi et al. (2017); (32) Campbell et al. (2015); (33) Zhang & Wang (2015); (34) Yan et al. (2017); (35) Tomasella et al. (2015); (36) Pan (2016a); (37) Lunnan et al. (2018); (38) Blagorodnova (2016); (39) Irani et al. (2019); (40) Tomasella (2016); (41) Prieto & Simonian (2017); (42) Pan (2016b); (43) Terreran et al. (2016); (44) Copperwheat et al. (2017).

(This table is available in its entirety in machine-readable form.)

Appendix B
Host Photometry

Table 9 summarizes the photometry of all objects in our sample.

Table 9
Photometry of the PTF CCSN Host Galaxies

PTF	Telescope Survey	Filter	Brightness (mag)	Reference
09awk	GALEX	FUV	20.24 ± 0.26	1
09awk	GALEX	NUV	20.03 ± 0.10	1
09awk	SDSS	u'	19.2 ± 0.06	1
09awk	SDSS	g'	18.16 ± 0.05	1
09awk	SDSS	r'	17.8 ± 0.05	1
09awk	SDSS	i'	17.51 ± 0.05	1
09awk	SDSS	z'	17.43 ± 0.06	1
09awk	PS1	$g_{\rm PS1}$	18.15 ± 0.05	1
09awk	PS1	$r_{\rm PS1}$	17.86 ± 0.05	1
09awk	PS1	$i_{\rm PS1}$	17.52 ± 0.05	1
09awk	PS1	$z_{\rm PS1}$	17.48 ± 0.05	1
09awk	PS1	$y_{\rm PS1}$	17.41 ± 0.06	1
09awk	2MASS	J	17.09 ± 0.11	1
09awk	2MASS	H	17.21 ± 0.09	1
09awk	2MASS	K	17.48 ± 0.13	1
09axi	SDSS	u'	20.17 ± 0.14	1
09axi	SDSS	g'	18.77 ± 0.06	1
09axi	SDSS	r'	18.47 ± 0.06	1
09axi	SDSS	i'	18.21 ± 0.06	1
09axi	SDSS	z'	18.16 ± 0.11	1
09axi	PS1	$g_{\rm PS1}$	18.88 ± 0.07	1
09axi	PS1	$r_{\rm PS1}$	18.52 ± 0.07	1
09axi	PS1	$i_{\rm PS1}$	18.29 ± 0.06	1
09axi	PS1	$z_{\rm PS1}$	18.26 ± 0.10	1
09axi	PS1	$y_{\rm PS1}$	18.29 ± 0.20	1
09bcl	PS1	$g_{\rm PS1}$	16.01 ± 0.46	1
09bcl	PS1	$r_{\rm PS1}$	15.27 ± 0.41	1
09bcl	PS1	$i_{\rm PS1}$	14.83 ± 0.40	1
09bcl	PS1	$z_{\rm PS1}$	14.60 ± 0.23	1
09bcl	PS1	$y_{\rm PS1}$	14.36 ± 0.24	1
09bcl	2MASS	J	13.98 ± 0.07	1
09bcl	2MASS	H	13.81 ± 0.07	1
09bcl	2MASS	K	13.88 ± 0.11	1
09bcl	WISE	$W1$	14.5 ± 0.10	1
09bcl	WISE	$W2$	15.05 ± 0.10	1

Note. All magnitudes are reported in the AB system and not corrected for reddening.

References. (1) This paper.

(This table is available in its entirety in machine-readable form.)

Appendix C
Examples of Bad SED Fits

Figure 15 displays examples of SEDs of SN host galaxies with poor fit statistics.

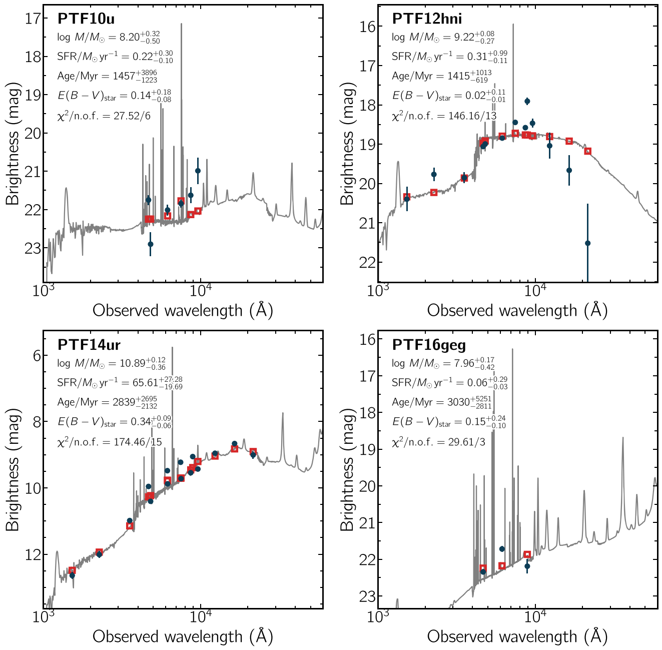

Figure 15. Examples of SEDs of SN host galaxies from 1000 to 60000 Å (similar to Figure 2) with poor fit statistics (χ^2/n. o. f. between 3 and 12). The fit quality is still high enough to extract reliable host properties. PTF10u and iPTF16geg exploded in very low-mass galaxies. The model-predicted and observed photometry deviate from each other. This is not unexpected given the plethora of emission lines of the best-fit model. The quality of the photometry at >7000 Å of the host of PTF12hni is not very good, driving the poor fit statistics. PTF14ur exploded in a galaxy with a large angular size. It is known that the PanSTARRS sky subtraction oversubtracts in areas with diffuse emission. This issue can lead to a deviation between SDSS and PanSTARRS images of up to several tenths of a magnitude.

Appendix D
Supernova Classifications

PTF09aux—Arcavi et al. (2010) classified the SN as a Type Ia/Ic SN. Owing to the ambiguity of the classification, we excluded this SN from our sample.

PTF09axc—Initially classified as an SN II (Arcavi et al. 2010), Arcavi et al. (2014) showed that this transient is in fact a TDE.

PTF09bcl—Arcavi et al. (2010) classified this transient as an SN II, but Nyholm et al. (2020) showed it to be an SN IIn.

PTF09bfz—Initially classified as an SN Ic-BL (Arcavi et al. 2010), Quimby et al. (2018) concluded that it is an SLSN using a new library of SN templates that were not available in 2010.

PTF09ct—Arcavi et al. (2010) classified this transient as an SN II. Spectra not available to them showed that it is in fact an SN IIn.

PTF09djl—Initially classified as an SN II (Arcavi et al. 2010), Arcavi et al. (2014) showed that this transient is actually a TDE.

PTF09ebq—Arcavi et al. (2010) initially classified the transient as an SN II in the center of its host galaxy. A reinspection of all data revealed variability about 1–2 months before the discovery of the transient. It is more likely an active galactic nucleus.

PTF09ejz—Arcavi et al. (2010) classified the SN as an SN Ia/Ic. Owing to the ambiguity of the classification, we excluded this SN from our sample.

PTF09ism—A reinspection of the spectra revealed He I λ 6678 in absorption, albeit weaker than what is deemed for a Type IIb SN. We changed its classification from Type II (Arcavi et al. 2010) to Type IIb.

PTF09q—Quimby et al. (2018) concluded that this object could be a H-poor SLSN instead of being an SN Ic (Arcavi et al. 2010). Quimby et al. (2018) noted that its massive host galaxy would be at odds with the known population of SLSN hosts, albeit a few SLSNe in massive hosts were reported in the literature (e.g., SN 2017egm; Nicholl et al. 2017; Bose et al. 2018). We follow Arcavi et al. (2010); De et al. (2018), and Fremling et al. (2018), classifying the object as an SN Ic.

PTF09tm—The Lick spectrum from 2009 July 25 shows narrow Balmer emission lines from Hα to Hγ, making it a Type IIn SN (Nyholm et al. 2020), instead of a Type II SN (Arcavi et al. 2010).

PTF10aaxi—Smith et al. (2012) classified PTF10aaxi as a Type II SN. HST images obtained after the transient faded show a resolved source with an absolute magnitude of −8 at the explosion site. With the currently available data, it remains ambiguous whether this object is connected with PTF10aaxi or is a companion star. Owing to this ambiguity, we removed PTF10aaxi from our final sample.

PTF10acbu—The spectrum of this stripped-envelope SN shows no helium in absorption. Therefore, we change the classification from Type Ib (Fremling et al. 2018) to Type Ic.

PTF10bip—We classify this object as an SN Ic, whereas it was listed as uncertain (SN Ic/SN Ic-BL) by Modjaz et al. (2020).

PTF10cwx—Initially classified as an SN II (Arcavi et al. 2010), a reassessment of the spectrum reveals narrow Balmer emission lines from Hα to Hγ, making it an SN IIn (Nyholm et al. 2020).

PTF10cxx—The spectrum shows narrow Balmer emission lines from Hα to Hδ, making this object an SN IIn, not an SN II (Arcavi et al. 2010).

PTF10gvb—De Cia et al. (2018) reported that spectra of this candidate SLSN (Quimby et al. 2018; Modjaz et al. 2020) lack the typical features of SLSNe and are better matched with templates of SNe Ic-BL. We follow this assessment and put PTF10gvb in the sample of SNe Ic-BL.

PTF10hgi—We followed Quimby et al. (2018) and Gal-Yam (2019), classifying this transient as an SLSN-IIb instead of an SLSN-I (Inserra et al. 2013).

PTF10izr—Fremling et al. (2018) classified this transient as an SN Ic. We removed it from our sample because of the poor data quality.

PTF10qwu—Perley et al. (2016) classified PTF10qwu as an SLSN-IIn. However, a detailed analysis by G. Leloudas et al. (2021, in preparation) raises concerns about this classification. We follow G. Leloudas et al. (2021, in preparation) and designate PTF10qwu an SN IIn.

PTF10svt—We classified this object as an SN Ic, whereas it was listed as uncertain (SN Ic/SN Ic-BL) by Modjaz et al. (2020).

PTF10tqv—This object was classified as an SN Ic-BL by Taddia et al. (2019) and Modjaz et al. (2020), and as an SN Ic by Fremling et al. (2018). Taddia et al. (2019) and Modjaz et al. (2020) showed that the spectra are better matched with SN Ic-

BL templates than templates of normal SNe Ic. We follow this analysis and classify it as an SN Ic-BL.

PTF10ts—The classification spectrum shows narrow Balmer emission lines from Hα to Hδ, making this object an SN IIn instead of an SN II (Arcavi et al. 2010).

PTF10u—The spectrum shows narrow Balmer emission lines from Hα to Hδ, making this object an SN IIn instead of an SN II (Arcavi et al. 2010).

PTF10wg—The classification of this transient is not free of ambiguity (Arcavi et al. 2010; Fremling et al. 2018); therefore, we exclude it.

PTF10ysd—Modjaz et al. (2020) concluded that the SN Ic templates provide a better match for this SN than SN Ic-BL templates (Taddia et al. 2019).

PTF10yyc—Perley et al. (2016) classified PTF10yyc as an SLSN-IIn. However, a detailed analysis by G. Leloudas et al. (2021, in preparation) raises concerns about this classification. We follow G. Leloudas et al. (2021, in preparation) and designate PTF10yyc an SN IIn.

PTF11gcj—Fremling et al. (2018) classified this transient as an SN Ic. Modjaz et al. (2020) used a newer SN template library and showed that SN Ic-BL templates match the spectra of PTF11gcj better.

PTF11mnb—Quimby et al. (2018) pointed out that the spectra are similar to those of the H-poor SLSN SN 1999as; however, it reached a peak luminosity of only $M_r \approx -18.9$ mag. We follow De Cia et al. (2018) and Taddia et al. (2019), classifying the transient as an SN Ic.

PTF11pnq—Spectra of this SN are better matched with SN Ib templates than with SN Ibc templates (Fremling et al. 2020).

PTF12epg—Perley et al. (2016) classified PTF12epg as an SLSN-IIn. However, a detailed analysis by G. Leloudas et al. (2021, in preparation) raises doubts about the nature of this transient. We follow G. Leloudas et al. (2021, in preparation) and designate PTF12epg as an SN IIn.

PTF12gty—Fremling et al. (2018) and Barbarino et al. (2020) classified this transient as an SN Ic. Quimby et al. (2018) used a larger template database and showed that this is a H-poor SLSN, the classification we adopt.

PTF12hni—Fremling et al. (2018) classified this transient as an SN Ic. Quimby et al. (2018) used a larger template database and showed that this is a H-poor SLSN, the designation we adopt.

iPTF13doq—Fremling et al. (2018) classified this transient as an SN Ic. We removed this object from our sample because of the low contrast between the SN and the host galaxy in the transient spectrum.

iPTF14jhf—Fremling et al. (2018) classified this transient as an SN Ic and Barbarino et al. (2020) as an SN Ibc. We removed this object from our sample owing to the poor data quality.

iPTF15eov—Taddia et al. (2019) classified iPTF15eov as an SN Ic-BL, but the authors also pointed out several peculiarities. The light curve is too broad, and the peak luminosity of $M_r = -21.8$ mag is 3.2 mag more luminous than the average SN Ic-BL in their sample and 1 mag more luminous than the second-most-luminous SN Ic-BL in their sample. They also concluded that the light curve could not be powered by the radioactive decay of nickel. The peak luminosity and the broad light curve are rather characteristic of an SLSN. Furthermore, Taddia et al. (2019) pointed out that the spectra of iPTF15eov are similar to those of the H-poor SLSN PTF11rks. We agree with this assessment and change the classification of iPTF15eov from SN Ic-BL to SLSN-I.

iPTF16flq—Fremling et al. (2020) and Barbarino et al. (2020) classified this object as an SN Ibc. We see no He in absorption in any of the spectra and hence classify it as an SN Ic.

ORCID iDs

Steve Schulze https://orcid.org/0000-0001-6797-1889
Jesper Sollerman https://orcid.org/0000-0003-1546-6615
Giorgos Leloudas https://orcid.org/0000-0002-8597-0756
Angus H. Wright https://orcid.org/0000-0001-7363-7932
Ragnhild Lunnan https://orcid.org/0000-0001-9454-4639
Avishay Gal-Yam https://orcid.org/0000-0002-3653-5598
Eran O. Ofek https://orcid.org/0000-0002-6786-8774
Daniel A. Perley https://orcid.org/0000-0001-8472-1996
Alexei V. Filippenko https://orcid.org/0000-0003-3460-0103
Mansi M. Kasliwal https://orcid.org/0000-0002-5619-4938
Shrinivas R. Kulkarni https://orcid.org/0000-0001-5390-8563
James D. Neill https://orcid.org/0000-0002-0466-1119
Peter E. Nugent https://orcid.org/0000-0002-3389-0586
Robert M. Quimby https://orcid.org/0000-0001-9171-5236
Mark Sullivan https://orcid.org/0000-0001-9053-4820
Nora Linn Strotjohann https://orcid.org/0000-0002-4667-6730
Iair Arcavi https://orcid.org/0000-0001-7090-4898
Sagi Ben-Ami https://orcid.org/0000-0001-6760-3074
Federica Bianco https://orcid.org/0000-0003-1953-8727
Joshua S. Bloom https://orcid.org/0000-0002-7777-216X
Morgan Fraser https://orcid.org/0000-0003-2191-1674
Christoffer U. Fremling https://orcid.org/0000-0002-4223-103X
Assaf Horesh https://orcid.org/0000-0002-5936-1156
Joel Johansson https://orcid.org/0000-0001-5975-290X
Patrick L. Kelly https://orcid.org/0000-0003-3142-997X
Sladjana Knežević https://orcid.org/0000-0003-1416-8069
Kate Maguire https://orcid.org/0000-0002-9770-3508
Seméli Papadogiannakis https://orcid.org/0000-0003-0783-3323
Tanja Petrushevska https://orcid.org/0000-0003-4743-1679
Adam Rubin https://orcid.org/0000-0003-4557-0632
Lin Yan https://orcid.org/0000-0003-1710-9339
Filomena Bufano https://orcid.org/0000-0002-3429-2481
Ryan J. Foley https://orcid.org/0000-0002-2445-5275
Yoav Green https://orcid.org/0000-0002-0809-6575
Jussi Harmanen https://orcid.org/0000-0001-8242-4090
Anna Y. Q. Ho https://orcid.org/0000-0002-9017-3567
Isobel M. Hook https://orcid.org/0000-0002-2960-978X
Griffin Hosseinzadeh https://orcid.org/0000-0002-0832-2974
D. Andrew Howell https://orcid.org/0000-0003-4253-656X
Albert K. H. Kong https://orcid.org/0000-0002-5105-344X
Rubina Kotak https://orcid.org/0000-0001-5455-3653
Thomas Matheson https://orcid.org/0000-0001-6685-0479
Curtis McCully https://orcid.org/0000-0001-5807-7893
Dan Milisavljevic https://orcid.org/0000-0002-0763-3885
Yen-Chen Pan https://orcid.org/0000-0001-8415-6720
Dovi Poznanski https://orcid.org/0000-0003-1470-7173
Sjoert van Velzen https://orcid.org/0000-0002-3859-8074

References

Ahn, C. P., Alexandroff, R., Allende Prieto, C., et al. 2012, ApJS, 203, 21

Anderson, J. P., Habergham, S. M., James, P. A., & Hamuy, M. 2012, MNRAS, 424, 1372

Andrews, B. H., & Martini, P. 2013, ApJ, 765, 140

Angus, C. R., Levan, A. J., Perley, D. A., et al. 2016, MNRAS, 458, 84

Angus, C. R., Smith, M., Sullivan, M., et al. 2019, MNRAS, 487, 2215

Arcavi, I., Gal-Yam, A., Kasliwal, M. M., et al. 2010, ApJ, 721, 777

Arcavi, I., Gal-Yam, A., Sullivan, M., et al. 2014, ApJ, 793, 38

Arcavi, I., Howell, D. A., Kasen, D., et al. 2017, Natur, 551, 210

Asplund, M., Grevesse, N., Sauval, A. J., & Scott, P. 2009, ARA&A, 47, 481

Astropy Collaboration, Price-Whelan, A. M., Sipőcz, B. M., et al. 2018, AJ, 156, 123

Astropy Collaboration, Robitaille, T. P., Tollerud, E. J., et al. 2013, A&A, 558, A33

Baldry, I. K., Driver, S. P., Loveday, J., et al. 2012, MNRAS, 421, 621

Barbarino, C., Sollerman, J., Taddia, F., et al. 2020, arXiv:2010.08392

Becker, A. 2015, HOTPANTS: High Order Transform of PSF ANd Template Subtraction, Astrophysics Source Code Library, ascl:1504.004

Bellm, E. C., Kulkarni, S. R., Barlow, T., et al. 2019, PASP, 131, 068003

Ben-Ami, S., Gal-Yam, A., Mazzali, P. A., et al. 2014, ApJ, 785, 37

Benn, C., Dee, K., & Agócs, T. 2008, Proc. SPIE, 7014, 70146X

Bertin, E. 2006, in ASP Conf. Ser., 351, Astronomical Data Analysis Software and Systems XV, ed. C. Gabriel et al. (San Francisco, CA: ASP), 112

Bertin, E., & Arnouts, S. 1996, A&AS, 117, 393

Bianchi, L., Conti, A., & Shiao, B. 2014, AdSpR, 53, 900

Bianchi, L., Shiao, B., & Thilker, D. 2017, ApJS, 230, 24

Bigelow, B. C., & Dressler, A. M. 2003, Proc. SPIE, 4841, 1727

Blagorodnova, N. 2016, TNSCR, 2016-557, 1

Blagorodnova, N., Neill, J. D., Walters, R., et al. 2018, PASP, 130, 035003

Blanton, M. R., & Roweis, S. 2007, AJ, 133, 734

Blondin, S., & Tonry, J. L. 2007, ApJ, 666, 1024

Boissier, S., & Prantzos, N. 2009, A&A, 503, 137

Bose, S., Dong, S., Pastorello, A., et al. 2018, ApJ, 853, 57

Brown, T. M., Baliber, N., Bianco, F. B., et al. 2013, PASP, 125, 1031

Byler, N., Dalcanton, J. J., Conroy, C., & Johnson, B. D. 2017, ApJ, 840, 44

Calzetti, D., Armus, L., Bohlin, R. C., et al. 2000, ApJ, 533, 682

Campbell, H., Lyman, J., Fraser, M., et al. 2015, ATel, 8139, 1

Cano, Z., de Ugarte Postigo, A., Perley, D., et al. 2015, MNRAS, 452, 1535

Cano, Z., Wang, S.-Q., Dai, Z.-G., & Wu, X.-F. 2017, AdAst, 2017, 8929054

Chabrier, G. 2003, PASP, 115, 763

Chambers, K. C., Magnier, E. A., Metcalfe, N., et al. 2016, arXiv:1612.05560

Chen, H.-L., Woods, T. E., Yungelson, L. R., Gilfanov, M., & Han, Z. 2015, MNRAS, 453, 3024

Chen, T.-W., Schady, P., Xiao, L., et al. 2017b, ApJL, 849, L4

Chen, T.-W., Smartt, S. J., Yates, R. M., et al. 2017a, MNRAS, 470, 3566

Conroy, C. 2013, ARA&A, 51, 393

Conroy, C., Gunn, J. E., & White, M. 2009, ApJ, 699, 486

Copperwheat, C. M., Piascik, A. S., & Steele, I. A. 2017, GCN, 20734, 1

Corsi, A., Ofek, E. O., Frail, D. A., et al. 2011, ApJ, 741, 76

Corsi, A., Ofek, E. O., Gal-Yam, A., et al. 2012, ApJL, 747, L5

Corsi, A., Ofek, E. O., Gal-Yam, A., et al. 2014, ApJ, 782, 42

Curtin, C., Cooke, J., Moriya, T. J., et al. 2019, ApJS, 241, 17

Cutri, R. M., Wright, E. L., Conrow, T., et al. 2013, Explanatory Supplement to the AllWISE Data Release Products

Daddi, E., Dickinson, M., Morrison, G., et al. 2007, ApJ, 670, 156

Davis, T. M., Hui, L., Frieman, J. A., et al. 2011, ApJ, 741, 67

De, K., Kasliwal, M. M., Ofek, E. O., et al. 2018, Sci, 362, 201

De Cia, A., Gal-Yam, A., Rubin, A., et al. 2018, ApJ, 860, 100

de Vaucouleurs, G. 1960, ApJ, 131, 574

Dey, A., Schlegel, D. J., Lang, D., et al. 2019, AJ, 157, 168

Elbaz, D., Daddi, E., Le Borgne, D., et al. 2007, A&A, 468, 33

Eldridge, J. J., Stanway, E. R., Xiao, L., et al. 2017, PASA, 34, e058

Faber, S. M., Phillips, A. C., Kibrick, R. I., et al. 2003, Proc. SPIE, 4841, 1657

Faber, S. M., Willmer, C. N. A., Wolf, C., et al. 2007, ApJ, 665, 265

Feindt, U., Nordin, J., Rigault, M., et al. 2019, JCAP, 2019, 005

Filippenko, A. V. 1997, ARA&A, 35, 309

Foreman-Mackey, D., Sick, J., & Johnson, B. 2014, Python-Fsps: Python Bindings To Fsps, v0.1.1, Zenodo, doi:10.5281/zenodo.12157

Freedman, W. L., & Madore, B. F. 2010, ARA&A, 48, 673

Fremling, C., Sollerman, J., Kasliwal, M. M., et al. 2018, A&A, 618, A37

Fremling, C., Sollerman, J., Taddia, F., et al. 2014, A&A, 565, A114

Fremling, C., Sollerman, J., Taddia, F., et al. 2016, A&A, 593, A68

Fremling, U. C., Miller, A. A., Sharma, Y., et al. 2020, ApJ, 895, 32

Frohmaier, C., Sullivan, M., Nugent, P. E., Goldstein, D. A., & DeRose, J. 2017, ApJS, 230, 4

Fruchter, A. S., Levan, A. J., Strolger, L., et al. 2006, Natur, 441, 463

Fynbo, J. P. U., Watson, D., Thöne, C. C., et al. 2006, Natur, 444, 1047

Gal-Yam, A. 2012, Sci, 337, 927

Gal-Yam, A. 2017, in Observational and Physical Classification of Supernovae, ed. A. W. Alsabti & P. Murdin (Cham: Springer), 195

Gal-Yam, A. 2019, ARA&A, 57, 305

Gal-Yam, A., Kasliwal, M. M., Arcavi, I., et al. 2011, ApJ, 736, 159

Galbany, L., Anderson, J. P., Sánchez, S. F., et al. 2018, ApJ, 855, 107

Galbany, L., Stanishev, V., Mourão, A. M., et al. 2016, A&A, 591, A48

Gorbikov, E., Gal-Yam, A., Ofek, E. O., et al. 2014, MNRAS, 443, 671

Graham, M. J., Kulkarni, S. R., Bellm, E. C., et al. 2019, PASP, 131, 078001

Graur, O., Bianco, F. B., Huang, S., et al. 2017a, ApJ, 837, 120

Graur, O., Bianco, F. B., Modjaz, M., et al. 2017b, ApJ, 837, 121

Greiner, J., Mazzali, P. A., Kann, D. A., et al. 2015, Natur, 523, 189

Grogin, N. A., Kocevski, D. D., Faber, S. M., et al. 2011, ApJS, 197, 35

Habergham, S. M., Anderson, J. P., & James, P. A. 2010, ApJ, 717, 342

Habergham, S. M., James, P. A., & Anderson, J. P. 2012, MNRAS, 424, 2841

Hakobyan, A. A., Karapetyan, A. G., Barkhudaryan, L. V., et al. 2016, MNRAS, 456, 2848

Hakobyan, A. A., Nazaryan, T. A., Adibekyan, V. Z., et al. 2014, MNRAS, 444, 2428

Hakobyan, A. A., Petrosian, A. R., McLean, B., et al. 2008, A&A, 488, 523

Helou, G., Madore, B. F., Schmitz, M., et al. 1991, in Databases and On-line Data in Astronomy, ed. M. A. Albrecht & D. Egret (Dordrecht: Springer), 89

Hill, G. J., Nicklas, H. E., MacQueen, P. J., et al. 1998, Proc. SPIE, 3355, 375

Hook, I. M., Jørgensen, I., Allington-Smith, J. R., et al. 2004, PASP, 116, 425

Horne, K. 1986, PASP, 98, 609

Hosseinzadeh, G., Arcavi, I., Valenti, S., et al. 2017, ApJ, 836, 158

Hosseinzadeh, G., McCully, C., Zabludoff, A. I., et al. 2019, ApJL, 871, L9

Howell, D. A., Kasen, D., Lidman, C., et al. 2013, ApJ, 779, 98

Howell, D. A., Sullivan, M., Perrett, K., et al. 2005, ApJ, 634, 1190

Ilbert, O., Tresse, L., Zucca, E., et al. 2005, A&A, 439, 863

Inserra, C., Smartt, S. J., Jerkstrand, A., et al. 2013, ApJ, 770, 128

Irani, I., Schulze, S., Gal-Yam, A., et al. 2019, ApJ, 887, 127

Izzo, L., Thöne, C. C., García-Benito, R., et al. 2018, A&A, 610, A11

Jerkstrand, A., Maeda, K., & Kawabata, K. S. 2020, Sci, 367, 415

Johnson, B. D., Leja, J. L., Conroy, C., & Speagle, J. S. 2019, Prospector: Stellar population inference from spectra and SEDs, Astrophysics Source Code Library, ascl:1905.025

Kangas, T., Portinari, L., Mattila, S., et al. 2017, A&A, 597, A92

Kann, D. A., Schady, P., Olivares, E. F., et al. 2019, A&A, 624, A143

Kelly, P. L., Filippenko, A. V., Modjaz, M., & Kocevski, D. 2014, ApJ, 789, 23

Kelly, P. L., & Kirshner, R. P. 2012, ApJ, 759, 107

Kelly, P. L., Kirshner, R. P., & Pahre, M. 2008, ApJ, 687, 1201

Khazov, D., Yaron, O., Gal-Yam, A., et al. 2016, ApJ, 818, 3

Koekemoer, A. M., Faber, S. M., Ferguson, H. C., et al. 2011, ApJS, 197, 36

Krühler, T., Malesani, D., Fynbo, J. P. U., et al. 2015, A&A, 581, A125

Kudritzki, R.-P., & Puls, J. 2000, ARA&A, 38, 613

Kulkarni, S. R. 2013, ATel, 4807, 1

Kuncarayakti, H., Doi, M., Aldering, G., et al. 2013a, AJ, 146, 30

Kuncarayakti, H., Doi, M., Aldering, G., et al. 2013b, AJ, 146, 31

Kuncarayakti, H., Maeda, K., Ashall, C. J., et al. 2018, ApJL, 854, L14

Laher, R. R., Surace, J., Grillmair, C. J., et al. 2014, PASP, 126, 674

Lang, D. 2014, AJ, 147, 108

Lantz, B., Aldering, G., Antilogus, P., et al. 2004, Proc. SPIE, 5249, 146

Law, N. M., Kulkarni, S. R., Dekany, R. G., et al. 2009, PASP, 121, 1395

Lee, N., Sanders, D. B., Casey, C. M., et al. 2015, ApJ, 801, 80

Leja, J., Johnson, B. D., Conroy, C., van Dokkum, P. G., & Byler, N. 2017, ApJ, 837, 170

Leloudas, G., Gallazzi, A., Sollerman, J., et al. 2011, A&A, 530, A95

Leloudas, G., Schulze, S., Krühler, T., et al. 2015, MNRAS, 449, 917

Leloudas, G., Sollerman, J., Levan, A. J., et al. 2010, A&A, 518, A29

Li, W., Chornock, R., Leaman, J., et al. 2011, MNRAS, 412, 1473

Liu, Y.-Q., Modjaz, M., Bianco, F. B., & Graur, O. 2016, ApJ, 827, 90

Lunnan, R., Chornock, R., Berger, E., et al. 2014, ApJ, 787, 138

Lunnan, R., Chornock, R., Berger, E., et al. 2015, ApJ, 804, 90

Lunnan, R., Fransson, C., Vreeswijk, P. M., et al. 2018, NatAs, 2, 887

Mainzer, A., Bauer, J., Cutri, R. M., et al. 2014, ApJ, 792, 30

Mannucci, F., Cresci, G., Maiolino, R., Marconi, A., & Gnerucci, A. 2010, MNRAS, 408, 2115

Martin, D. C., Fanson, J., Schiminovich, D., et al. 2005, ApJL, 619, L1

Mateo, M. L. 1998, ARA&A, 36, 435

McConnachie, A. W. 2012, AJ, 144, 4
McConnachie, A. W., Patton, D. R., Ellison, S. L., & Simard, L. 2009, MNRAS, 395, 255
Meisner, A. M., Lang, D., & Schlegel, D. J. 2017, AJ, 153, 38
Michałowski, M. J., Xu, D., Stevens, J., et al. 2018, A&A, 616, A169
Miller, T. B., van Dokkum, P., Mowla, L., & van der Wel, A. 2019, ApJL, 872, L14
Modjaz, M., Blondin, S., Kirshner, R. P., et al. 2014, AJ, 147, 99
Modjaz, M., Bianco, F. B., Siwek, M., et al. 2020, ApJ, 892, 153
Modjaz, M., Kewley, L., Kirshner, R. P., et al. 2008, AJ, 135, 1136
Modjaz, M., Liu, Y. Q., Bianco, F. B., & Graur, O. 2016, ApJ, 832, 108
Moriya, T. J., Tanaka, M., Yasuda, N., et al. 2019, ApJS, 241, 16
Morrissey, P., Conrow, T., Barlow, T. A., et al. 2007, ApJS, 173, 682
Mowla, L., van der Wel, A., van Dokkum, P., & Miller, T. B. 2019, ApJL, 872, L13
Muzzin, A., Marchesini, D., Stefanon, M., et al. 2013, ApJ, 777, 18
Neill, J. D., Sullivan, M., Gal-Yam, A., et al. 2011, ApJ, 727, 15
Nicholl, M., Berger, E., Margutti, R., et al. 2017, ApJL, 845, L8
Nicholl, M., Blanchard, P. K., Berger, E., et al. 2020, NatAs, 4, 893
Noeske, K. G., Weiner, B. J., Faber, S. M., et al. 2007, ApJL, 660, L43
Nyholm, A., Sollerman, J., Taddia, F., et al. 2017, A&A, 605, A6
Nyholm, A., Sollerman, J., Tartaglia, L., et al. 2020, A&A, 637, A73
Ofek, E. O., Laher, R., Surace, J., et al. 2012, PASP, 124, 854
Ofek, E. O., Rabinak, I., Neill, J. D., et al. 2010, ApJ, 724, 1396
Ofek, E. O., Sullivan, M., Cenko, S. B., et al. 2013, Natur, 494, 65
Oke, J. B., Cohen, J. G., Carr, M., et al. 1995, PASP, 107, 375
Oke, J. B., & Gunn, J. E. 1982, PASP, 94, 586
Oke, J. B., & Gunn, J. E. 1983, ApJ, 266, 713
Pan, Y. 2016a, TNSCR, 2016-132, 1
Pan, Y. 2016b, TNSCR, 2016-41, 1
Pan, Y. C., Foley, R. J., Smith, M., et al. 2017, MNRAS, 470, 4241
Patterson, M. T., Bellm, E. C., Rusholme, B., et al. 2019, PASP, 131, 018001
Pedregosa, F., Varoquaux, G., Gramfort, A., et al. 2011, J. Mach. Learn. Res., 12, 2825
Perley, D. A. 2019, PASP, 131, 084503
Perley, D. A., Fremling, C., Sollerman, J., et al. 2020, ApJ, 904, 35
Perley, D. A., Quimby, R. M., Yan, L., et al. 2016, ApJ, 830, 13
Pian, E., Mazzali, P. A., Moriya, T. J., et al. 2020, MNRAS, 497, 3542
Planck Collaboration, Ade, P. A. R., Aghanim, N., et al. 2016, A&A, 594, A13
Prantzos, N., & Boissier, S. 2003, A&A, 406, 259
Prieto, J., & Simonian, G. 2017, TNSCR, 2017-42, 1
Prieto, J. L., Stanek, K. Z., & Beacom, J. F. 2008, ApJ, 673, 999
Quimby, R. M., De Cia, A., Gal-Yam, A., et al. 2018, ApJ, 855, 2
Quimby, R. M., Kulkarni, S. R., Kasliwal, M. M., et al. 2011, Natur, 474, 487
Rau, A., Kulkarni, S. R., Law, N. M., et al. 2009, PASP, 121, 1334
Rice, S. O. 1945, BSTJ, 24, 46
Rubin, A., Gal-Yam, A., De Cia, A., et al. 2016, ApJ, 820, 33
Sana, H., de Mink, S. E., de Koter, A., et al. 2012, Sci, 337, 444
Sanders, N. E., Soderberg, A. M., Levesque, E. M., et al. 2012, ApJ, 758, 132
Sargent, M. T., Béthermin, M., Daddi, E., & Elbaz, D. 2012, ApJL, 747, L31
Schlafly, E. F., & Finkbeiner, D. P. 2011, ApJ, 737, 103
Schulze, S., Chapman, R., Hjorth, J., et al. 2015, ApJ, 808, 73
Schulze, S., Krühler, T., Leloudas, G., et al. 2018, MNRAS, 473, 1258
Scoville, N., Aussel, H., Brusa, M., et al. 2007, ApJS, 172, 1
Shivvers, I., Filippenko, A. V., Silverman, J. M., et al. 2019, MNRAS, 482, 1545
Silverman, J. M., Foley, R. J., Filippenko, A. V., et al. 2012, MNRAS, 425, 1789
Simcoe, R. A., Burgasser, A. J., Schechter, P. L., et al. 2013, PASP, 125, 270
Skrutskie, M. F., Cutri, R. M., Stiening, R., et al. 2006, AJ, 131, 1163
Smartt, S. J. 2009, ARA&A, 47, 63
Smith, M., Sullivan, M., Nichol, R. C., et al. 2018, ApJ, 854, 37
Smith, N., Cenko, S. B., Butler, N., et al. 2012, MNRAS, 420, 1135
Soumagnac, M. T., Ofek, E. O., Gal-yam, A., et al. 2019, ApJ, 872, 141
Speagle, J. S. 2020, MNRAS, 493, 3132
Stoll, R., Prieto, J. L., Stanek, K. Z., & Pogge, R. W. 2013, ApJ, 773, 12
Svensson, K. M., Levan, A. J., Tanvir, N. R., Fruchter, A. S., & Strolger, L. G. 2010, MNRAS, 405, 57
Taddia, F., Fremling, C., Sollerman, J., et al. 2016, A&A, 592, A89
Taddia, F., Sollerman, J., Fremling, C., et al. 2015, A&A, 580, A131
Taddia, F., Sollerman, J., Fremling, C., et al. 2019, A&A, 621, A71
Taddia, F., Sollerman, J., Razza, A., et al. 2013, A&A, 558, A143
Taggart, K., & Perley, D. 2021, MNRAS, 503, 3931
Tanga, M., Krühler, T., Schady, P., et al. 2018, A&A, 615, A136
Terreran, G., Faran, T., Kromer, M., Taubenberger, S., & Yaron, O. 2016, TNSCR, 2016-114, 1
Thöne, C. C., de Ugarte Postigo, A., Garcia-Benito, R., et al. 2015, MNRAS, 451, L65
Thöne, C. C., de Ugarte Postigo, A., Leloudas, G., et al. 2017, A&A, 599, A129
Tody, D. 1986, Proc. SPIE, 627, 733
Tomasella, L. 2016, TNSCR, 2016-977, 1
Tomasella, L., Benetti, S., Cappellaro, E., et al. 2015, ATel, 7012, 1
Tomczak, A. R., Quadri, R. F., Tran, K.-V. H., et al. 2014, ApJ, 783, 85
Toy, V. L., Cenko, S. B., Silverman, J. M., et al. 2016, ApJ, 818, 79
Tremonti, C. A., Heckman, T. M., Kauffmann, G., et al. 2004, ApJ, 613, 898
Tsvetkov, D. Y., Pavlyuk, N. N., & Bartunov, O. S. 2004, AstL, 30, 729
van den Bergh, S. 1997, AJ, 113, 197
Van Dyk, S. D. 2017, Handbook of Supernovae (Cham: Springer), 693
Vergani, S. D., Salvaterra, R., Japelj, J., et al. 2015, A&A, 581, A102
Vergani, S. D., Palmerio, J., Salvaterra, R., et al. 2017, A&A, 599, A120
Vernet, J., Dekker, H., D'Odorico, S., et al. 2011, A&A, 536, A105
Vreeswijk, P. M., Savaglio, S., Gal-Yam, A., et al. 2014, ApJ, 797, 24
Walker, E. S., Mazzali, P. A., Pian, E., et al. 2014, MNRAS, 442, 2768
Wright, A. H., Robotham, A. S. G., Bourne, N., et al. 2016, MNRAS, 460, 765
Wright, E. L., Eisenhardt, P. R. M., Mainzer, A. K., et al. 2010, AJ, 140, 1868
Yan, L., Lunnan, R., Perley, D. A., et al. 2017, ApJ, 848, 6
Yan, L., Quimby, R., Ofek, E., et al. 2015, ApJ, 814, 108
Yaron, O., & Gal-Yam, A. 2012, PASP, 124, 668
Yaron, O., Perley, D. A., Gal-Yam, A., et al. 2017, NatPh, 13, 510
Zapartas, E., de Mink, S. E., Izzard, R. G., et al. 2017, A&A, 601, A29
Zhang, J., & Wang, X. 2015, ATel, 8120, 1